Thermal conduction in amorphous materials and the role of collective excitations

Thesis by
Jaeyun Moon

In Partial Fulfillment of the Requirements for the
Degree of
Doctor of Philosophy

CALIFORNIA INSTITUTE OF TECHNOLOGY
Pasadena, California

2020
Defended December 11, 2019

Jaeyun Moon
ORCID: 0000-0001-8199-5588

ACKNOWLEDGEMENTS

Looking back through a little over 5 years of my Ph. D. journey, it is crystal clear that I couldn't have finished this thesis without the support I have received during this time.

I would like to first thank my advisor and mentor, Prof. Austin J. Minnich for his guidance and endless support. I am grateful for the countless discussions we have had for the last 5 years. I learned a lot about how to do research and how to ask good questions from working with him. I am extremely fortunate that he had given me a lot of scientific freedom and independence and that he allowed me to pursue projects that excite me. Because I am very interested in X-ray sciences and ultrafast phenomena, he allowed me to be away for a year at SLAC National Accelerator Laboratory and Stanford University to learn about these topics. For that, I owe a debt of gratitude to my advisor. I am also very fortunate that I was able to tackle scientific questions from several angles from calculations to experiments under his guidance.

I have had many enriching experiences at SLAC and Stanford. Due to close interactions between SLAC and Stanford researchers, there are many specialized courses regarding X-ray sciences, and I was fortunate to take some of these courses that are directly related to my current Ph. D. research and my future work as a post-doc at Oak Ridge National Laboratory. I would like to thank Profs. David Reis and Evan Reed for hosting me and for allowing me to pursue my scientific interests. I am also grateful that I was able to participate and do research projects there that were outside of my research area. I would also like to express my gratitudes to my lab members and friends at SLAC and Stanford: Dr. Peter Schindler, Dr. Rodrigo Freitas, Kenji Oyama, Dr. Austin Sendek, Evan Antoniuk, Gowoon Cheon, Vincent Dufour-Decieux, Aditi Krishnapriyan, Brandi Ransom, Yanbing Zhu, Jaclyn Schillinger, Viktor Krapivin, Dr. Mariano Trigo, Dr. Samuel Teitelbaum, Yijing Huang, Dr. Gilberto Antonio de la Pena Munoz, and Prof. Jerry Hastings. I am profoundly thankful for all the enriching and fun experiences with these wonderful people.

The help I have received from my collaborators has also been monumental in my thesis. I would like to express my gratitude to Drs. Raphäel P Hermann and Michael E. Manley from Oak Ridge National Laboratory and Ahmet Alatas and Ayman H.

Said from Argonne National Laboratory for their help in scattering measurements and for their fruitful scientific discussions.

I would like to thank my current and former lab members at Caltech: Dr. Benoit Latour, Taeyong Kim, Dr. Lina Yang, Dr. Ruiqiang Guo, Dr. Bo Sun, Dr. Nina Shulumba, Prof. Ole Martin Løvvik, Dr. Andrew Robbins, Dr. Nick Dou, Dr. Nathan Thomas, Peishi Cheng, Alex Choi, Adrian Tan, Erika Ye, Yang Gao, Zoila Jurado, Dr. Chengyun Hua, Dr. Navaneetha Ravichandran, Dr. Ding Ding, Dr. Hang Zhang, Dr. Xiangwen Chen, Dr. Junlong Kou, and Nachiket Naik. Being a member of our group has been a great learning experience. We had a lot of constructive discussions in the group meetings and in our offices in Gates Thomas Laboratory. Outside of the lab settings, we also had many memorable times in group socials. I would like to especially extend my gratitude to Andrew and Benoit who helped me get started with my research at the beginning of my Ph. D.

I am also grateful for the opportunities to have been the co-mentor to three undergraduate students in their summer projects as SURF students from IIT, Gandhinagar: Akash Pallath, Sowill Dave, and Ayushman Tripathi who have now gone to a graduate school to pursue a Ph. D. and to space agencies. It was a unique experience to teach and advise students on their projects.

Last but not least, the support from my close friends and family has been the linchpin of my Ph. D. I would like to thank my friends Andre da Silva, Peter Schindler, Gowoon Cheon, Evan Antoniuk, Vincent Dufour-Decieux, Joe Ahn, Connor McMahan, Camille Bernal, Abhishek Kwatra, Kien Nguyen, Sungwon Ahn, Louisa Avellar, Taeyong Kim, Takafumi Oyake, Vidyasagar, Radhika Kashyap, and William Rapin. I am profoundly grateful to my parents and my brother for their lifelong support and for teaching me to pursue excellence.

I would like to thank the Samsung Scholarship, Acosta Fellowship, and Resnick Sustainability Institute at Caltech for their graduate fellowships and I would like to thank the Kavli Nanoscience Institute at Caltech and its staff members for their support in my projects.

ABSTRACT

The atomic vibrations and thermal properties of amorphous dielectric solids are of fundamental and practical interest. For applications, amorphous solids are widely used as thermal insulators in thermopile and other detectors where low thermal conductivity directly sets the sensitivity of the detector. Amorphous solids are of fundamental interest themselves because the lack of atomic periodicity complicates theoretical development. As a result, the lower limits of thermal conductivity in solids as well as the nature of the vibrational excitations that carry heat remain active topics of research.

In this thesis, we use numerical and experimental methods to investigate the thermal conduction in amorphous dielectrics. We begin by using molecular dynamics to investigate the thermal conductivity of amorphous nanocomposites. We find that mismatching the vibrational density of states of constituent materials in the composite is an effective route to achieve exceptionally low thermal conductivity in fully dense solids.

We then transition to examining the properties of the atomic vibrations transporting heat in amorphous solids. For decades, normal mode methods have been used extensively to study thermal transport in amorphous solids. These methods naturally assume that normal modes are the fundamental vibrational excitations transporting heat. We examine the predictions from normal mode analysis that are now able to be tested against experiments, and we find that the predictions from these methods do not agree with experimental observations. For instance, normal mode methods predict that the low frequency normal modes are scattered by anharmonic interactions as in single crystalline solids. However, temperature dependent thermal conductivity measurements demonstrate a typical glassy temperature dependence inconsistent with normal modes scattering through anharmonic interactions. These discrepancies suggest that normal modes are not the fundamental heat carriers in amorphous dielectrics.

To identify the actual heat carriers, we draw on fundamental concepts from many-body physics and inelastic scattering theory that dictate that the excitation energies of a many-body interacting system are given by the poles of the single-particle Green's function. The imaginary part of this function is proportional to the dynamic structure factor that is directly measured in inelastic scattering experiments. Collective

excitations of a given energy and wavevector can thus be identified from peaks in the dynamic structure factor; their damping is given by the broadening of the peak. Using these concepts from many-body physics, the physical picture that emerges is that heat is carried in large part by a gas of weakly interacting collective excitations with a cutoff frequency that depends on the atomic structure and composition of the glass.

We test this picture using numerical and experimental inelastic scattering measurements on amorphous silicon, a commonly studied amorphous solid. We observe collective excitations up to 10 THz, well into the thermal spectrum, and far higher than previous inelastic scattering measurements on other glasses. Our numerical and experimental evidence also confirms that the collective excitations are damped by structural disorder rather than anharmonic interactions and that they dominate the thermal conduction in amorphous silicon. Subsequent analysis shows that these high frequency acoustic excitations are supported in amorphous silicon due to a large sound velocity and monatomic composition, suggesting that other monatomic amorphous solids with large sound velocities may also support these thermal excitations.

Overall, our results provide strong evidence that the heat carriers in amorphous dielectrics are collective excitations rather than normal modes. This change in physical picture advances our understanding of atomic dynamics in glasses and also provides a foundation for realizing dielectric solids with ultralow thermal conductivity.

PUBLISHED CONTENT AND CONTRIBUTIONS

1. Kim, T. *., Moon, J. *. & Minnich, A. J. Role of acoustic excitations in amorphous silicon characterizaed by ultrafast transient grating spectroscopy and picosecond acoustics. *In preparation.*
   J. M. synthesized samples, analyzed measurements, and co-wrote the manuscript along with other authors. This article was discussed in Chapter 3 of this thesis.

2. Moon, J. & Minnich, A. J. Examining the validity of normal modes as fundamental heat carriers in amorphous materials. *In preparation.*
   J. M. analyzed existing data in literature. J. M. performed classical molecular dynamics and ab-initio molecular dynamics simulations and analyzed data. J. M. wrote the manuscript. This article was discussed in Chapters 1, 2, and 3 of this thesis.

3. Sun, B. *et al.* High-frequency atomic tunneling yields ultralow and glass-like thermal conductivity in chalcogenide single crystals. *Under review.*
   J. M. performed inelastic scattering experiments.

4. Moon, J. *et al.* Thermal acoustic excitations with atomic-scale wavelengths in amorphous silicon. *Physical Review Materials* **3,** 065601 (2019).
   https://doi.org/10.1103/PhysRevMaterials.3.065601
   J. M. and A. J. M. conceived the idea. J. M. fabricated samples and performed experiments and analyzed data. J. M. wrote the manuscript.

5. DeAngelis, F. *et al.* Thermal Transport in Disordered Materials. en. *Nanoscale and Microscale Thermophysical Engineering* (2018).
   https://doi.org/10.1080/15567265.2018.1519004
   J. M. contributed to the manuscript.

6. Moon, J., Latour, B. & Minnich, A. J. Propagating elastic vibrations dominate thermal conduction in amorphous silicon. en. *Physical Review B* **97** (2018).
   https://doi.org/10.1103/PhysRevB.97.024201
   J. M. and A. J. M. conceived the idea. J. M. performed and analyzed the simulation results. J. M. wrote the manuscript.

7. Moon, J. & Minnich, A. J. Sub-amorphous thermal conductivity in amorphous heterogeneous nanocomposites. en. *RSC Advances* **6,** 105154–105160 (2016).
   https://doi.org/10.1039/C6RA24053D
   J. M. and A. J. M. conceived the idea. J. M. performed and analyzed the simulation results. J. M. wrote the manuscript.

TABLE OF CONTENTS

LIST OF ILLUSTRATIONS

LIST OF TABLES

Chapter 1

PHENOMENOLOGY OF THERMAL PROPERTIES OF GLASSES

The term, *amorphous*, comes from ancient Greek, *ámorphos*, which means "without form". Amorphous or non-crystalline solids are, therefore, defined as solids that lack the long-range order. Various classifications of solids fall into the "amorphous" category ranging from amorphous polymers and ceramics to random alloys and metallic glasses. For clarification, glasses are technically amorphous solids that go through the glass transition from their liquid states, but the terms amorphous solids and glasses are often used interchangeably and this is also the case in this thesis. Despite the abundance of glasses and millenia of glass usage, it may come as a surprise that we understand very little about them. Nobel Laureate Philip Anderson famously wrote a viewpoint in *Science* [1] in 1995 saying, "The deepest and most interesting unsolved problem in solid state theory is probably the theory of the nature of glass and the glass transition." Decades later, this statement still remains relevant to this day in atomic dynamics and thermal properties in amorphous materials.

As a starting point of this thesis, a high level picture of some of the universal features of amorphous solids (non-metals) in their thermal properties is described. Comparing with crystals, we find that there exist some anomalous temperature dependent thermal properties. Some phenomenological models including tunneling two level systems (TLS) and minimum thermal conductivity models to explain these features are explored in this chapter.

1.1 Temperature dependent thermal conductivity and heat capacity of glasses

Temperature dependent thermal conductivity of various crystals and glasses is shown in Fig. 1.1 [2]. Some metals are also shown for reference, but the focus of the discussion is with regards to non-metallic solids in which phonons dominate the thermal conduction rather than electrons as in metals. In the temperature range shown, we see a wide range of thermal conductivity values of ~ 7 orders of magnitude. There are large variations of thermal conductivity among crystals depending on the composition and atomic structure. Take sapphire and black phosphorus at 30 K, for instance. A factor of 10^4 differences in thermal conductivity is observed. On the other hand, we see a stark difference for amorphous solids in that they exhibit more uniform thermal conductivity in all temperature ranges

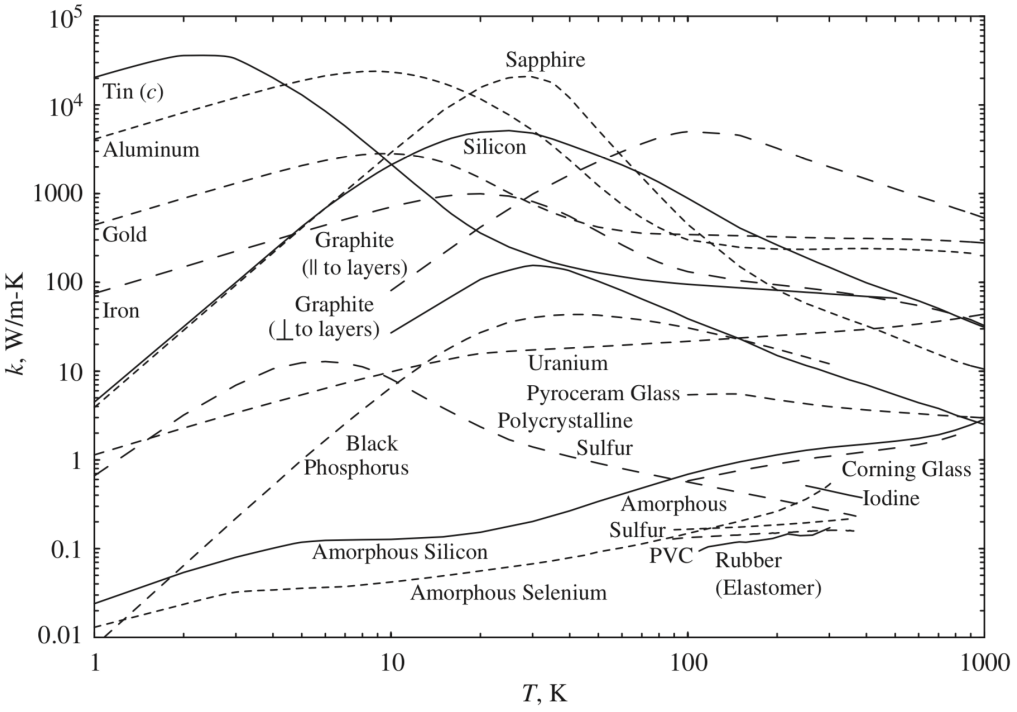

Figure 1.1: Temperature dependent thermal conductivity of various crystals and glasses [2].

regardless of the composition and local atomic structures. Another obvious trend we see from Fig. 1.1 is that crystals have orders of magnitude larger thermal conductivity than amorphous solids, which highlights the role of disorder in reducing the thermal conductivity. For instance, crystalline silicon (c-Si) has two orders of magnitude higher thermal conductivity compared to amorphous silicon (a-Si) at room temperature, while they have the same composition and similar density (2.3 gcm^{-3} for c-Si and 2.1 to 2.2 gcm^{-3} for a-Si). Because of the intrinsically low thermal conductivity, amorphous solids are considered to set the lower boundary of thermal conductivity for fully dense solids, also known as the amorphous limit, and motivated the development of minimum thermal conductivity models [3–6], which will be discussed in detail in a later section.

A signature thermal conductivity trend for a crystal is demonstrated in crystalline silicon (c-Si). At very low temperatures below a few K, phonon population is scarce and with the lack of disorder scattering for a perfect crystal and small phonon-phonon interactions, phonons can travel far distances on the order of bulk sample sizes; hence the thermal conductivity closely follows temperature dependence of the heat capacity at these temperatures ($C_v \, \alpha \, T^3$). As the temperature increases further,

more phonons are populated and they start to scatter with each other more strongly, leading to a reduction in thermal conductivity. The above qualitative description of temperature dependent thermal conductivity in crystals is widely accepted and is written in many standard solid state physics textbooks [7, 8].

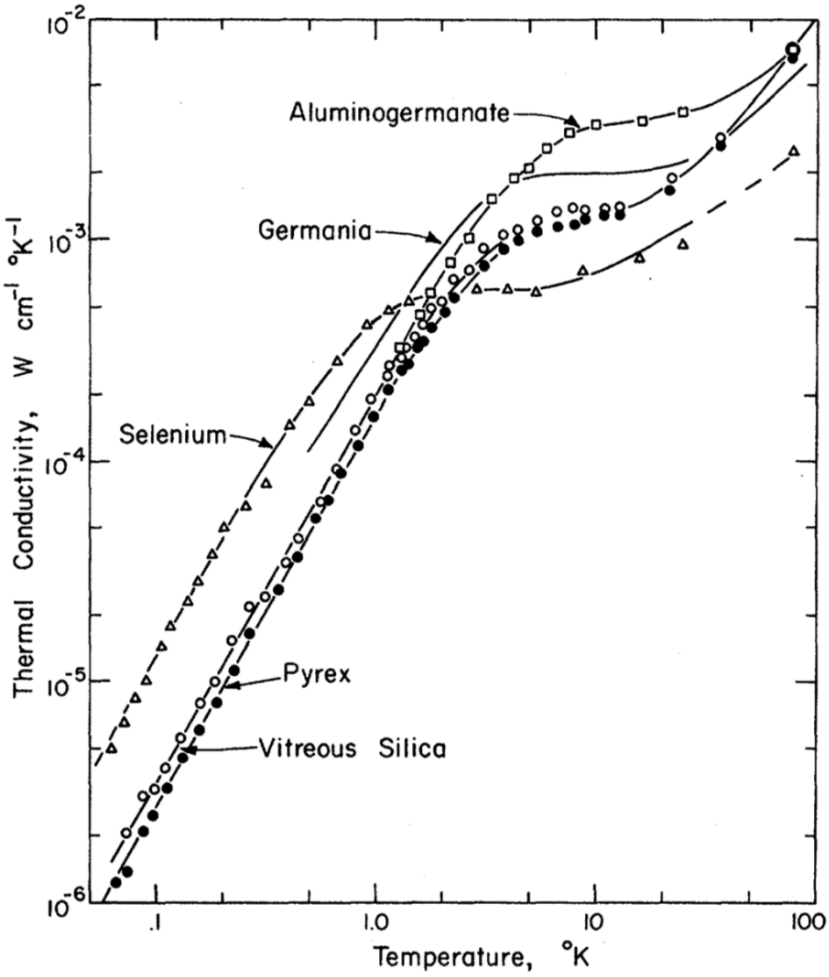

Figure 1.2: Thermal conductivity of various glasses at low temperatures from Zeller and Pohl [9]. Below around 1 K, we see a T^2 dependence in the thermal conductivity.

We see a different temperature dependent thermal conductivity for glasses: a continuously increasing thermal conductivity with some materials exhibiting a plateau at around 10 K is observed. This strikingly different temperature dependence in thermal conductivity was first pointed out by Eucken more than a century ago in 1911 [10] and ignited decades of subsequent research efforts to understand the underlying physics of thermal properties in glasses.

Other commonly observed features in glasses are the thermal conductivity being

quadratic in temperature as shown in Fig. 1.2 while the specific heat being linear with temperature at low temperatures below around 1 K, first observed by Zeller and Pohl in 1971 [9]. Prior to this work, it was long thought that because the dominant phonons have low frequencies $\ll$ 1 THz and macroscopic wavelengths, vibrational properties of glasses could be treated as a Debye solid as in crystals where phonons are insensitive to microscopic structure in these temperatures. Subsequent phenomenological model called tunneling two level systems proposed independently by Phillips [11] and Anderson et al. [12] was able to explain these anomalous thermal properties below 1K, which is to be discussed further in a next section.

In addition to different temperature dependence in the specific heat, we generally see larger specific heat in glasses compared to their crystalline counterparts at low temperatures below 20 to 30 K. As an example, temperature dependent specific heat of silica glass and crystal is shown in Fig. 1.3 (**A**). The additional specific heat is related to a distinct feature in the vibrational density of states $g(E)$ called the Boson peak located around 5 meV when plotted in a reduced form $g(E)/E^2$ as depicted in Fig. 1.3 (**B**). The Debye model of density of states is plotted as a guide to the eye. Crystals such as α-quartz shown follow the Debye model for low energy excitations. The excess of specific heat and the boson peak are observed in many glasses and have been the focus of decades of work, but the conclusions do not yet converge to a unified answer to the origin of these anomalies [13–18].

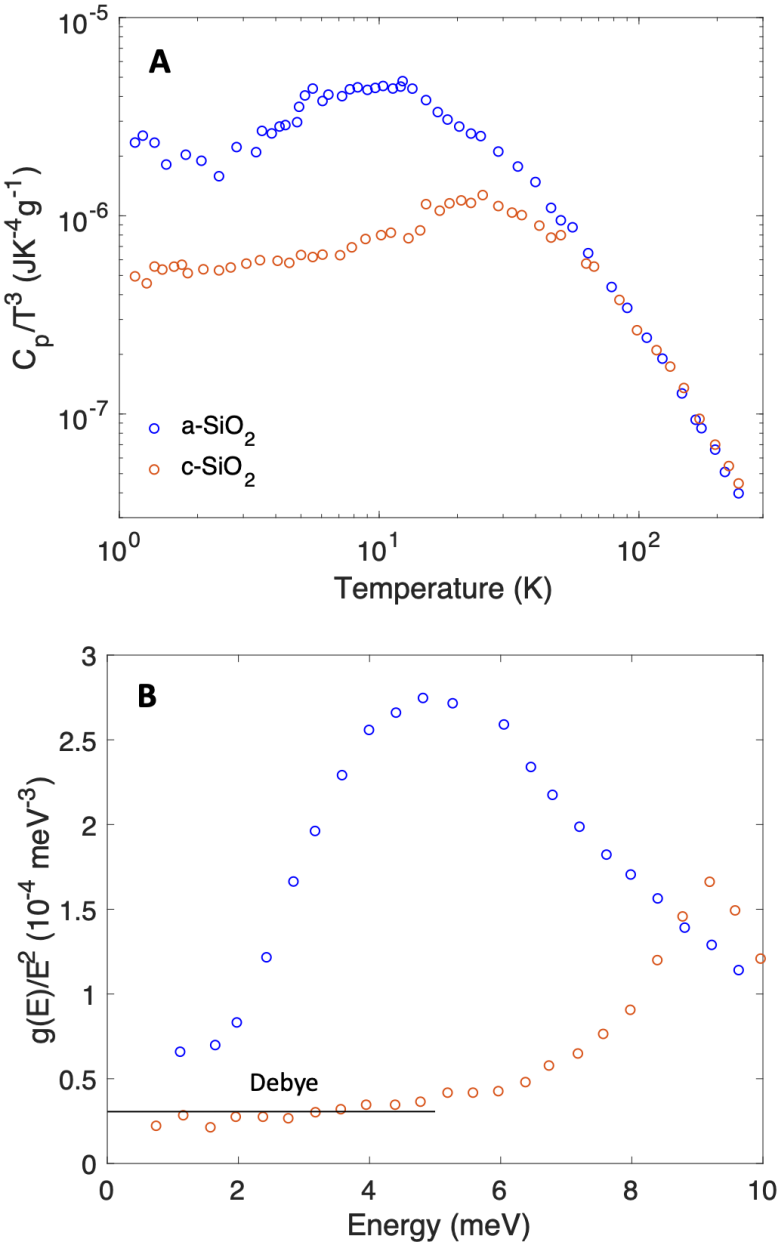

Figure 1.3: (**A**) Specific heat [9] and (**B**) reduced density of states [18] of amorphous silica (a-SiO_2, blue circle) and α-quartz (c-SiO_2, orange circle). Debye density of states is plotted as a guide to the eye. Excess of specific heat is clearly seen in a-SiO_2 at low temperatures below 20 to 30 K due to additional vibrational states over the α-quartz below a few meV.

1.2 Minimum thermal conductivity models

Now that some big differences in thermal properties between glasses and crystals are explored, we next discuss the minimum thermal conductivity models described briefly before.

Different trends in the temperature dependent thermal conductivity of crystals and glasses led to the interpretation by Kittel that the mean free paths are dominated by the disordered nature of the structure rather than the anharmonic lattice interactions in glasses [3]. Hence, it was hypothesized that average mean free paths are constant with temperature, and thermal conductivity closely follow the specific heat temperature dependence. Using the kinetic theory, the average mean free paths were calculated to be a few Å in glasses and comparing the calculated average mean free paths of quartz glass, crown glass, and flint glass, Kittel concluded that impurities give additional scattering.

In 1911, Einstein [19] was trying to understand the thermal conductivity of crystals rather than glasses from the measurements by Eucken [10]. He considered a simple cubic lattice and each atom to be a harmonic oscillator with the same frequency of vibration. The harmonic oscillator coupling was extended up to the third nearest neighbors. Requiring that the phases of the oscillators to be uncorrelated, the energy diffuse from an oscillator to the other during half the period of oscillation. It was later shown, however, that the lattice vibrations of crystals are better described by elastic waves traveling at the speed of sound in a correlated motion of neighboring atoms by Born and von Kármán [20] and Debye [21]. Nonetheless, Einstein's model of energy diffusion in the harmonic oscillators became useful to describe thermal conductivity of glasses as described below.

Plugging in half the period of oscillators as the phonon lifetime, Einstein specific heat, and the average distance between atoms as the phonon mean free paths to the kinetic theory of thermal conductivity, Cahill and Pohl expressed the Einstein model of thermal conductivity as [4]

$$k_{Eins} = \frac{k_B^2 n^{1/3}}{\hbar\pi}\Theta_E \frac{x^2 e^x}{(e^x-1)^2} \tag{1.1}$$

where k_B is the Boltzmann constant, n is the number density, Θ_E is the Einstein temperature, and $x = \Theta_E/T$. The Einstein model of thermal conductivity can qualitatively describe the temperature dependence of thermal conductivity measurements of glasses where we see a positive correlation with temperature as seen in Fig. 1.4. However, the predicted thermal conductivity can vary by a few orders of magnitude

with measurements at low temperatures below 50 K [4] and the determination of the Einstein frequency or temperature is arbitrary [22]. It is worth mentioning here that recently an apparent discrepancy between thermal conductivity measurements and the calculations based on the correlated motion of atoms as mentioned previously were observed in a single crystal with low thermal conductivity ($<\sim 1$ $Wm^{-1}K^{-1}$) and Einstein model of thermal conductivity has been successfully implemented to fill this gap as a second channel of heat conduction on top of the correlated atomic motion [23].

To circumvent the arbitrariness of the Einstein frequency, Cahill and Pohl combined the Debye model and Einstein model to express the thermal conductivity as

$$k_{min} = \frac{\pi}{6}^{1/3} k_B n^{2/3} \sum_i v_i \left(\frac{T}{\Theta_i}\right)^2 \int_0^{\frac{\Theta_i}{T}} \frac{x^3 e^x}{(e^x - 1)^2} dx \tag{1.2}$$

where the sum is taken over the three branches of sound each with speed of sound v_i, $\Theta_i = v_i(\hbar/k_B)(6\pi^2 n)^{1/3}$ is the Debye cut-off frequency for each branch. This thermal conductivity model (also known as the minimum thermal conductivity), therefore, describes each vibration traveling at the speed of sound with the lifetime equal to the half the period of the oscillation [4]. Despite the simplicity of the model (only density, sound velocities, and temperature needed as input), it has become quite successful in predicting the thermal conductivity measurements of various amorphous solids at room temperature as shown in Fig. 1.5. However, similar to k_{Eins}, the minimum thermal conductivity model fails by orders of magnitude at low temperatures as shown in Fig. 1.4, emphasizing that more sophisticated atomic dynamics models are necessary to fully describe the thermal conductivity of amorphous solids.

1.3 Two level systems

As mentioned before, the tunneling two level systems (TLS) can explain low temperature ($\leq \sim 1$ K) anomalies in the thermal properties of glasses well. The central assumption of the TLS model is that there are a number of atoms or groups of atoms which can sit in two nearly degenerate asymmetric equilibrium positions as shown in Fig. 1.6. In this model, there are two ways that phonons can attenuate via interacting with TLS: resonance absorption and structural relaxation.

The Hamiltonian that describes the TLS with the ground states in the double-well

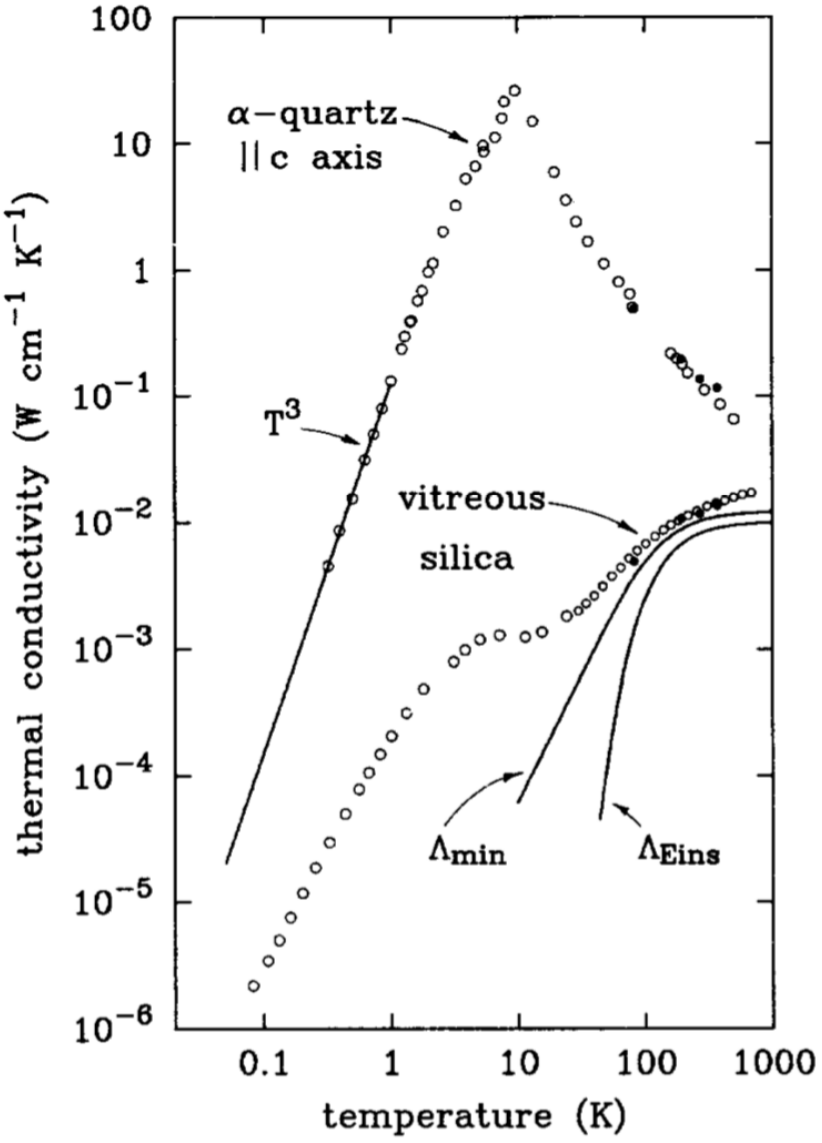

Figure 1.4: Thermal conductivity of crystalline and amorphous SiO_2 [4]. The solid circles are from Eucken [10] and the open circles are from [24, 25]. Λ_{Eins} and Λ_{min} denote Einstein model of thermal conductivity (k_{Eins}) and minimum thermal conductivity (k_{min}) by Cahill and Pohl [4] as discussed in the text.

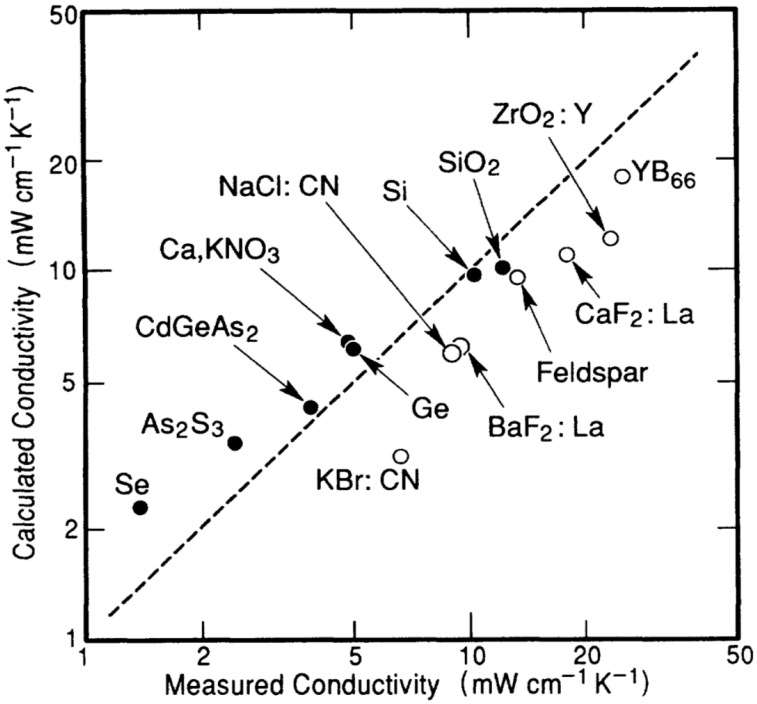

Figure 1.5: Thermal conductivity comparison of the calculations from Eq. (1.2) and measurements of various amorphous solids at 300 K [5]

potential can be written as

$$H_0 = \begin{pmatrix} \epsilon & \hbar\omega_0 e^{-\lambda} \\ \hbar\omega_0 e^{-\lambda} & -\epsilon \end{pmatrix}$$

where ϵ is the sum of the energy difference between two local minima potential energies and the energy difference between the zero-point motion energies about these local minima, $\hbar\omega_0$ is an energy of the order of the zero-point energy, and $e^{-\lambda}$ denotes the overlap between the wavefunctions with $\lambda = \left(\frac{2mV}{\hbar^2}\right)^{1/2}\Delta x$. The off-diagonal matrix elements, therefore, gives rise to tunneling from one position to the other. The eigenstates of H_0 then have energies

$$E_{1,2} = \pm\frac{1}{2}E \text{ with } E = \sqrt{\epsilon^2 + (\hbar\omega_0 e^{-\lambda})^2}. \tag{1.3}$$

The coupling between TLS eigenstates and phonons occurs through the deformation of the double-well potentials caused by an elastic wave. The deformation in potential in turn introduces a perturbation Hamiltonian H' as

$$H' = \frac{1}{2}\begin{pmatrix} \delta\epsilon & 0 \\ 0 & -\delta\epsilon \end{pmatrix}.$$

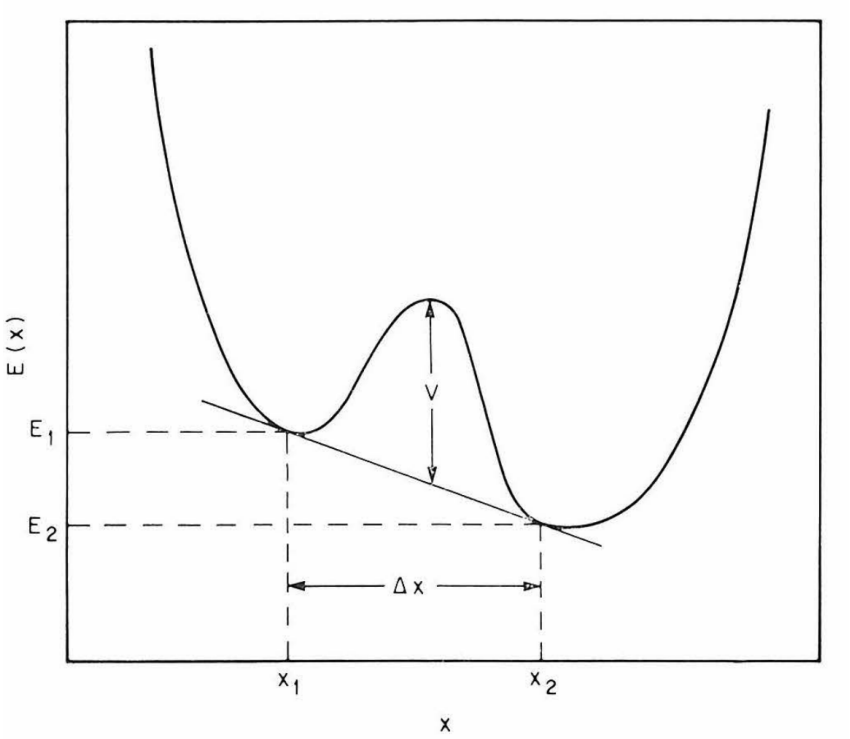

Figure 1.6: The double-well potential as a function of a generalized coordinate x [12]

Writing $\delta\epsilon$ in terms of a deformation potential parameter B and the elastic strains by phonon creation and annhilation operators, the matrix elements for absorption of a phonon with wavevector $\boldsymbol{k}$ and polarization α can be obtained through

$$\langle \boldsymbol{k}, \alpha, 2|H'|1\rangle = \left(\frac{k}{2\rho v_\alpha}\right)^{\frac{1}{2}} \frac{B\hbar\omega_0 e^{-\lambda}}{E}. \tag{1.4}$$

where ρ is the density of the glass and v_α is the sound velocity in the given polarization. Using the Fermi's golden rule, the phonon lifetime τ_{res} via the resonance absorption by the TLS can be then written as

$$\tau_{res}^{-1} = \frac{A\hbar\omega v_\alpha}{k_B}\tanh\left(\frac{\hbar\omega}{2k_BT}\right). \tag{1.5}$$

Here $A = \frac{\pi B^2 g_0 k_B}{\rho v_0^3 \hbar}$ and the energy density of two-level systems has been assumed to have the constant value g_0 and it is this assumption that leads to the linear dependence in the specific heat as

$$C(T) = \int_0^\infty n_0 \frac{E^2}{4k_BT^2}\mathrm{sech}^2\left(\frac{E}{2k_BT}\right)dE \tag{1.6}$$

where n_0 is the constant density of states. Evaluating the integral leads to

$$C(T) = \frac{\pi^2}{6} n_0 k_B^2 T \tag{1.7}$$

which recovers the experimentally observed linear dependence in temperature. These tunneling states scatter the phonons which gives the quadratic dependence in temperature for the thermal conductivity below 1 K, consistent with experiments [26].

At higher temperatures, the relaxation of the tunneling states results in additional phonon attenuation. Briefly, the mean free paths (l_{rel}) of phonons by the relaxation process can be obtained by solving two coupled Boltzmann transport equations of the TLS and phonon distribution functions [27] and can be expressed as [28]

$$l_{rel}^{-1} = \frac{A}{2}\left(\frac{k_B}{\hbar\omega} + \frac{1}{DT^3}\right)^{-1} \tag{1.8}$$

with $D = \frac{\pi^2 k_B^2}{12\rho\hbar^3}\sum_\alpha \frac{B^2}{v_\alpha^5}$. Combining the phonon attenuation from the absorption and relaxation, we obtain an overall inverse mean free paths from TLS as

$$l_{TLS}^{-1}(\omega, T) = \frac{A}{2}\left[\frac{2\hbar\omega}{k_B}\tanh\left(\frac{\hbar\omega}{2k_BT}\right) + \left(\frac{k_B}{\hbar\omega} + \frac{1}{DT^3}\right)^{-1}\right]. \tag{1.9}$$

The calculated thermal conductivity from the TLS mean free paths above [28] and the measurements [9] below 1 K for amorphous silica are shown in Fig. 1.7. We see a good agreement between the two and $k \sim T^2$ is observed for the TLS predictions in this temperature range. Besides the good agreement between the predictions of heat capacity and thermal conductivity with measurements, there are other experimental evidences to support the TLS predictions such as the saturation and non-linear effects of the resonant absorption when the ultrasonic waves have large amplitudes [27, 29]. Despite the huge success, it is currently unknown if the TLS model is the unique explanation of the low-temperature properties of glasses [30].

It is worth mentioning here that not all glasses exhibit the "typical" temperature dependence of glasses mentioned in §1.1. For instance, an ultra-stable glass of indomethacin (IMC) synthesized by a physical vapor deposition at a high temperature close to the glass transition temperature ($\sim 0.85\ T_g$) lacks the linear dependence in the specific heat at temperatures below 1 K. Instead, T^3 dependence, reminiscent of crystals are demonstrated in these temperatures as shown in Fig. 1.8. The dashed lines represent the corresponding linear fits $C_p = c_{lin}T + c_{cub}T^3$; hence, the y-axis

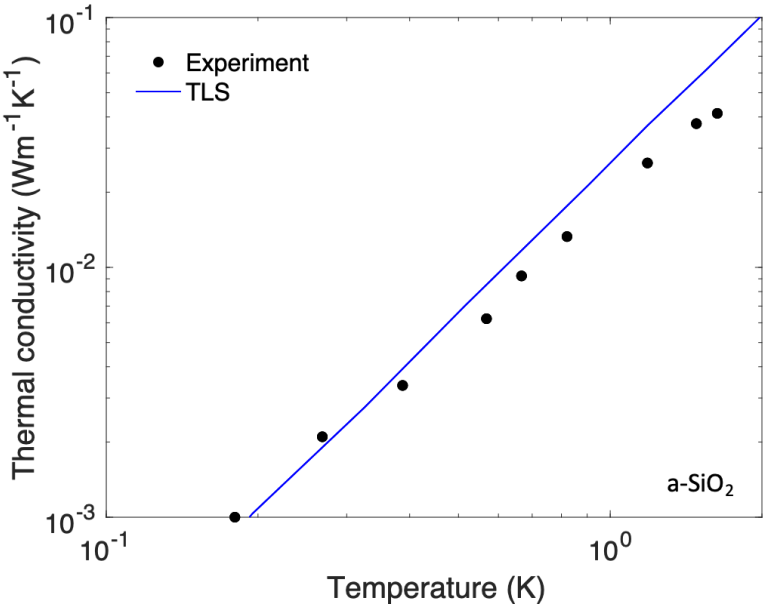

Figure 1.7: Temperature dependent thermal conductivity of amorphous silica from calculations (blue line) [28] based on Eq. (1.9) and from experiments (black circle) [9]

intercept in the Fig. 1.8 represents the degree of the linear specific heat contribution. The lack of the linear specific heat below 1 K in the ultra-stable IMC glass has been ascribed to the suppression of the TLS. The absence of TLS has also been reported in amorphous silicon (a-Si) synthesized at a high growth temperature of 673 K using e-beam evaporation [31]. The internal friction of a-Si which is proportional to the tunneling strength in the TLS model was measured to be within the experimental uncertainty of the background noise, indicative of the absence of the TLS. It will be, therefore, interesting to see if the specific heat of these a-Si at low temperature also lacks the linear dependence.

With these experimental evidence then, it is clear that the tunneling two level system is a very successful phenomenological model to describe the low temperature thermal properties in glasses where dominant phonons have macroscopic wavelengths and periods. However, for higher temperatures and for vibrations with mesoscopic wavelengths comparable to interatomic distances, TLS alone is not enough to capture the rich atomic dynamics in amorphous solids. For instance, an additional strong scattering regime such as $\tau \sim \omega^{-4}$ is needed to explain the plateau region at a few tens of K in thermal conductivity [28].

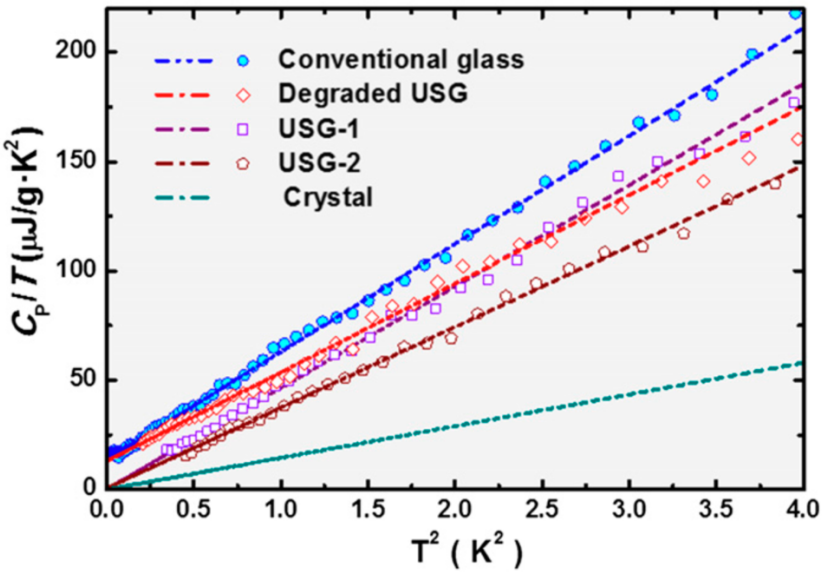

Figure 1.8: Specific heat measurements for several types of indomethacin (IMC) glass and crystal [32]. The conventional IMC (solid blue circle) was created by a melt-quench method with the cooling rate of 10 Ks^{-1}. USG stands for ultra-stable glass that is made by physical vapor deposition at a high temperature $\sim$ 0.85 T_g. Degraded USG represents a glass that was stored in a poor vacuum for 2 months. The dashed lines represent the corresponding linear fits $C_p = c_{lin}T + c_{cub}T^3$. USG glasses show no y-intercept, indicating that there is no linear specific heat contributions, similar to crystals.

1.4 Conclusion

Atomic dynamics in amorphous solids has been studied immensely for more than a century after anomalous thermal properties in glasses were first measured in 1911. Successful phenomenological models such as minimum thermal conductivity and tunneling two level states were developed to explain some of these anomalous features, but more complete theories are needed to fully describe the rich atomic dynamics in amorphous solids.

Subsequent efforts have utilized normal mode based methods to study thermal transport in amorphous solids. Assuming atoms vibrating around their equilibrium positions, these methods decompose atomic vibrations into normal modes and treat them as the fundamental heat carriers. Using some of these methods, we identify mechanisms to achieve ultralow thermal conductivity in fully dense amorphous nanocomposites in the next chapter and some common normal mode based methods are thoroughly introduced.

In our recent works, however, a careful analysis shows that there exist numerous discrepancies between the thermal conductivity predictions from the normal mode methods and measurements in amorphous solids. Pinpointing the precise origin of these discrepancies is challenging, but in the next chapters, it is demonstrated that some of the intrinsic assumptions made in normal modes, such as vibrating around equilibrium positions and normal modes being fundamental heat carriers, may not be valid. Instead, it is shown that collective acoustic excitations from the standard inelastic scattering theory, which do not rely on these assumptions, are consistent with experiments.

Chapter 2

SUB-AMORPHOUS THERMAL CONDUCTIVITY IN AMORPHOUS HETEROGENEOUS NANOCOMPOSITES

This chapter has been adapted from [33]:

Moon, J., Minnich, A. J., Sub-amorphous thermal conductivity in amorphous heterogeneous nanocomposites, *RSC Advances*, 2016

As previously mentioned in Chapter 1, pure amorphous solids are traditionally considered to set the lower bound of thermal conductivity due to their disordered atomic structure that impedes vibrational energy transport. However, the lower limits for thermal conductivity in heterogeneous amorphous solids and the physical mechanisms underlying these limits remain unclear. In this chapter, we use equilibrium molecular dynamics to show that an amorphous SiGe nanocomposite can possess thermal conductivity substantially lower than those of the amorphous Si and Ge constituents. To understand the low thermal conductivity, we first review some common normal mode methods such as normal mode lifetimes, Green-Kubo modal analysis, and Allen-Feldman theory. Using Allen-Feldman theory, it is demonstrated that the presence of the Ge inclusion localizes vibrational modes with frequency above the Ge cutoff in the Si host, drastically reducing their ability to transport heat. This observation suggests a general route to achieve exceptionally low thermal conductivity in fully dense solids by restricting the vibrational density of states available for transport in heterogeneous amorphous nanocomposites.

2.1 Introduction

Low thermal conductivity materials are desired for a wide range of applications ranging from thermoelectric power generators [34–39] to thermopile detectors [40]. As mentioned in Chapter 1, amorphous materials are considered to set the lower limit of thermal conductivity due to the disordered atomic structure that impedes the formation of propagating vibrations [2, 25, 41]. While in crystals heat is carried by propagating lattice waves, or phonons, in amorphous solids the lack of a periodic atomic structure results in other modes of thermal transport such as non-propagating vibrations for energy transport.

Allen and Feldman introduced categories of normal modes in amorphous solids known as propagons, diffusons, and locons [42, 43] (discussed more in detail in Chapter 3). Propagons are propagating and delocalized phonon-like plane waves that typically possess long wavelengths compared to the interatomic spacing. Diffusons are modes that scatter over a distance less than the interatomic distance and thus transport heat as a random-walk. Locons are non-propagating and localized modes that are unable to transport heat in harmonic solids [43, 44].

Although pure amorphous solids are typically assumed to achieve the lower limit of thermal conductivity, some works have examined how this limit may be broken. In semi-crystalline solids, it is well known that composites can possess exceptionally low thermal conductivity due to thermal boundary resistance [45]. This effect has been exploited by Chiritescu et al. [46] to achieve ultralow thermal conductivity in disordered WSe_2 nanolaminates below thermal conductivity predicted by the minimum thermal conductivity model [5], although a recent theory work suggests that the experiments agree with this model if anisotropy is taken into account [47]. Wingert et al. reported that crystalline silicon nanotubes with shell thicknesses as thin as 5 nm have a low thermal conductivity of 1.1 W/m-K, lower than that of the amorphous counterpart via a phonon softening effect [48]. Dechaumphai et al. experimentally observed an ultralow thermal conductivity of 0.33 ± 0.04 W/m-K at room temperature in amorphous multilayers made of Au and Si [49]. Computationally, Norouzzadeh et al. used MD to study the thermal conductivity of an a-SiGe alloy with different Ge content and observed thermal conductivity values below those of the constituent materials [50]. Giri et al. used NEMD to examine the role of the interface of amorphous SiGe superlattices and amorphous Si/heavy-Si superlattices, concluding that increasing mass-mismatch in amorphous superlattices results in higher Kapitza resistances, leading to low thermal conductivity [51].

Although these works have suggested that thermal conductivities of heterogeneous amorphous solids below those of the pure constituents are achievable, key questions remain. Some of these works have interpreted their results with a phonon gas model, which is of questionable validity for non-propagating vibrations, and others have used the concept of thermal boundary resistance to explain their observations. In particular, the latter approach implicitly assumes that vibrational modes of the two solids composing the interface are well defined. However, if the inclusion in the nanocomposite is sufficiently small, the vibrational modes of the composite may not coincide with the vibrations of the pure materials. In this case, the nature of the

vibrations in the composite solids, and hence the lower limits of thermal conductivity in heterogeneous amorphous solids, remain unclear.

Here, we examine heat transport in amorphous SiGe nanocomposites consisting of a Ge inclusion in a Si host matrix. We find that these structures can possess thermal conductivities that are significantly smaller than those of the constituent materials, with the minimum thermal conductivity reaching as low as 32% of that of the amorphous Si host. Normal mode analysis demonstrates that the presence of the Ge cluster drastically enhances localization of vibrational modes with frequency above the Ge cutoff in the Si host, leading to a remarkable decrease in thermal conductivity. These results demonstrate a mechanism for achieving remarkably low thermal conductivity in fully dense amorphous materials that may be useful for solid-state thermal insulation and highly sensitive thermopile detectors.

2.2 Normal mode methods

In normal mode analysis, the atomic displacements around an equilibrium position for atom j in unit cell l are expanded in plane wave solutions in harmonic oscillator approximation as shown below.

$$\boldsymbol{u}(jl,t) = \sum_{\boldsymbol{k},\nu} \boldsymbol{U}(j,\boldsymbol{k},\nu) e^{i[\boldsymbol{k}\cdot\boldsymbol{r}(jl)-\omega(\boldsymbol{k},\nu)t]} \tag{2.1}$$

where $\boldsymbol{k}$ is the wave vector, ω is the angular frequency, ν is the branch, and $\boldsymbol{U}(j,\boldsymbol{k},\nu)$ is the amplitude vector. More commonly in phonon transport literature, the above equation is re-written as

$$\boldsymbol{u}(jl,t) = \frac{1}{(Nm_j)^{1/2}} \sum_{\boldsymbol{k},\nu} \boldsymbol{e}(j,\boldsymbol{k},\nu) e^{i\boldsymbol{k}\cdot\boldsymbol{r}(jl)} Q(\boldsymbol{k},\nu,t) \tag{2.2}$$

where N is the number of atoms, $\boldsymbol{e}(j,\boldsymbol{k},\nu)$ is the mode eigenvector, m is the mass and $Q(\boldsymbol{k},\nu,t)$ is the Fourier transform of (2.2) as shown below

$$Q(\boldsymbol{k},\nu,t) = \frac{1}{N^{1/2}} \sum_{jl} m_j^{1/2} e^{-i\boldsymbol{k}\cdot\boldsymbol{r}(jl)} \boldsymbol{e}^*(j,\boldsymbol{k},\nu) \cdot \boldsymbol{u}(jl,t). \tag{2.3}$$

The complex quantity, $Q(\boldsymbol{k},\nu,t)$, is named the normal mode coordinate. Many thermodynamic and dynamic properties such as heat capacity and root-mean-square displacements can then be decomposed in terms of these normal modes with the caveat that explicit assumption of vibration around equilibrium position and plane wave solutions has been made. For interested readers for more details about normal mode decomposition of such properties, Ref. [52] and [2] are recommended.

In subsequent subsections, three commonly used normal mode methods such as normal mode lifetimes, Green-Kubo modal analysis, and Allen-Feldman theory are introduced in detail. In addition to the assumption that atoms vibrate around their equilibrium positions, these methods treat normal modes as fundamental heat carriers.

Normal mode lifetimes

The Hamiltonian of a system of harmonic oscillators can be expressed equivalently in both the real space and the normal mode space as follows

$$H = \frac{1}{2}\sum_{jl} m_j |\dot{\boldsymbol{u}}(jl,t)|^2 + \frac{1}{2}\sum_{jj',ll'} \boldsymbol{u}^T(jl,t)\cdot\Phi(jj',ll',t)\cdot\boldsymbol{u}(j'l',t) \tag{2.4}$$

and

$$H = \frac{1}{2}\sum_{\boldsymbol{k},\nu} \dot{Q}(\boldsymbol{k},\nu,t)\dot{Q}(-\boldsymbol{k},\nu,t) + \frac{1}{2}\sum_{\boldsymbol{k},\nu}\omega^2(\boldsymbol{k},\nu)Q(\boldsymbol{k},\nu,t)Q(-\boldsymbol{k},\nu,t). \tag{2.5}$$

where dot over a variable represents time derivative, superscript T represent transpose, and $\Phi(jj',ll',t)$ is the force constant matrix. The first terms and the second terms in the above Hamiltonian expressions are kinetic energy and potential energy, respectively. The instantaneous, total energy of each mode of a classical system is then

$$H_{\boldsymbol{k},\nu} = \frac{1}{2}\dot{Q}(\boldsymbol{k},\nu,t)\dot{Q}(-\boldsymbol{k},\nu,t) + \frac{1}{2}\omega^2(\boldsymbol{k},\nu)Q(\boldsymbol{k},\nu,t)Q(-\boldsymbol{k},\nu,t). \tag{2.6}$$

However, the harmonic expression above is not exact at finite temperature as vibrational modes start interacting with one another. One can imagine that for harmonic oscillators, there is no damping of the vibration, leading to infinite lifetime and thermal conductivity, which is not physical for real materials at finite temperature. To account for the mode interactions, displacements from molecular dynamics (MD) at a desired finite temperature which account for all degrees of anharmonicities are used instead and projected to the normal mode coordinates, the temporal decay of the autocorrelation of $H_{\boldsymbol{k},\nu}$ is then related to the relaxation time of that mode by [2, 53]

$$\frac{H_{\boldsymbol{k},\nu}(t)H_{\boldsymbol{k},\nu}(0)}{H_{\boldsymbol{k},\nu}(0)H_{\boldsymbol{k},\nu}(0)} = e^{-\frac{t}{\tau_{\boldsymbol{k},\nu}}} \tag{2.7}$$

A typical normalized total energy autocorrelation for a mode is shown in Fig. 2.1 [2]. As expected, we see an exponential decay in the normalized energy autocorrelation and the lifetime can be extracted as discussed. Normalized potential energy autocorrelation is also plotted in the same figure. The vibration frequency of the

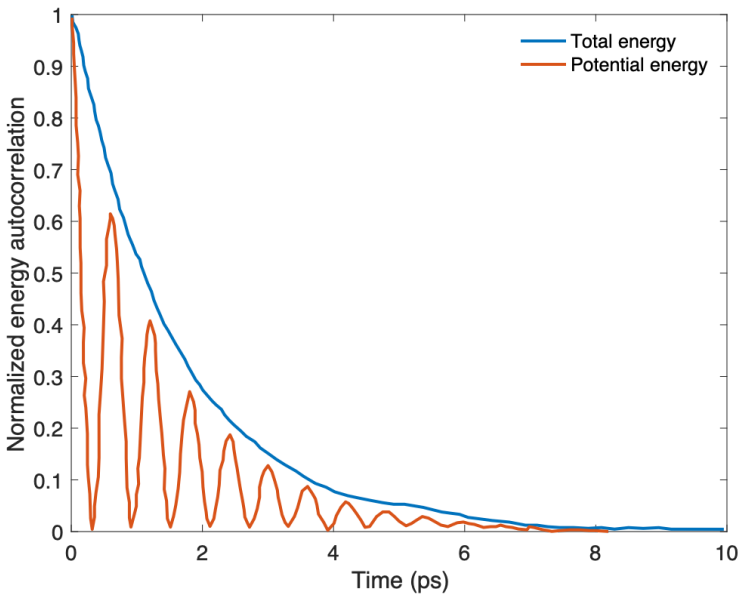

Figure 2.1: A typical normalized energy autocorrelation for the relaxation time calculations as adapted from [2]. Blue and orange solid lines correspond to normalized total energy and potential energy autocorrelations of a mode, respectively. We see an exponential decay in the total energy autocorrelation as expected. The vibration frequency of the mode is one half of the oscillation frequency observed in the potential energy autocorrelations.

mode is half of the oscillation frequency in the potential energy autocorrelation. The normal mode lifetime calculations can also be done in the frequency space in which we see a peak with a Lorentzian linewidth (full width at half maximum) which corresponds to the peak frequency and the inverse of lifetime of the mode, respectively.

The normal mode lifetime calculation scheme mentioned above is general for both crystals and amorphous solids. However, it is important to note that for amorphous solids all the normal mode analysis is done at the $\Gamma(\boldsymbol{k} = 0)$ point due to the lack of translational symmetry, which is equivalent to treating the entire computational domain as one supercell. Hence, group velocities ($\frac{d\omega}{dk}$) of these normal modes are not directly found and some assumptions have to be made to calculate the thermal conductivity utilizing normal mode lifetimes, which will be discussed further in the next chapter. Now that the essence of the normal mode lifetime calculations is introduced, we next explore the Green-Kubo modal analysis (GKMA).

Green-Kubo modal analysis

Green-Kubo modal analysis is a method to decompose the heat flux into the time derivative of normal mode coordinates in the Green-Kubo formalism to calculate the thermal conductivity [54]. According to the Green-Kubo formalism, thermal conductivity tensor is given by

$$k_{\alpha\beta} = \frac{V}{k_B T^2} \int \langle J_\alpha(t + t') J_\beta(t) \rangle dt' \tag{2.8}$$

where the angled bracket notation is the ensemble average, subscripts α and β denote cartesian directions, V is the volume of the system, k_B is the Boltzmann constant, T is the temperature, and J is the heat flux and is expressed as [55]

$$\boldsymbol{J} = \frac{1}{V} \left[\sum_i E_i \boldsymbol{v}_i + \frac{1}{2} \sum_{i,j} (\boldsymbol{F}_{ij} \cdot \boldsymbol{v}_i) \boldsymbol{r}_{ij} \right] \tag{2.9}$$

where the summation is over atoms. It is worth mentioning that sometimes in literature, the Green-Kubo thermal conductivity is written in terms of heat current, $\boldsymbol{S} = V\boldsymbol{J}$. So far, the Green-Kubo thermal conductivity with the above heat flux equation is general in that it can be used to calculate thermal conductivity of solids, liquids, and gases. Assuming atoms vibrating with respect to their equilibrium positions, velocity in (2.9) is decomposed into time derivative of normal modes as [54]

$$\boldsymbol{v}_i(t) = \sum_n \boldsymbol{v}_i(n,t) = \frac{1}{m_i^{1/2}} \sum_n \boldsymbol{e}(i,n) \dot{Q}(n,t) \tag{2.10}$$

where the sum is over all the modes. To reach this expression, we have treated the entire computational domain as one supercell as mentioned before. Substituting (2.10) into (2.9), we obtain the individual modal contribution to heat flux as

$$\boldsymbol{J}(n,t) = \frac{1}{V} \left[\sum_i E_i \left(\frac{1}{m_i^{1/2}} \boldsymbol{e}(i,n) \dot{Q}(n,t) \right) + \frac{1}{2} \sum_{i,j} \left\{ \boldsymbol{F}_{ij} \cdot \left(\frac{1}{m_i^{1/2}} \boldsymbol{e}(i,n) \dot{Q}(n,t) \right) \right\} \boldsymbol{r}_{ij} \right]. \tag{2.11}$$

Decomposition of heat flux into individual mode contribution enables mode resolved thermal conductivity as

$$k_{\alpha\beta,nn'} = \frac{V}{k_B T^2} \int \langle J_\alpha(n, t + t') J_\beta(n', t) \rangle dt'. \tag{2.12}$$

One can, therefore, examine how the correlation between pairs of modes contributes to thermal conductivity. The total thermal conductivity is then

$$k_{\alpha\beta} = \frac{V}{k_B T^2} \sum_{n,n'} \int \langle J_\alpha(n, t + t') J_\beta(n', t) \rangle dt'. \tag{2.13}$$

It is important to note that the thermal conductivity calculations based on GKMA account for all degrees of anharmonicity as the velocities which are decomposed into normal modes are from classical molecular dynamics.

Allen and Feldman theory

Allen and Feldman proposed a quantum mechanical theory in which heat is carried by decoupled harmonic oscillators [42, 56]. Extensive derivation of the theory is well-documented in Ref. [56]. Hence, only the important aspects of the derivations are covered here.

Heat flux is written with respect to the heat flux operator as

$$\boldsymbol{J} = tr(\rho \boldsymbol{S}) = -\boldsymbol{k} \cdot \nabla T \tag{2.14}$$

where tr is the trace. Assuming a system in steady state with a local space-dependent temperature $T(x) = [k_B \beta(s)]^{-1}$, the local density matrix is given by

$$\rho = \frac{e^{-\int d^3x \beta(x) h(x)}}{Z} \tag{2.15}$$

where $h(x)$ is the Hamiltonian density operator and Z is the partition function. Hamiltonian can, therefore, be written in terms of $h(x)$ as, $H = \int d^3x h(x)$. Under the harmonic approximation, the Hamiltonian is equivalent to (2.4). The Hamiltonian density operator, $h(x)$ and the heat flux density operator $\boldsymbol{S}(x)$ obey the condition of local energy conservation as

$$\frac{\partial h(x)}{\partial t} + \boldsymbol{\nabla} \cdot \boldsymbol{S}(x) = 0. \tag{2.16}$$

Now, recalling that the heat flux $\boldsymbol{J}$ vanishes in equilibrium when $\beta(x)$ is constant and assuming that the temperature fluctuations, $\delta T(x)$, is small, $\beta(x)$ can be expanded as

$$\beta(x) = \beta\left(1 - \frac{\delta T}{T}\right) \tag{2.17}$$

where β and T are corresponding average constants. Substituting the expression back to the local density matrix,

$$\rho = \frac{e^{-\beta(H+H')}}{Z} \tag{2.18}$$

$$H' = -\frac{1}{T} \int d^3x \delta T(x) h(x) \tag{2.19}$$

using the energy conversion condition to replace $h(x)$ by $\boldsymbol{S} = \frac{1}{V}\int d^3x\boldsymbol{S}(x)$ and with some algebra,

$$H' = -\frac{1}{T}\int_{-\infty}^{0} dt \int d^3x \nabla T(x) \cdot \boldsymbol{S}(t) \tag{2.20}$$

taking $\nabla T(x)$ as a constant,

$$H' = -\frac{V\nabla T}{T}\int_{-\infty}^{0} dt\boldsymbol{S} \tag{2.21}$$

recognizing that the density matrix can be expanded in powers of the Hamiltonian perturbation,

$$\rho = \frac{e^{-\beta(H+H')}}{Z} = \frac{e^{-\beta H}}{Z}\left(1 + \int_0^\beta d\lambda e^{\lambda H} H' e^{-\lambda H} + ...\right). \tag{2.22}$$

When carrying out $tr(\rho\boldsymbol{S})$, the first term is zero due to constant β and the perturbation from the equation above leads to $-\boldsymbol{k} \cdot \nabla T$. The thermal conductivity can, therefore, be written as

$$k_{\alpha\beta} = \frac{V}{T}\int_0^\beta d\lambda \int_0^\infty \langle e^{\lambda H} S_\alpha(t) e^{-\lambda H} S_\beta(0)\rangle \tag{2.23}$$

Time shifting the time integral and taking the Fourier transform of the above equation, we obtain

$$k_{\alpha\beta} = \frac{V}{T}\int_0^\beta d\lambda \int_0^\infty e^{i(\omega+i\eta)t}\langle S_\alpha(-i\hbar\lambda) S_\beta(t)\rangle \tag{2.24}$$

where $S(-i\hbar\lambda) \equiv e^{\lambda H} S e^{-\lambda H}$. It's worth mentioning that no assumption of normal modes have been made so far and the above equation is the Kubo formula for thermal conductivity. The classical version of the Green-Kubo thermal conductivity has been derived in Appendix C for completeness. Decomposing the heat current operator in terms of normal modes in the harmonic approximation, expressing the time dependence of the heat current operator in Heisenberg picture, and taking the real part of the thermal conductivity, we obtain

$$k = \frac{1}{V}\sum_i C_i(T) D_i \tag{2.25}$$

where $C_i(T)$ is the specific heat and D_i is the mode diffusivity given by

$$D_i = \frac{\pi V^2}{3\hbar\omega_i^2}\sum_{i\neq j} |S_{ij}|^2 \delta(\omega_i - \omega_j). \tag{2.26}$$

The matrix elements of the heat current operator is given by

$$S_{ij} = \frac{\hbar}{2V} \boldsymbol{v}_{\boldsymbol{K}ij}(\omega_{\boldsymbol{K}i} + \omega_{\boldsymbol{K}j})$$
$$\boldsymbol{v}_{\boldsymbol{K}ij} = \frac{i}{2\sqrt{\omega_{\boldsymbol{K}i}\omega_{\boldsymbol{K}j}}} \sum_{\alpha,\beta,m,\kappa,\kappa'} e_\alpha(\kappa;\boldsymbol{K},i) D^{\kappa'\kappa}_{\beta\alpha}(0,m)(\boldsymbol{R}_m + \boldsymbol{R}_{\kappa\kappa'}) e^{i\boldsymbol{K}\cdot\boldsymbol{R}_m} e_\beta(\kappa';\boldsymbol{K},j) \tag{2.27}$$

where $\boldsymbol{K}$ is the wavevector, α, β are the cartesian directions, m labels a unit cell, κ, κ' denote the atoms in the cell m, e with subscripts is the eigenvector, $D^{\kappa'\kappa}_{\beta\alpha}(0,m)$ is the Hermitian force constants. The above expression for $\boldsymbol{v}_{\boldsymbol{K}ij}$ is written for a periodic system, but can be simplified to amorphous solids by considering the entire domain as one unit cell.

The above thermal conductivity expression in Eq. 2.25 is termed Allen-Feldman thermal conductivity also denoted as k_{AF}. To summarize the derivations, temperature gradient in a disordered solid couples different harmonic eigenstates through the heat current operator (off-diagonal elements) which lead to the finite thermal conductivity while the diagonal elements contribute zero to the overall thermal conductivity confirming that the thermal conductivity using the above expressions is from non-propagating modes.

2.3 Results

Now that the fundamentals of commonly used normal mode analysis methods are discussed, we next look at how these standard normal mode methods can be used to study the origin of ultralow thermal conductivity in amorphous nanocomposite materials.

We calculated the thermal conductivity of amorphous Si and amorphous SiGe nanocomposites using equilibrium MD with the Stillinger-Weber (SW) interatomic potential [57]. The two types of structures studied are shown in Figure 2.2. The atomic configuration consisting of 4096 atoms was provided by N. Mousseau and was generated from the modified Wooten-Winer-Weaire (WWW) algorithm [58].

For na-SiGe structures, a cubic domain in the middle of the structure with side length a was replaced with heavier germanium atoms with appropriate coefficient changes in SW potential. SW potential coefficients for silicon and germanium interactions are described in Refs. [57, 59, 60] The side length, a, was chosen to be 10, 20, 25, 30, 35, 40, and 46.4 Å. These lengths represent 1, 10, 20, 35, 55, 82, and 100% Ge fraction, respectively. Periodic boundary conditions were

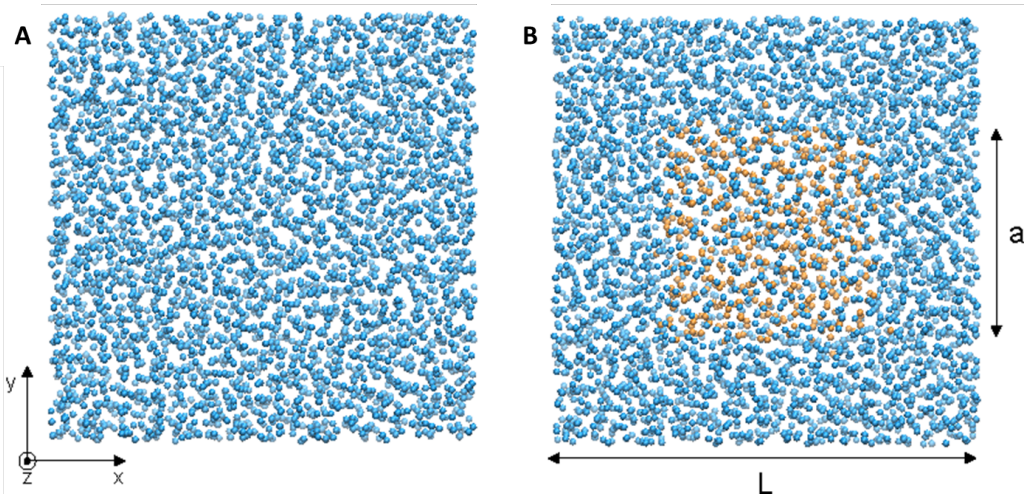

Figure 2.2: 4096-atom configurations of (**A**) amorphous silicon and (**B**) nanostructured amorphous silicon germanium. Blue atoms represent silicon and orange atoms represent germanium. The germanium cubic side length, a, varies from 10 Å to the side length of the entire domain, L = 46.4 Å.

imposed for all the structures. The MD simulations were performed with Large-scale Atomic/Molecular Massively Parallel Simulator (LAMMPS) [61] with a time step of 0.5 fs. The simulation procedure began with an anneal at 1000 K for 20 ns using the NPT ensemble to reduce metastabilities [44, 62]. We observed a decrease and plateau of the potential energy during the annealing process for each structure indicating a reduction of metastability.

Subsequently, the domain was quenched at a rate of 10 K/ps to 300 K and equilibrated in an NPT ensemble at 300 K for 20 ns to relax the structure to equilibrium pressure. Because volume and pressure fluctuate in MD simulations, we computed the average atom positions over the last 100 ps to ensure the domain was not under strain. The resulting mean pressure was on the order of 0.1 bar. This domain was then thermostatted in an NVT ensemble for 10 ns using a Nose-Hoover thermostat. After an additional NVE equilibration for 50 ps, the heat fluxes were computed for 1.6 ns in NVE ensemble.

We computed the thermal conductivity of the various structures using the Green-Kubo (GK) formalism, which relates the thermal conductivity to the heat current autocorrelation function as in Eq. (2.8). The thermal conductivity calculations reported in this study are based on the average of the integrals of the heat current autocorrelation functions (HCACF) from 10 simulations and the autocorrelations were calculated by the Wiener-Khinchin theorem derived in Appendix B.

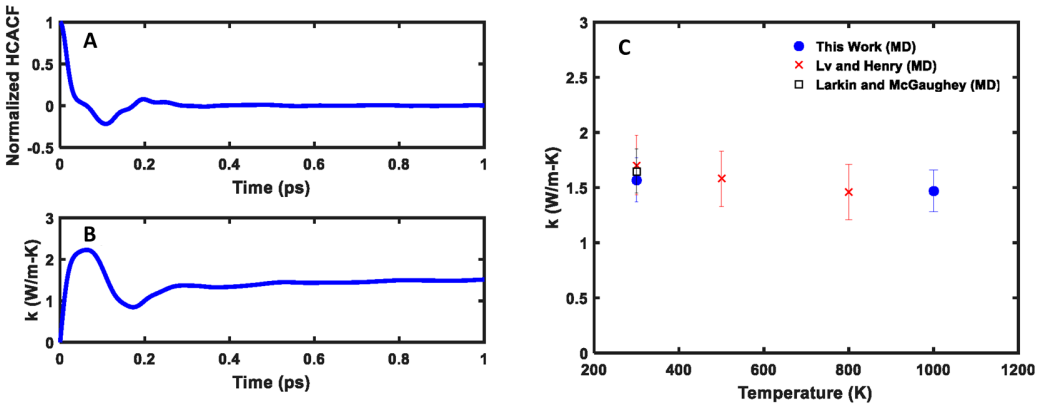

Figure 2.3: (**A**) Normalized heat current autocorrelation function versus time. (**B**) Thermal conductivity integral calculated by Eq 2.8 versus time. The thermal conductivity of a-Si is determined by taking the average between 5 and 20 ps. (**C**) Thermal conductivity versus temperature (blue circles), comparison with the works by Larkin and McGaughey (black squares) [44], and Lv and Henry (red crosses) [54] utilizing 4096 atoms, SW potential, and GK formalism at temperatures from 300 K to 1000 K. Negligible temperature dependence is observed.

Figure 2.3(**A**) shows the HCACF normalized by $\langle \mathbf{J}(0) \cdot \mathbf{J}(0) \rangle$ for a-Si. The autocorrelation function converges quickly to 0 in less than 0.5 ps for a-Si. The HCACF convergence times of na-SiGe are on the order of 10 ps. The resulting thermal conductivity of a-Si obtained from the integral of the autocorrelation function versus integration time is depicted in Figure 2.3(**B**). The thermal conductivity of a-Si is determined by taking the average between 5 and 20 ps. The thermal conductivity of a-Si with respect to temperature for 4096 atoms with SW potential is plotted in Figure 2.3(**C**) and compared with works by Larkin and McGaughey [44] and Lv and Henry [54]. At 300 K, thermal conductivity from this work is 1.55 ± 0.20 W/m-K which is in agreement with these works. Consistent with Ref [54], weak temperature dependence of thermal conductivity is observed.

We now examine the thermal conductivity of na-SiGe versus Ge content, shown in Figure 2.4. Pure amorphous Si and Ge have thermal conductivities of 1.55 ± 0.20 W/m-K and 0.99 ± 0.21 W/m-K, respectively. Interestingly, we observe thermal conductivities substantially smaller than either of these values for na-SiGe composites with Ge content ranging from 35% to 82%, with the minimum thermal conductivity of 0.50 ± 0.17 W/m-K achieved with 55% of Ge content. This value is less than a third of the original a-Si thermal conductivity and half that of a-Ge. Interestingly, it is even lower than the thermal conductivity of an amorphous

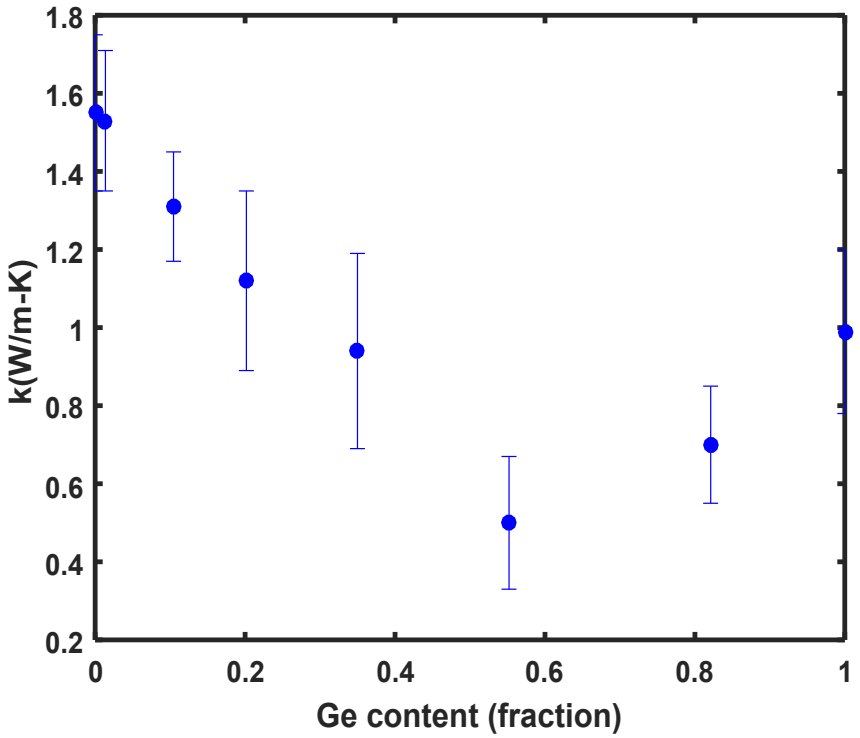

Figure 2.4: Thermal conductivity of na-SiGe versus Ge content. The minimum thermal conductivity of 0.50 ± 0.17 W/m-K is observed with 55% Ge content.

SiGe alloy with the same Ge content, which has a thermal conductivity of 0.78 ± 0.16 W/m-K. The percentage decrease of thermal conductivity in na-SiGe is nearly twice that in a-Si/a-Ge superlattices by an NEMD study by Giri et al. utilizing SW potential despite similar geometry [51].

To understand the mechanism behind the reduction in thermal conductivity, we first examine the vibrational density of states (vDOS) of the a-Si and a-Ge constituents in na-$Si_{0.45}Ge_{0.55}$ shown in Figure 2.5(**A**). The vDOS is computed from

$$g(\omega) = \sum_{m=1}^{3N_{atom}} \delta(\omega - \omega_m) = \frac{1}{3k_B T} \int_0^{\infty} \sum_{n=1}^{N_{atom}} m_n \langle \mathbf{v}(t) \cdot \mathbf{v}(0) \rangle e^{i\omega t} dt \qquad (2.28)$$

where N_{atom} is the number of atoms, T is the temperature, m_n is the mass of atom n, and $V_n(t)$ is the velocity of atom n at time t [63]. The vDOS of a-Si and a-Ge is similar to that of c-Si and c-Ge with distinct peaks at certain frequencies [51]. Due to absence of strong anharmonicity, only weak vibrational interaction of Si and Ge atoms is expected for frequencies greater than the frequency cutoff of a-Ge of 10 THz. In other words, we expect the vibrational modes with frequencies exceeding 10 THz to be confined to a-Si.

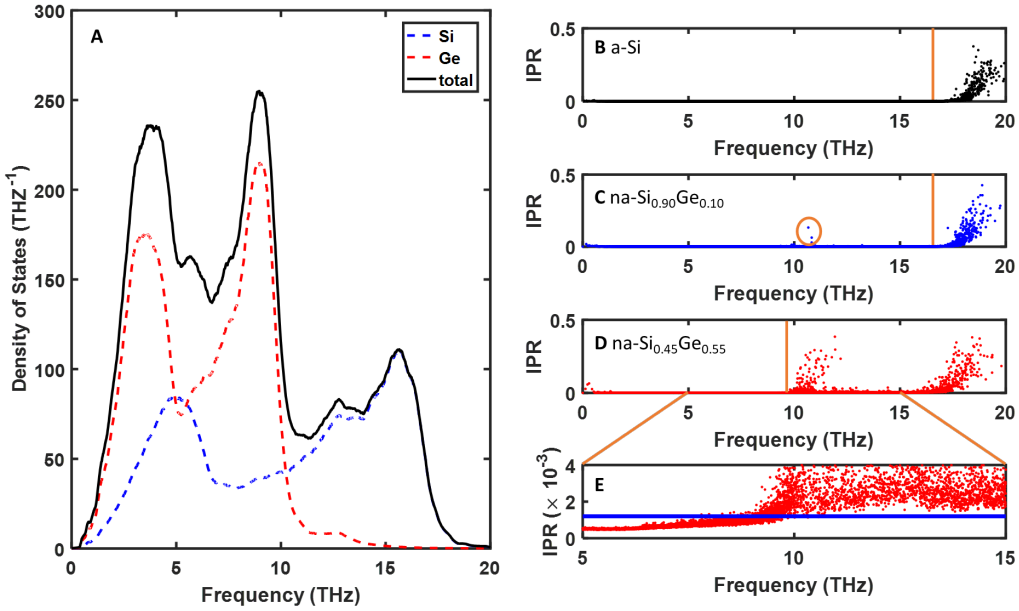

Figure 2.5: (**A**) The vibrational density of states of Si (blue dashed line) and Ge (red dashed line) constituents in na-$Si_{0.45}Ge_{0.55}$ along with the total density of states (black line). Inverse participation ratio (IPR) for (**B**) a-Si, (**C**) na-$Si_{0.90}Ge_{0.10}$, and (**D**) na-$Si_{0.45}Ge_{0.55}$. (**E**) Zoomed-in view of IPR of na-$Si_{0.45}Ge_{0.55}$ for frequencies from 5 to 15 THz where modes above the bold line are defined as locons. Vibrational modes start to be localized at 9 THz and are completely localized above 10 THz.

We confirm this hypothesis by first calculating the inverse participation ratio (IPR), which is a measure of how many atoms participate in the motion of a particular eigenmode. The IPR is given by

$$p_n^{-1} = \sum_i (\sum_\alpha e^*_{i\alpha,n} e_{i\alpha,n})^2 \tag{2.29}$$

where $e_{i\alpha,n}$ is the eigenvector component for atom i in α direction for the mode n. [64] The eigenvectors for each mode and atom are calculated by harmonic lattice dynamics in GULP [65] with relaxed structures from MD at 300 K. The IPR is defined so that it equals $1/N_{atom}$ if all atoms are participating, or 1 if the vibration is completely localized to one atom. Defining a specific IPR value that uniquely distinguishes locons is not possible, but vibrational modes with participation ratio less than 0.2 (corresponding to IPR greater than 0.0012 here) have been defined previously as localized modes [66, 67]. We therefore define locons according to this convention.

Figures 2.5(**B**)-(**E**) show the IPR for a-Si, na-$Si_{0.90}Ge_{0.10}$, na-$Si_{0.45}Ge_{0.55}$, and a zoomed-in view of the IPR of na-$Si_{0.45}Ge_{0.55}$ from 5 to 15 THz. The IPR for a-Si, Figure 2.5(**B**), shows that locons are observed primarily over around 17 THz, consistent with prior works [43, 54]. As Ge atoms are introduced in the nanocomposite in na-$Si_{0.90}Ge_{0.10}$, we observe locons in the medium-frequency region around 10 THz. For na-$Si_{0.45}Ge_{0.55}$, all the vibrational modes above around 10 THz are localized. The corresponding locon mode fractions are 7%, 9%, and 31% for a-Si, na-$Si_{0.90}Ge_{0.10}$, and na-$Si_{0.45}Ge_{0.55}$, respectively. In other words, na-$Si_{0.45}Ge_{0.55}$ has the lowest thermal conductivity and also more than 4 times the number of locons than a-Si, suggesting localized modes in Si are associated with the low thermal conductivity of the nanocomposite. We also note that vibrational modes with higher IPR than 0.0012 are present at low frequencies. We have verified that these modes are due to the finite size of the computational domain and disappear as the size of the system increases.

We next confirm that these localized modes reside in silicon by calculating the local vibrational density of states, defined as [68]

$$D_i(\omega) = \sum_n \sum_\alpha e^*_{i\alpha,n} e_{i\alpha,n} \delta(\omega - \omega_n) \tag{2.30}$$

where the sum is over Cartesian directions α and vibrational modes n for atom i. Furthermore, the spatial distribution of energy can be described as[67]

$$E_i = \sum_\omega (n_{BE} + \frac{1}{2}) \hbar\omega D_i(\omega) \tag{2.31}$$

where n_{BE} is the occupation number given by the Bose-Einstein distribution. We identify where the vibrational modes are localized by performing the sum only for vibrational modes that correspond to locons as identified by the IPR.

The spatial energy distribution is shown in Figures 2.6(**A**)-(**C**) for a-Si, na-$Si_{0.90}Ge_{0.10}$, and na-$Si_{0.45}Ge_{0.55}$, respectively. The distribution has been normalized by the maximum energy of an atom in the domain. We plot cross section x-y plane in the middle of z axis for clear visualization. It is apparent that for a-Si the spatial distribution of locons is randomly distributed. As Ge content is increased, however, we observe that locons are located in Si atoms. This result confirms that vibrational modes over around 10 THz are increasingly localized as Ge content grows and that these locons are indeed localized in a-Si atoms.

The drastic increase in locon population in na-SiGe suggests that the origin of the low thermal conductivity in na-SiGe is due to conversion of delocalized modes in

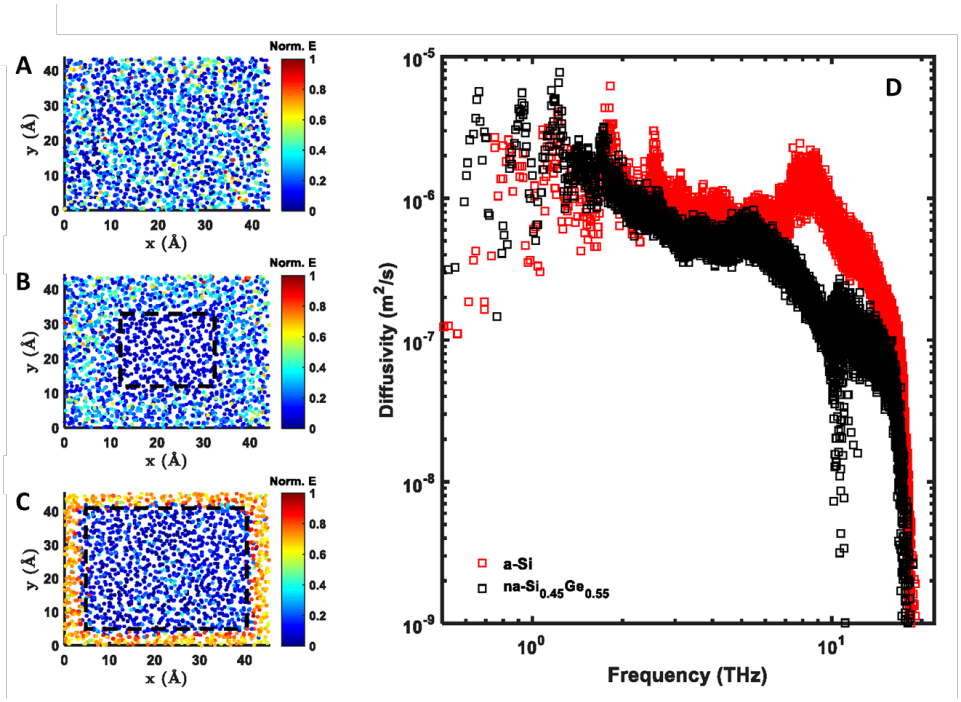

Figure 2.6: Normalized spatial energy distribution of the cross section XY plane in the middle of z axis for (**A**) a-Si, (**B**) na-$Si_{0.90}Ge_{0.10}$, and (**C**) na-$Si_{0.45}Ge_{0.55}$. Individual circles in the figure represent atoms and dashed lines represent the boundaries between Si and Ge atoms. Color indicates the degree of localization at an atom with red indicating high localization. (**D**) Spectral thermal diffusivities of a-Si and na-$Si_{0.45}Ge_{0.55}$ versus mode frequency. Thermal diffusivities decrease significantly for vibrational modes with frequencies higher than 10 THz in na-$Si_{0.45}Ge_{0.55}$ compared to those in a-Si.

a-Si to locons. To verify this hypothesis, we calculate the thermal diffusivities using the harmonic heat flux operator from Allen-Feldman theory discussed earlier. The thermal conductivity of a solid is given by

$$k = \frac{1}{V}\sum_i C(\omega_i) D_{th}(\omega_i) \tag{2.32}$$

where V is the volume of structure, $C(\omega_i)$ is the specific heat, $D_{th}(\omega_i)$ is the thermal diffusivity of frequency ω_i, and the summation is over modes. For diffusons under harmonic Allen-Feldman (AF) theory, the thermal diffusivity is calculated by

$$D_{AF}(\omega_i) = \frac{\pi V^2}{\hbar^2 \omega_i^2}\sum_{j\neq i} |S_{ij}|^2 \delta(\omega_i - \omega_j) \tag{2.33}$$

where S_{ij} is the heat current operator in the harmonic approximation [56]. Feldman et al. demonstrated that diffusivity calculations based on Peierls-Boltzmann theory

(phonon gas model) for low frequency propagon modes coincide reasonably well with D_{AF} in the low frequency range [68]. Therefore, we calculate D_{AF} for all the vibrational modes for a-Si and na-$Si_{0.45}Ge_{0.55}$ as shown in Figure 2.6(**D**). We observe that, for vibrational modes defined as locons by IPR ($\gtrsim$ 17 THz for a-Si and $\gtrsim$ 10 THz for na-$Si_{0.45}Ge_{0.55}$), the thermal diffusivities decrease significantly. For vibrational modes with frequencies between 10 THz to 17 THz, we observe an order of magnitude decrease in diffusivity from a-Si to na-$Si_{0.45}Ge_{0.55}$, contributing to the decrease in thermal conductivity. For low frequency propagating modes $\lesssim$ 2 THz, no apparent changes in diffusivity occur among different structures, and we are unable to conclude how propagons with frequencies less than 1 THz are affected in the nanocomposite due to limitations in the size of the domain.

The results suggest a simple explanation for the low thermal conductivity of the nanocomposite. In a-Si, nearly the full vibrational spectrum contributes to heat conduction as indicated by the calculated thermal diffusivities and associated small locon population. In the nanocomposite, diffusons with frequencies above the soft Ge cutoff frequency become localized, impeding their ability to transport heat. In effect, the soft inclusion restricts the vibrational spectrum available to conduct heat because many Si vibrational modes are not supported in the inclusion.

Another interesting consideration is why the thermal conductivity of the composite is less than the intrinsic thermal conductivity of the amorphous Ge. The explanation can again be identified from the locon population and the density of vibrational states. The locon population of a-Ge is found to be 8% compared to 31% of na-$Si_{0.45}Ge_{0.55}$, which means there are more vibrational modes that are able to transport heat than in na-$Si_{0.45}Ge_{0.55}$. Although the a-Ge has a lower cutoff frequency than a-Si, its density of states is the same as that of a-Si because the atomic number densities are identical. However, in the nanocomposite, only a fraction of the modes in Si with frequencies below that of the Ge cutoff are able to conduct heat; therefore, the composite contains fewer states with non-negligible thermal diffusivities than a-Ge. As a result, the thermal conductivity of the composite may be lower than those of both the stiff host and softer inclusion.

Many prior works have interpreted thermal conductivity reductions in amorphous or disordered heterogeneous solids using the concept of thermal boundary resistance between the adjacent layers [37, 49, 51]. However, this interpretation relies on the vibrational mode properties of individual constituents separately. Our analysis shows that the vibration mode characters change drastically from a-Si to na-SiGe,

suggesting that thermal boundary resistance is not a well-defined concept in the amorphous nanocomposites studied here as the vibrational modes of the constituent materials cannot be separated. Instead, it is the change in character of the overall vibrational modes of the composite that leads to the low thermal conductivity.

2.4 Conclusion

In this chapter, we studied thermal transport in ultralow thermal conductivity in amorphous nanocomposites and found that mismatching the density of states of the constituent atoms is a promising way to achieve exceptionally low thermal conductivity. Popular normal mode methods such as normal mode lifetimes, Green-Kubo modal analysis, and Allen-Feldman theory to study thermal transport in amorphous solids have been reviewed. These methods explicitly assume that atoms vibrate around their equilibrium positions and that normal modes are the fundamental heat carriers in amorphous solids. However, as we will discuss in Chapter 3, a careful analysis of the predictions from the normal mode methods shows that there exist clear discrepancies with the experiments in some amorphous materials. While the conclusion we obtained from studying amorphous nanocomposites above is not likely to change, the normal mode analysis of vibrations in these materials may need to be revisited.

Chapter 3

NORMAL MODES AND THE VIBRATIONAL EXCITATIONS IN GLASSES

This chapter has been adapted from [69]:

Moon, J., Minnich, A. J., *In preparation*.

Normal mode methods discussed in the previous chapter have been used to study thermal transport in a variety of amorphous solids from polymers [70] and hydrates [71] to amorphous silicon [42–44, 54, 56, 62, 72–77] and others [33, 44, 78–81]. As mentioned previously, normal mode methods rely on the assumptions that atoms vibrate around their equilibrium positions and that normal modes are the fundamental heat carriers. In this chapter, a detailed literature review of normal mode studies in widely studied amorphous a-Si is carried out. Subsequent careful analysis of the results from these studies demonstrates that the assumptions that normal modes are heat carrying excitations leads to direct conflicts with experiments.

3.1 General consensus of thermal transport of a-Si by normal mode methods

Historically, thermal transport in amorphous silicon has been studied extensively as a model amorphous solid due to its relatively simpler monatomic composition and for their wide industrial applications such as solar cells [82, 83] and gravitational wave detectors [84]. It further gained a lot of interests due to their anomalously strong thickness dependence in thermal conductivity measurements that are not typically observed in most amorphous solids [85–89]. Allen and Feldman showed that their thermal conductivity model could not capture the thermal conductivity of a-Si and ascribed this discrepancy to the contribution from the long mean free path, low frequency modes [42]. As mentioned briefly in the last chapter, Allen and Feldman further proposed to categorize the normal modes into three types of "particles": propagons, diffusons, and locons as shown in Fig. 3.1 [43]. Propagons ($\leq\sim$ 2 THz) are propagating modes, similar to phonons in crystals, that can travel over distances larger than $\sim$ interatomic distance. Diffusons ($>\sim$ 2 THz and $\leq\sim$ 17 THz) are modes that are neither propagating, nor localized. Hence, the concepts of mean free paths and wavevector lose meaning. Locons ($>$ 17 THz) are localized modes that

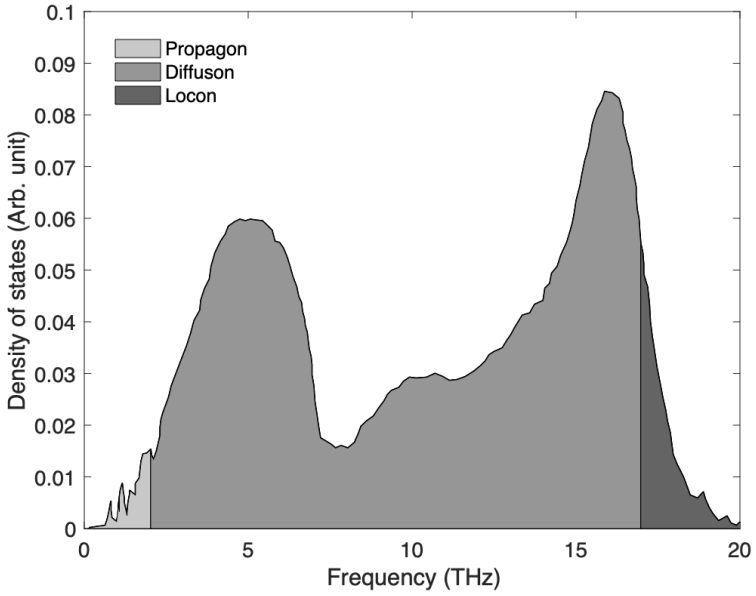

Figure 3.1: Vibrational density of states of amorphous silicon (Stillinger-Weber potential [57], 4096 atoms). Each shaded area represents propagon, diffuson, and locon regions from lighter to darker grey according to Allen and Feldman proposed taxotomy [43].

are thought to contribute negligibly to thermal conductivity. For interested readers, methods to find these crossover frequencies are briefly summarized in Appendix D. This taxonomy of vibrations used in amorphous silicon has also been applied to many different amorphous solids [44, 76, 80].

Each normal mode work has some variations in their conclusions, but the general consensus is that propagons contribute from 20 to 50 % of thermal conductivity despite their small population consisting of only $\sim$ 3 % of the density of states [43, 44, 54, 62, 76], and that they are scattered by anharmonicity [44, 62]. Here, anharmonicity refers to typical phonon-phonon interactions such as normal and Umklapp scattering in absence of disorder scattering [44, 62].

Despite decades of these efforts, however, numerous discrepancies in the general consensus are found when comparing the normal mode results from one work to the other and when directly comparing with experiments as discussed in the next section.

3.2 Discrepancies found in the predictions from normal mode methods

We first examine the general consensus that propagons exist up to 2 to 3 THz. If this assertion is true, we should not observe any size effects in the thermal transport by diffusons that supposedly exist from ~ 2 THz to ~ 17 THz. GKMA was utilized to study the size effect of a-Si by comparing the spectral thermal conductivity of bulk a-Si [54] and a 14 nm thick a-Si film [77] as shown in Fig. 3.2. To clarify, bulk a-Si here denotes the same 4096-atom domain with periodic boundary conditions in all cartesian directions as in Ref. [54] and the 14 nm film has dimensions of 14 nm by 2 nm by 2 nm. In the long direction (cross-plane), the structure is exposed to vacuum, while in the in-plane directions, periodic boundary conditions are imposed. A stark difference in the spectral thermal conductivity of both structures is observed. A suppression of the propagon (< 2 THz) thermal conductivity is observed in the cross-plane direction as expected. What is unexpected here is the clear suppression of diffuson thermal conductivity. By the definition of diffusons by Allen and Feldman [43], they are normal modes with mean free paths below distances on the order of interatomic distances (a few Å). Hence, if the normal modes from 2 THz to 17 THz are indeed diffusons, the diffuson spectral thermal conductivity should not be affected in the cross-plane direction of the 14 nm thick a-Si structure. A clear discrepancy is, therefore, observed here.

We next discuss the prediction that the lifetimes of few THz vibrations are governed by anharmonicity [44, 62]. If that is the case, explaining the low thermal conductivity of a-Si is challenging because the same vibrations contribute 75 $Wm^{-1}K^{-1}$ to thermal conductivity in c-Si. Accounting for the low thermal conductivity of a-Si only by changes in anharmonicity requires either unphysically large increases in anharmonic force constants or in the scattering phase space. These changes would in turn affect other properties like the heat capacity of a-Si that have not been observed [90]. Along similar lines, if lifetimes of few THz vibrations are governed by anharmonicity, the reported thermal conductivities of films of the same thickness should be reasonably uniform, yet the data vary widely [85, 86, 90].

To elucidate the discrepancy further, some of the normal mode lifetimes evaluated at $\Gamma(\boldsymbol{k} = 0)$ in amorphous silicon (a-Si) from several research groups spanning a couple decades [44, 62, 73–75, 91] are illustrated in Fig. 3.3. In this figure, lifetimes from molecular dynamics [44] and from perturbation theory [74, 75] that use Stillinger-Weber potential [57] are adopted. ω^{-2} scaling is plotted as a guide to the eye, which signifies the anharmonic scattering [44, 92]. We see that at 300 K, the

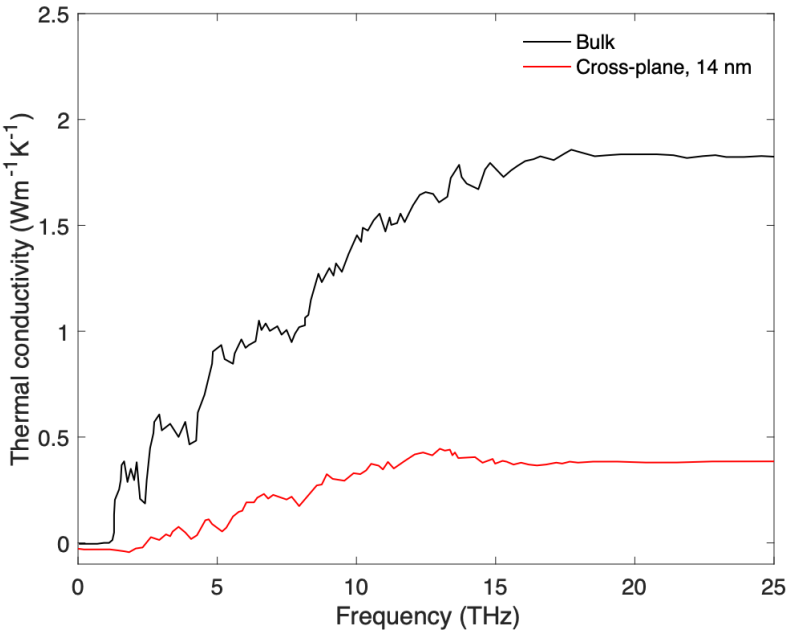

Figure 3.2: Spectral thermal conductivity of bulk a-Si (solid black line) and 14 nm a-Si thin film (solid red line) at 300 K using GKMA [77]. A clear suppression in the thermal conductivity from both propagons and diffusons is seen.

lifetimes derived from both methods coincide well with the exception of a few points at low frequencies due to a smaller structure size of PT method. At 10 K, one to two orders of magnitude increase in the lifetimes for frequencies below around 5 THz is clearly observed, which is consistent with their conclusion that propagating waves are scattered by anharmonicity. This prediction, therefore, indicates that thermal diffusivity and conductivity should necessarily have a significant and continuous increase from 300 K to 10 K. Taking into account the temperature dependent phonon occupation and assuming that the lifetimes increase on average by a factor of 100 in these frequencies, one can estimate that the propagon thermal conductivity increases by a factor of 40 from 300 K to 10 K. However, large increase in thermal conductivity going from room temperature to low temperatures on the order of 10 K is not observed in several experiments [85, 86, 89]. Rather, the opposite trend closely following specific heat temperature dependence is apparent. Our recent thermal diffusivity measurements using transient grating spectroscopy further show that thermal diffusivity is on the same order going from room temperature to 40 K [93].

One may think that the discrepancy in the normal mode lifetime works mentioned

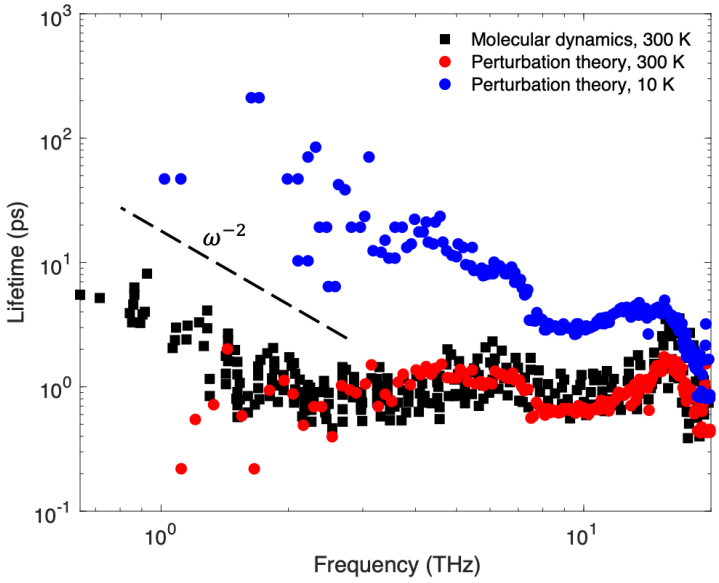

Figure 3.3: Normal mode lifetimes calculated from molecular dynamics at 300 K (black solid square) [44] and perturbation theory at 10 K (blue solid circle) and 300 K (red solid circle) [75]. For all cases, Stillinger-Weber potential [57] was used and WWW continuous random network algorithms were used to construct the structure. At 300 K, molecular dynamics and perturbation theory calculations produce consistent lifetimes and at 10 K, one to two orders of magnitude increase in the lifetimes are observed for modes with frequency less than 5 THz. ω^{-2} is plotted as a guide to the eye, which signifies the anharmonic scattering [44, 92].

above may be the result of using unphysically anharmonic interatomic potentials rather than the normal mode lifetime methodology itself. However, using the same interatomic potentials, we find that thermal conductivity from Green-Kubo formalism follows a typical glass temperature dependent thermal conductivity, which signifies that the high anharmonicity found in the normal mode lifetime does not originate from the interatomic potentials themselves.

We next discuss the predictions that the diffusons dominate thermal conduction in amorphous silicon. To elucidate this prediction, recent normal mode works [54, 77] utilizing Green-Kubo modal analysis that calculates spectral thermal conductivity is reviewed here. In Ref. [54], 4096-atom structure and Tersoff potential [94] were used in the classical molecular dynamics. Due to the decomposition of the thermal conductivity into individual mode contributions, modal quantum correction to the specific heat is possible and both the classical and the quantum corrected results at 300 K are shown in Fig. 3.4 (A). We see an apparent effect of the quantum correction

in the spectral thermal conductivity at high frequencies above 8 THz. Due to the small size of the computational domain, no contribution from long wavelength, long period vibrations (< 1.2 THz) is observed. Setting 2 THz as the propagon to diffuson crossover using the eigenvector periodicity method, about 20 % of the thermal conductivity is found to be from propagons [76].

Temperature dependent thermal conductivity from the quantum corrected GKMA predictions and experiments are displayed in Fig. 3.4 (B). In the original paper [54], only the 3ω measurements [85] of the 0.52 μm thick, sputtered sample was compared with the predictions. Despite the lack of vibrations < 1.2 THz in the calculation, an excellent agreement is clearly seen. On the other hand, when comparing with another 3ω measurements [86] of 80 μm thick sample made from hot-wire chemical vapor deposition (HWCVD), we see a large discrepancy, which signifies the dominant contribution to thermal conductivity by long mean free path propagons.

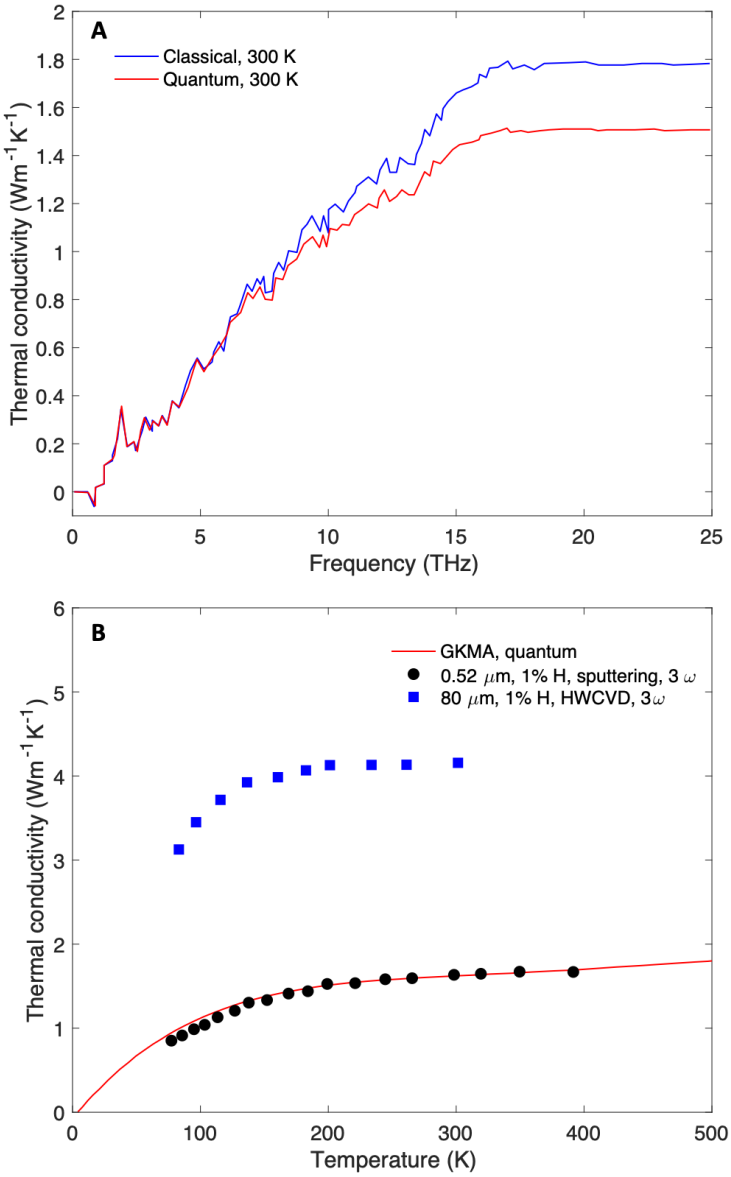

Figure 3.4: **(A)** Spectral thermal conductivity of a-Si at 300 K using GKMA with (solid red line) and without (solid blue line) the quantum correction to the specific heat [54]. Tersoff potential [94] and 4096 atoms are used in the calculations. A clear effect of the quantum correction is shown for vibrations with frequencies higher than 8 THz. **(B)** Temperature dependent thermal conductivity comparisons between quantum corrected GKMA (solid red line) [54] and thermal conductivity measurements of 0.52 μm thick a-Si film (solid black circle) synthesized by sputtering [85] and 80 μm thick a-Si film (solid blue square) synthesized by hot-wire chemical vapor deposition (HWCVD) [86] using the 3ω technique. Both films are reported to have a very small amount of hydrogen atoms (1%) While an excellent agreement is observed between the simulation and the 0.52 μm sample, a large discrepancy is shown for the 80 μm measurements, which signifies the role of propagons.

3.3 Testing the normal mode assumption that atoms move around equilibrium positions in glasses

Here, we examine the fundamental assumption of normal mode analysis that atoms vibrate around their equilibrium positions.

Two types of amorphous silicon simulation domains were prepared. The first structure (4096 atoms) was created using the Stillinger Weber potential [57] and the timestep of 0.5 fs in classical molecular dynamics (LAMMPS [61]). The crystalline structure was first melted at 3500 K for 500 ps in an NVT ensemble. Next, the liquid silicon was quenched to 1000 K with the quench rate of 100 K/ps. The structures were annealed at 1000 K for 25 ns to reduce metastabilities. Finally, the domain was quenched at a rate of 100 K/ps to desired temperatures (300 K, 500 K, 700 K, and 900 K) and equilibrated at these temperatures for 10 ns in an NPT ensemble using a Nose-Hoover thermostat. The atomic locations were then collected for the next 150 ps. Another structure (216 atoms) was also created by *ab-initio* molecular dynamics (AIMD). AIMD simulations were performed with the projector augmented wave approach [95] and the Perdew-Burke-Ernzerhof (PBE) [96] generalized-gradient approximation to the density functional theory (DFT) as implemented in the Vienna ab-initio simulation package (VASP) [97]. The time step was the same as classical MD. Only Γ was adopted for the wavevector grid and the energy cutoff of 245 eV was used. Crystalline silicon (c-Si) was first melted at 3500 K for 30 ps followed by quenching to desired temperatures at 100 K/ps. The structure relaxed for 10 ps. Then, the atomic locations were recorded for the next 25 ps at the desired temperatures. The radial distribution function of these two structures compared to neutron diffraction measurements on a-Si [98] is shown in Fig. 3.5. Generally, good agreement between the computational structures and the experiment is observed, but a better match is demonstrated for the MD structure, especially at the second peak.

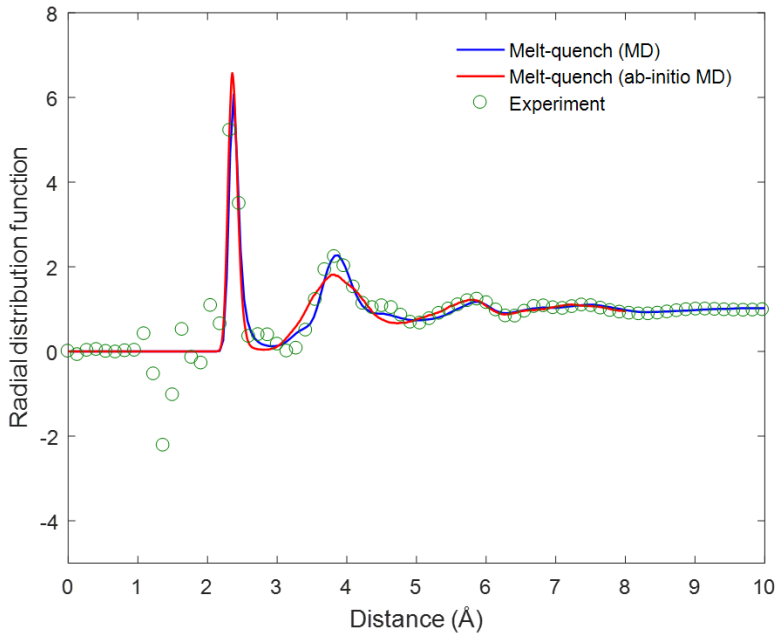

Figure 3.5: Radial distribution function of two a-Si structures made from MD and *ab-initio* MD is compared to neutron diffraction of a-Si [98].

The maximum distances away from the initial positions for each atom during the 500 ps data collection for both c-Si and a-Si in classical MD are plotted in Fig. 3.6. It is clear that at all temperatures, atoms in a-Si explore significantly more volume compared to those in c-Si during the simulation. While having more volume to move around does not necessarily mean that atoms are diffusing, some atoms move as much as 1.4 Å, 2.1 Å, and 3.9 Å which is comparable to the interatomic distance (~ 2.4 Å) of a-Si at 300 K, 500 K, and 900 K, respectively. For simplicity, the maximum atomic distances from *ab-initio* MD are not plotted. It is worth mentioning, however, that they had closely overlapping results with classical MD. To gain further insight into atomic displacements, temporal movement of an atom at 300 K having maximum distance of 0.7 to 0.8 Å away from the initial position in Fig. 3.6 **A** is shown in Fig. 3.7. Also plotted is the results from *ab-initio* MD. We can clearly see that in both cases, atoms initially vibrate around their equilibrium positions. Some time later, however, these atoms hop to new equilibrium positions and vibrate around these positions. When examining the temporal movements of atoms in a-Si at higher temperatures, more atoms were found to hop and diffuse to new equilibrium positions due to their higher kinetic energy as expected. For c-Si, atoms had greater distance amplitude at higher temperatures, but they still vibrated

around their equilibrium positions during the entire simulations.

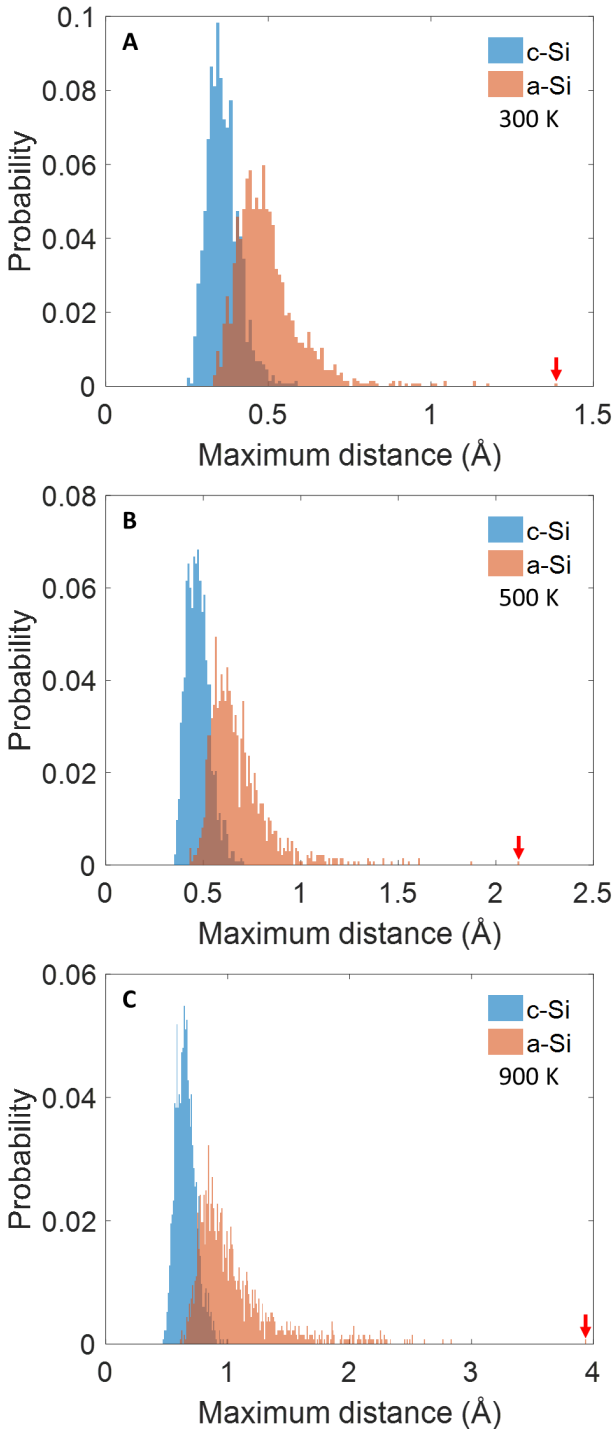

Figure 3.6: Histogram of maximum distance from initial position of each atom for both c-Si and a-Si from classical MD at (**A**) 300 K, (**B**) 500 K, and (**C**) 900 K. Red arrows denote the maximum value to which the distribution is extended to. We see that atoms in a-Si have consistently larger displacements than those in c-Si.

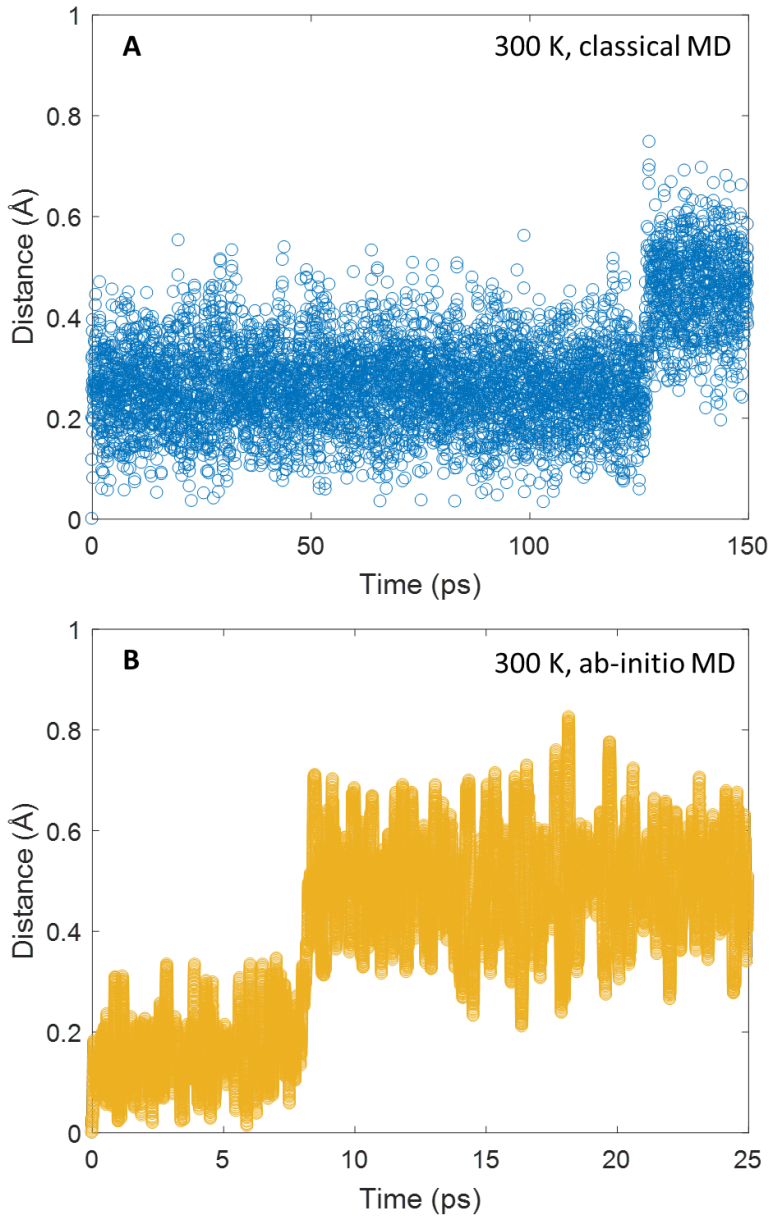

Figure 3.7: Temporal movement of an atom at 300 K for (**A**) classical MD and (**B**) ab-initio MD. These atoms have maximum distance of 0.7 to 0.8 Å shown in Fig. 3.6 (**A**). Clear atomic hopping is observed in both cases.

Similar results were also experimentally observed recently in neutron reflectometry in ^{29}Si/^{nat}Si isotope multilayers [99, 100]. Isotope multilayers are stacks of 10 layers of [^{29}Si (5 nm) /^{nat}Si (16 nm)] deposited by ion-beam sputtering. In the neutron reflectometry, Bragg peaks are formed by the reflection of the neutrons at the isotope interfaces. Changes in the Bragg peak intensities at various temperatures compared to that of the as-deposited sample intensity leads to the self-diffusion measurements. This apparatus is sensitive to low diffusivities down to 10^{-25} m^2/s and very small diffusion lengths of 1 nm and below. Several temperature dependent diffusivity measurements under argon at ambient pressure during various time periods were done. The diffusivity measurements after 60 seconds of annealing at 673 K, 723 K, and 773 K are depicted in Fig. 3.8 [100]. Diffusion lengths, $d = (2Dt)^{1/2}$, are also represented on top of each data point. As the diffusivity is an ensemble averaged measurement, the distribution of the diffusion lengths for each atom is unknown, but it is apparent that on average atomic diffusion is quite significant in a-Si at these temperatures.

Quantitative comparison between experiments [100] and our computations is difficult due to the large differences in simulation times (on the order of ps to ns) compared to experiments (minutes to hours). Nonetheless, it is evident from both experiments and calculations that the fundamental assumption in normal mode analysis that atoms vibrate around their equilibrium positions may be unsatisfied. As normal mode decomposition methods are routinely used for amorphous solids at high temperatures up to 1200 K [79, 91], caution is needed to interpret the results from these methods.

3.4 Conclusion

Amorphous silicon has been a model glass to study thermal transport in glasses due to its relatively simpler monatomic composition and industrial applications. In this chapter, decades of research efforts utilizing normal mode methods in a-Si have been reviewed and the general consensus from these works has been discussed. A careful analysis of various works, however, clearly shows that there exist numerous discrepancies in the consensus, from results invalidating assumptions made in these methods to explicit inconsistencies when comparing to the measurements. Pinpointing the exact origin of these discrepancies is challenging, but the common aspects that these methods share are the assumptions that i) atoms vibrate around their equilibrium positions and that ii) normal modes are the fundamental heat carriers in amorphous solids. We show through calculations that some atoms are prone

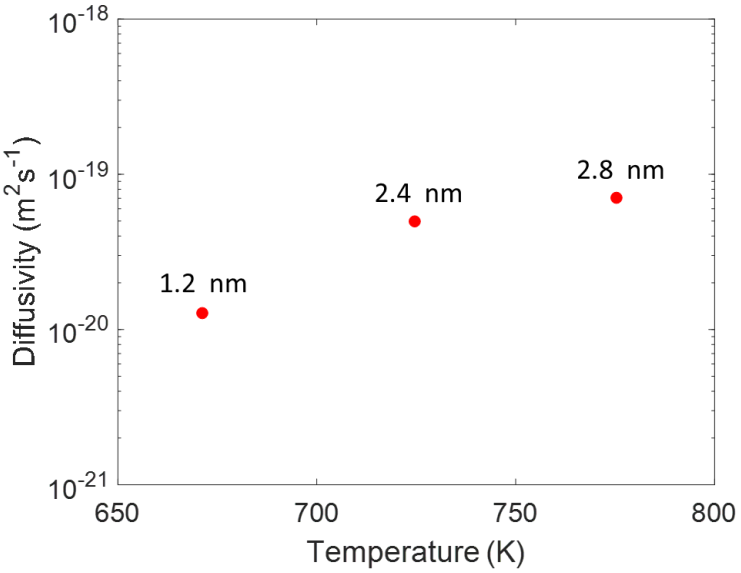

Figure 3.8: Atomic diffusivity in a-Si after 60 seconds of annealing at 673 K, 723 K, and 773 K [100]. Numbers above each data point represent diffusion lengths at that temperature.

to diffusion even at room temperature, contrasting the first assumption of normal modes mentioned above. It may be the case that at sufficiently low temperatures or for some special atomic configurations, atoms do not have enough kinetic energy to overcome their local potential well and they do vibrate around their equilibrium positions. However, *are normal modes good representations of atomic dynamics in the amorphous solid in general?* It is important to note that the degree of error that the atomic diffusion brings to the normal mode analysis is unexplored, but an alternative scheme of studying atomic dynamics that does not rely on normal modes or assumptions of equilibrium positions is highly needed. Historically, atomic dynamics in amorphous solids was investigated using the ideas and concepts that were applied to crystals and recently, a unified theory of thermal transport of crystals and glasses was published [101]. However, perhaps amorphous solids should instead be treated as highly viscous liquid when studying their atomic dynamics and thermal transport.

In the next chapter, we use inelastic scattering theory to study the vibrational excitations of glasses which does not assume that the excitations are normal modes.

Chapter 4

INELASTIC X-RAY SCATTERING TO PROBE COLLECTIVE EXCITATIONS IN AMORPHOUS SOLIDS

In this chapter, inelastic scattering through light-matter interactions to probe directly collective excitations without the assumptions of normal modes is reviewed thoroughly. Due to the lack of kinematic constraints and with the development of high brilliance X-ray sources and high quality optics, inelastic X-ray scattering has been extensively used to probe several aspects of materials dynamics as shown in Fig. 4.1. Methods range from quasi-elastic scattering which probes diffusive motion to compton scattering that probes electron momentum densities. In this chapter, we explicitly focus on non-resonant inelastic X-ray scattering (IXS) which is relevant to atomic dynamics. Many different forms of condensed matter have been studied from crystals [102, 103] and glasses [104–109] to liquids [109–111] via IXS, but the focus of this chapter lies in glasses.

The rest of this chapter is structured as follows. First, the theory of inelastic

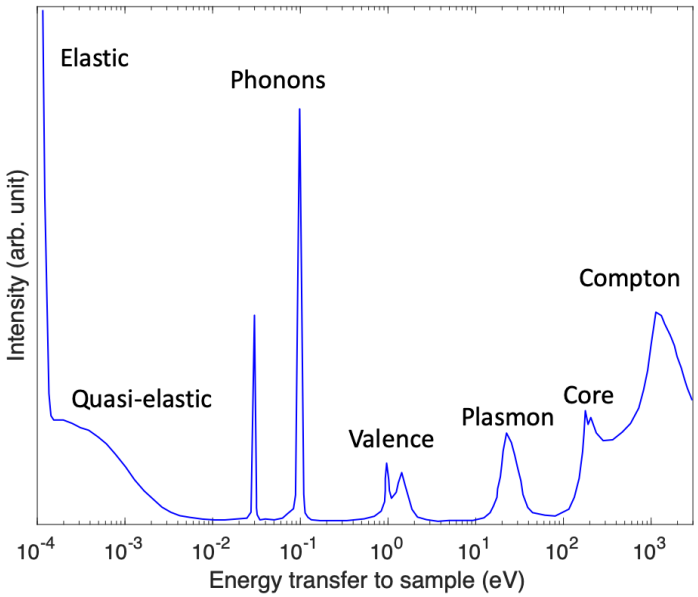

Figure 4.1: Schematic of excitations that can be probed by inelastic X-ray scattering [112].

scattering is derived and the concept of dynamic structure factor is discussed. Then, the results from IXS on atomic dynamics in some extensively investigated glasses, such as amorphous silica and glycerol, are discussed. For interested readers, in-depth reviews in Ref. [113–117] are recommended. Knowledge of instrumentation is certainly crucial for successful measurements. However, the goal of this chapter is rather to introduce the background of IXS and the new physical insights on atomic dynamics in amorphous solids gained from IXS. For more information on instrumentation, Refs. [114, 117–119] are recommended.

4.1 Theory of non-resonant inelastic X-ray scattering

The Hamiltonian for a system of non-relativistic electrons in a condensed matter interacting with an electromagnetic field is expressed by

$$H = \frac{1}{2m}\sum_i \left(\boldsymbol{p}_i - \frac{q}{c}\boldsymbol{A}\delta(\boldsymbol{r}-\boldsymbol{r}_i)\right)^2 + \sum_i V(\boldsymbol{r}_i) + V_{int}^{e-e} \tag{4.1}$$

where c is the speed of light, q is the electric charge, m is the electron mass, sum is over all electrons, $V(\boldsymbol{r}_i)$ is the atom-electron potential, and V_{int}^{e-e} describes the electron-electron interaction. Spin contribution is neglected. Rearranging the Hamiltonian,

$$H = H_e + H_{int}^{(1)} + H_{int}^{(2)} \tag{4.2}$$

where

$$H_e = \sum_i \left[\frac{\boldsymbol{p}_i^2}{2m} + V(\boldsymbol{r}_i)\right] + V_{int}^{e-e} \tag{4.3}$$

$$H_{int}^{(1)} = -\frac{q}{2mc}\sum_i [\boldsymbol{p}_i \cdot \boldsymbol{A}\delta(\boldsymbol{r}-\boldsymbol{r}_i) + \boldsymbol{A}\delta(\boldsymbol{r}-\boldsymbol{r}_i)\cdot\boldsymbol{p}_i] \tag{4.4}$$

$$H_{int}^{(2)} = \frac{q^2}{2mc^2}\sum_i \boldsymbol{A}\cdot\boldsymbol{A}\delta(\boldsymbol{r}-\boldsymbol{r}_i) \tag{4.5}$$

$$\boldsymbol{A} = \sum_{\boldsymbol{k},\alpha} 2\pi\sqrt{\frac{\hbar}{\omega_k L^3}}c\epsilon_\alpha\left[a_{\boldsymbol{k},\epsilon}^{+}e^{i\boldsymbol{k}\cdot\boldsymbol{r}} + a_{\boldsymbol{k},\epsilon}^{-}e^{-i\boldsymbol{k}\cdot\boldsymbol{r}}\right]. \tag{4.6}$$

Here $\boldsymbol{k}$ and α refer to the photon wave vector and polarization state, respectively. L^3 is the normalization box volume, $\omega_{\boldsymbol{k}}$ is the photon angular frequency, $a_{\boldsymbol{k},\epsilon}^{+}$ is the photon annhilation operator and $a_{\boldsymbol{k},\epsilon}^{-}$ is the photon creation operator for the photon state $|\boldsymbol{k},\alpha\rangle$. We can see that to the first order, $H_{int}^{(1)}$ is related to one photon emission or absorption. To the second order, we have scattering. On the other hand, we have scattering from the first order of $H_{int}^{(2)}$ due to its quadratic vector potential. When considering only the first order theory, we can, therefore, neglect $H_{int}^{(1)}$. If, however,

the incident photon energy is near an X-ray resonance, scattering from $H_{int}^{(1)}$ can become significant. In the rest of the derivation of the double differential IXS cross section, we only consider up to the first order: the scattering of photons only comes from $H_{int}^{(2)}$. We explicitly assume adiabatic approximation and the electronic part of the total wave function unaffected by the scattering process.

Recall that the density of states of a single photon with polarization α and $\boldsymbol{k}$ pointing into the solid angle $d\Omega$ is given by

$$g(\boldsymbol{k}, \alpha) = \frac{k^2 L^3}{(2\pi)^3} \frac{d\Omega}{\hbar c} \tag{4.7}$$

and that the incident photon flux $\Phi = \frac{c}{L^3}$. Now, consider a situation in which a photon $|\boldsymbol{k}, \alpha\rangle$ is scattered by a state $|\lambda\rangle$ in the sample via $H_{int}^{(2)}$ to create a photon $|\boldsymbol{k'}, \beta\rangle$ and a sample state $|\lambda'\rangle$ as shown in Fig. 4.2. Hence, the initial state prior to the scattering is denoted as $|\boldsymbol{k}, \alpha, \lambda\rangle$ and the final state after the scattering is denoted as $|\boldsymbol{k'}, \beta, \lambda'\rangle$.

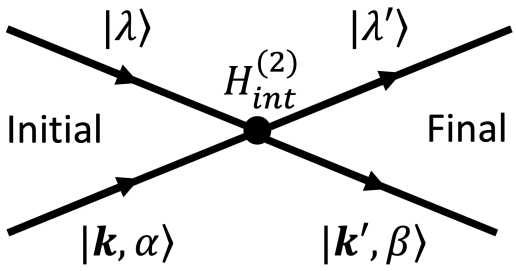

Figure 4.2: Scattering a photon $|\boldsymbol{k}, \alpha\rangle$ by a state $|\lambda\rangle$ in the sample through the Hamiltonian, $H_{int}^{(2)}$, which creates a photon $|\boldsymbol{k'}, \beta\rangle$ and a new state $|\lambda'\rangle$ in the sample.

The differential cross section of this process into a solid angle $d\Omega$ is written as

$$\left(\frac{d\sigma}{d\Omega}\right) = \frac{1}{\Phi} \frac{1}{d\Omega} \sum_{\boldsymbol{k'}}^{d\Omega} W_{|\boldsymbol{k},\alpha,\lambda\rangle \to |\boldsymbol{k'},\beta,\lambda'\rangle} \tag{4.8}$$

where the number of transitions per unit time, $W_{|\boldsymbol{k},\alpha,\lambda\rangle \to |\boldsymbol{k'},\beta,\lambda'\rangle}$ is expressed using the Fermi's golden rule as

$$\sum_{\boldsymbol{k'}}^{d\Omega} W_{|\boldsymbol{k},\alpha,\lambda\rangle \to |\boldsymbol{k'},\beta,\lambda'\rangle} = \frac{2\pi}{\hbar} |\langle \boldsymbol{k'}, \beta, \lambda' | H_{int}^{(2)} | \boldsymbol{k}, \alpha, \lambda \rangle|^2 g(\boldsymbol{k'}, \beta). \tag{4.9}$$

The bra-ket square term above can be simplified as

$$|\langle \boldsymbol{k'}, \beta, \lambda' | H_{int}^{(2)} | \boldsymbol{k}, \alpha, \lambda \rangle|^2 = \frac{q^4 \hbar^2 \pi^2}{m^2 L^6} \frac{|\epsilon_{\boldsymbol{k'}} \cdot \epsilon_{\boldsymbol{k'}}|^2}{\omega_{\boldsymbol{k'}} \omega_{\boldsymbol{k}}} \langle \lambda' | \sum_i e^{-i\boldsymbol{Q}\cdot\boldsymbol{r}_i} | \lambda \rangle \langle \lambda | \sum_j e^{i\boldsymbol{Q}\cdot\boldsymbol{r}_j} | \lambda' \rangle \tag{4.10}$$

where the momentum transfer $\boldsymbol{Q} = \boldsymbol{k'} - \boldsymbol{k}$. To obtain the above equation, only the term involving $a^-_{\boldsymbol{k'},\beta} a^+_{\boldsymbol{k},\alpha}$ in the $H^{(2)}_{int}$ was considered as it annihilates the photon $|\boldsymbol{k}, \alpha\rangle$ and creates a photon in the $|\boldsymbol{k'}, \beta\rangle$ state. Plugging in the expression for the flux and the photon density of states mentioned earlier, the differential cross section can be written as

$$\left(\frac{d\sigma}{d\Omega}\right) = r_o^2 \left(\frac{\boldsymbol{k'}}{\boldsymbol{k}}\right) |\epsilon_{\boldsymbol{k'}} \cdot \epsilon_{\boldsymbol{k}}|^2 \langle \lambda' | \sum_i e^{-i\boldsymbol{Q}\cdot\boldsymbol{r}_i} |\lambda\rangle\langle\lambda| \sum_j e^{i\boldsymbol{Q}\cdot\boldsymbol{r}_j} |\lambda'\rangle \tag{4.11}$$

where $r_o = \frac{q^2}{mc^2}$ is the classical electron radius. Finally, requiring the energy conservation and thermally averaging over all initial and final states λ, λ' we have the double differential cross section

$$\frac{d^2\sigma}{d\Omega dE'} = r_o^2 \frac{\boldsymbol{k'}}{\boldsymbol{k}} |\epsilon_{\boldsymbol{k'}} \cdot \epsilon_{\boldsymbol{k}}|^2 \sum_{\lambda\lambda'} \sum_{i,j} p_\lambda \langle \lambda' | e^{-i\boldsymbol{Q}\cdot\boldsymbol{r}_i} |\lambda\rangle\langle\lambda| e^{i\boldsymbol{Q}\cdot\boldsymbol{r}_j} |\lambda'\rangle \delta(\hbar\omega + E - E') \tag{4.12}$$

where $p_\lambda = \frac{e^{-E_\lambda/k_B T}}{Z}$ and Z is the partition function, $\hbar\omega = E' - E$ is the energy transferred from the photon to the sample. Assuming the adiabatic approximation, the atomic quantum state $|S\rangle = |S_e\rangle|S_n\rangle$ where the subscript e and n denote the electronic and nuclear states, respectively. When the exchanged energies by scattering is small (1 to $\sim$ 100 meV) compared to that of the electronic excitation energies, the contributions of core electrons to the total scattering is dominant. Therefore, the exchange of momentum and energy is mostly due to the excitations of the ions. With these hypotheses, the double differential cross section can be written as

$$\frac{d^2\sigma}{d\Omega dE'} = r_o^2 \frac{\boldsymbol{k'}}{\boldsymbol{k}} |\epsilon_{\boldsymbol{k'}} \cdot \epsilon_{\boldsymbol{k}}|^2 \sum_{\lambda\lambda'} \sum_{i,j} p_\lambda \langle \lambda' | f_i(\boldsymbol{Q}) e^{-i\boldsymbol{Q}\cdot\boldsymbol{R}_i} |\lambda\rangle\langle\lambda| f_j(\boldsymbol{Q}) e^{i\boldsymbol{Q}\cdot\boldsymbol{R}_j} |\lambda'\rangle \delta(\hbar\omega + E - E') \tag{4.13}$$

where $f_i(Q)$ is the atomic form factor of the ith atom, $\boldsymbol{R}_i$ is the atom position vector, and the sample states, λ, λ' refer to the nuclear states. Assuming that all atoms scatter identically (same form factor), we can take out the atomic form factors and simplify as

$$\frac{d^2\sigma}{d\Omega dE'} = r_o^2 \frac{\boldsymbol{k'}}{\boldsymbol{k}} |\epsilon_{\boldsymbol{k'}} \cdot \epsilon_{\boldsymbol{k}}|^2 |f(\boldsymbol{Q})|^2 S(\boldsymbol{Q}, \omega) \tag{4.14}$$

where the dynamic structure factor, $S(\boldsymbol{Q}, \omega)$ is defined as

$$S(\boldsymbol{Q}, \omega) = \sum_{\lambda\lambda'} \sum_{i,j} p_\lambda \langle \lambda' | e^{-i\boldsymbol{Q}\cdot\boldsymbol{R}_i} |\lambda\rangle\langle\lambda| e^{i\boldsymbol{Q}\cdot\boldsymbol{R}_j} |\lambda'\rangle \delta(\hbar\omega + E - E'). \tag{4.15}$$

By interpreting the operators in the Heisenberg picture and writing the delta function in integral representation, the dynamic structure factor can be written in a compact

form as

$$S(\boldsymbol{Q},\omega) = \frac{1}{2\pi}\int_{-\infty}^{\infty} dt e^{-i\omega t}\langle\rho^{\dagger}(\boldsymbol{Q},t)\rho(\boldsymbol{Q},0)\rangle \tag{4.16}$$

where the $\rho(\boldsymbol{Q},t)$ is the spatial Fourier transform of the density operator $\rho(\boldsymbol{R},t)$ as

$$\rho(\boldsymbol{Q},t) = \sum_i e^{-i\boldsymbol{Q}\cdot\boldsymbol{R}_i} = \int d\boldsymbol{R} e^{-i\boldsymbol{Q}\cdot\boldsymbol{R}} \sum_i \delta(\boldsymbol{R}-\boldsymbol{R}_i) = \int d\boldsymbol{R} e^{-i\boldsymbol{Q}\cdot\boldsymbol{R}}\rho(\boldsymbol{R},t). \tag{4.17}$$

Hence, the dynamic structure factor is the temporal Fourier transform of the correlation of the spatial Fourier component of the density operators. In deriving the dynamic structure factor, it is important to note that no assumption of the normal modes has been made. When the form factors of atoms are different in Eq. (4.13) (for instance, in non-monatomic systems), the double differential cross section can be expressed in terms of the fluctuations and the mean of the atomic form factor [114].

The measured scattered intensity is then proportional to the double differential cross section as [114]

$$I = KI_o\frac{\partial^2\sigma}{\partial\Omega\partial E'}\Delta\Omega\Delta E' nt e^{-\mu t} \tag{4.18}$$

where K accounts for detector efficiency and all other geometrical and spurious intensity effects, I_o is the incident beam intensity, n is the number of scatterers per unit volume, t is the sample thickness, μ is the total absorption coefficient. Since $\frac{\partial I}{\partial t} = 0$ when $t = \frac{1}{\mu}$, it is ideal to have the sample thickness equal to the absorption depth of a given X-ray beam.

Another way to calculate the dynamic structure factor is using the velocity currents as demonstrated below.

$$\begin{aligned}
\omega^2 S(\boldsymbol{Q},\omega) &= \frac{\omega^2}{2\pi}\int_{-\infty}^{\infty} e^{-i\omega t}\langle\rho^{*}(\boldsymbol{Q},t)\rho(\boldsymbol{Q},0)\rangle \\
&= \frac{i^2}{2\pi}\int_{-\infty}^{\infty}\frac{d^2e^{-i\omega t}}{dt^2}\langle\rho^{*}(\boldsymbol{Q},t)\rho(\boldsymbol{Q},0)\rangle \\
&= -\frac{1}{2\pi}\int_{-\infty}^{\infty} dt e^{-i\omega t}\left\langle\left[\frac{\partial^2\rho^{*}(\boldsymbol{Q},t)}{\partial t^2}\right]\rho(\boldsymbol{Q},0)\right\rangle \\
&= \frac{1}{2\pi}\int_{-\infty}^{\infty} dt e^{-i\omega t}\left\langle\left[\frac{\partial\rho^{*}(\boldsymbol{Q},t)}{\partial t}\right]\left[\frac{\partial\rho(\boldsymbol{Q},t)}{\partial t}\right]_{t=0}\right\rangle
\end{aligned} \tag{4.19}$$

.

To get to the third equation, integration by parts was used twice with the correlation function going to zero at the boundaries. The last step is from an identity for the

Liouville operator being a Hermitian first-order differential operator [120]. Here the time derivative of the density operator is given by

$$\frac{\partial \rho(\boldsymbol{Q},t)}{\partial t} = -i \sum_i (\boldsymbol{Q} \cdot \boldsymbol{v}_i) e^{-i\boldsymbol{Q}\cdot\boldsymbol{R}_i} \tag{4.20}$$

where $\boldsymbol{v}_i$ is the velocity of the atom i. The dynamic structure factor is then expressed as

$$S(\boldsymbol{Q},\omega) = \frac{1}{2\pi}\left(\frac{Q}{\omega}\right)^2 \int_{-\infty}^{\infty} dt \langle \boldsymbol{j}_L(\boldsymbol{Q},t) \cdot \boldsymbol{j}_L^*(\boldsymbol{Q},0)\rangle e^{-i\omega t} \tag{4.21}$$

where the longitudinal velocity current is given by

$$\boldsymbol{j}_L(\boldsymbol{Q},t) = \sum_i^N [\boldsymbol{v}_i(t) \cdot \hat{\boldsymbol{Q}}]\hat{\boldsymbol{Q}} e^{i\boldsymbol{Q}\cdot\boldsymbol{R}_i(t)} \tag{4.22}$$

where $\hat{\boldsymbol{Q}}$ denotes $\boldsymbol{Q}$ unit vector.

Using molecular dynamics, time dependent atom locations and velocities can be recorded. With either Eq. (4.16) or Eq. (4.21), the dynamic structure factor can be readily calculated and compared directly to the inelastic scattering experiments. It is worth mentioning that sometimes in literature, dynamic structure factor is calculated without the factor in front of the integral in Eq. (4.21). It is again emphasized here that no assumption of the normal modes is used in the dynamic structure factor derivations.

4.2 Meaning of dynamic structure factor

Now, what does the dynamic structure factor tell us about the atomic dynamics in amorphous solids? To answer this question, we look at the relationship between the dynamic structure factor and retarded Green's function via the fluctuation-dissipation theorem given by

$$S(\boldsymbol{Q},\omega) = -\frac{1}{\pi}(n_{BE}+1) Im(G^R(\boldsymbol{Q},\omega)) \tag{4.23}$$

where n_{BE} is the Bose-Einstein distribution and $G^R(\boldsymbol{Q},\omega)$ is the retarded Green's function in frequency and wavevector space. The retarded Green's function of an interacting system can in principle be obtained in a many-body perturbation approach using Feynman diagrams [121–123]. The real part of the pole of $G^R(\boldsymbol{Q},\omega)$ gives the excitation energy and the imaginary part of the pole of $G^R(\boldsymbol{Q},\omega)$ represents the lifetime of the excitation. In the dynamic structure factor, these translate to the peak frequency of the inelastic peaks being the collective excitation energy with the finite

broadening proportional to the inverse lifetime of collective excitations. Here, it is emphasized that inelastic scattering can, therefore, probe collective excitations of matter without the assumptions of normal modes.

A typical IXS spectrum of a glass is shown in Fig. 4.3. This measurement was done for glassy glycerol at 175 K at the momentum transfer $Q = 2$ nm^{-1} [109]. We see a large quasi-elastic peak at zero energy representing no energy transfer to the sample followed by two asymmetric inelastic peaks on the sides representing collective excitations in the sample with ± 4.2 meV energy and linewidths (~2 meV) representing inverse of lifetimes at the momentum transfer of $Q = 2$ nm^{-1}. The asymmetry of the inelastic peaks arise according to the detailed-balance principle. To extract useful information, a Lorentzian and two damped harmonic oscillator (DHO) models were convolved with the experimentally determined resolution function to fit the quasi-elastic peak and inelastic peaks, respectively as clearly seen in Fig. 4.3 (**B**).

With some fundamentals of inelastic scattering gone over, we now move onto new physical insights gained from IXS on widely studied amorphous solids, such as amorphous silica and glycerol.

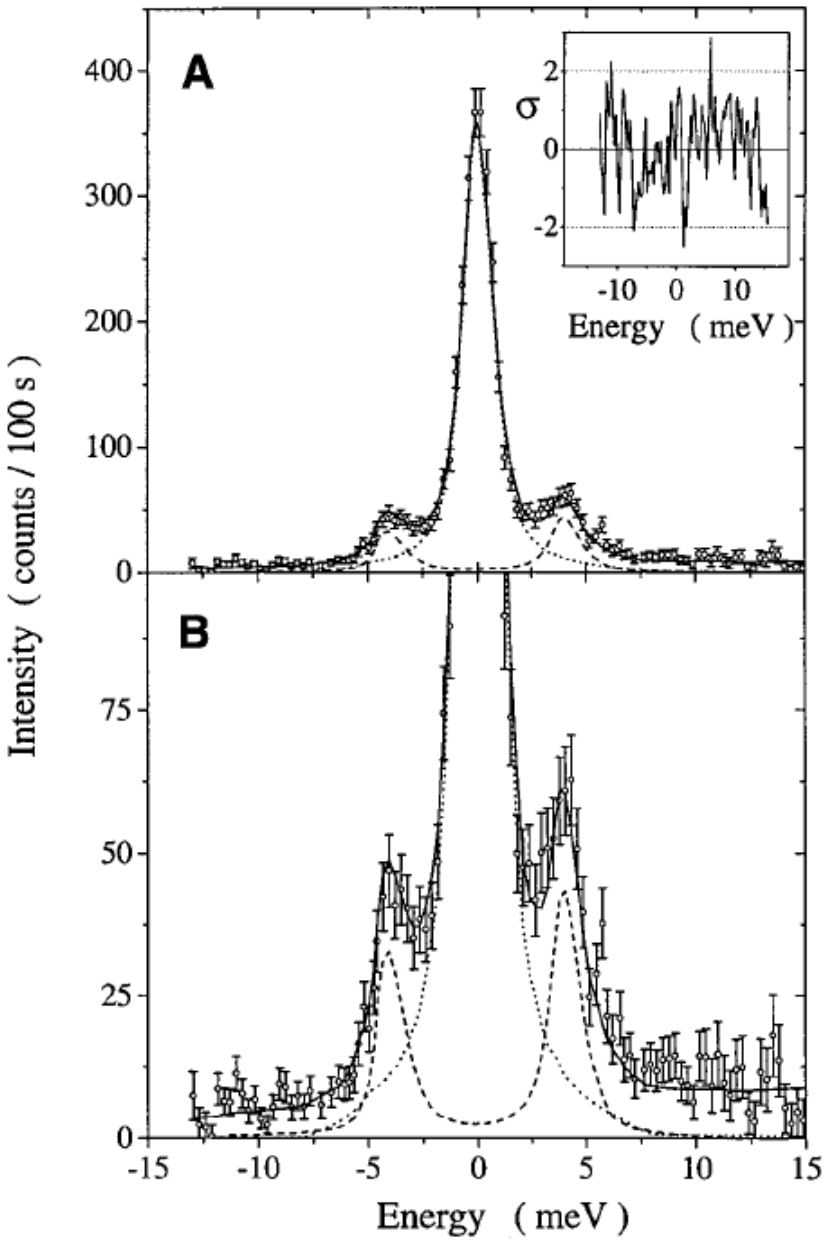

Figure 4.3: (**A**) IXS spectrum of glassy glycerol at 175 K and Q = 2 nm^{-1} [109]. The dotted line and dashed lines show quasi-elastic and inelastic contributions, respectively. Inelastic peaks represent the collective excitations with excitation energy of ± 4.2 meV with linewidths being the inverse lifetimes at this momentum transfer. The quasi-elastic peak was fitted with a Lorentzian and the inelastic peaks were fitted with a damped harmonic oscillator (DHO) model. Solid line is the superposed fit. (**B**) Enlarged view of the inelastic spectra. The inset in (**A**) shows the residuals of the fit to the data in standard deviation units, σ.

4.3 Overview of IXS measurements on glassess

Amorphous silica

A representative momentum transfer dependent IXS spectra of amorphous silica is shown in Fig. 4.4 [109]. The solid line represents the resolution function in Fig. 4.4 (**A**) and IXS spectra with the resolution function subtracted show clear inelastic signal in Fig. 4.4 (**B**). We can see that as the momentum transfer doubles, the peak frequencies of the inelastic peaks also double, demonstrating that these are propagating excitations dispersing with a linear relation as indicated by arrows in Fig. 4.4 (**B**).

It is worth mentioning here that due to the instrument energy resolution of $\sim$ 1 to 2 meV, which is still remarkable considering that the hard X-rays used in IXS typically have energies of 10 to 20 keV, Q = 1 nm^{-1} is close to the lower bound that IXS can probe. For lower Q's, Brillouin light scattering and inelastic ultraviolet scattering can be used.

Peak frequencies and the broadening of the temperature dependent inelastic excitations are demonstrated in Fig. 4.5. It can be seen that the peak frequencies are not affected by the temperature as they are within the error bars with each other. Similar observation is shown for the broadening where a clear temperature dependence is not observed as shown in Fig. 4.5 (**B**); therefore, the role of structural disorder is dominant in sound attenuation in these frequency and wavevector regimes. By comparing the lifetimes which are inversely proportional to the broadening and the peak frequency, the Ioffe-Regel crossover has been determined to be around 1 to 2 THz in a-SiO_2. Another point to take away from Fig. 4.5 (**B**) is the apparent power law $\Gamma \, \alpha \, Q^2$ which has also been observed "universally" in these high momentum transfer regimes in many types of glasses [125–128]. However, the precise origin of this power law is still unclear.

Brillouin light scattering (BLS) and inelastic ultraviolet scattering (IUVS) measurements were also done on a-SiO_2 to investigate the attenuation of the acoustic excitations at lower momentum transfers as shown in Fig. 4.6 [105, 129]. The Q^2 scaling from the IXS data shown in Fig. 4.5 is also shown for comparisons. While we also observe a Q^2 dependence for acoustic excitations with $Q \leq 0.1$ nm^{-1}, there is a clear discontinuity between the two. At the higher Q values above 0.1 nm^{-1}, we see an intermediate strong scattering regime with Q^4 dependence which seems to connect the two Q^2 lines. The frequencies at which the transitions ($Q^2 \rightarrow Q^4$ and $Q^4 \rightarrow Q^2$) occur are reported at 100 GHz and 140 GHz, respectively [105].

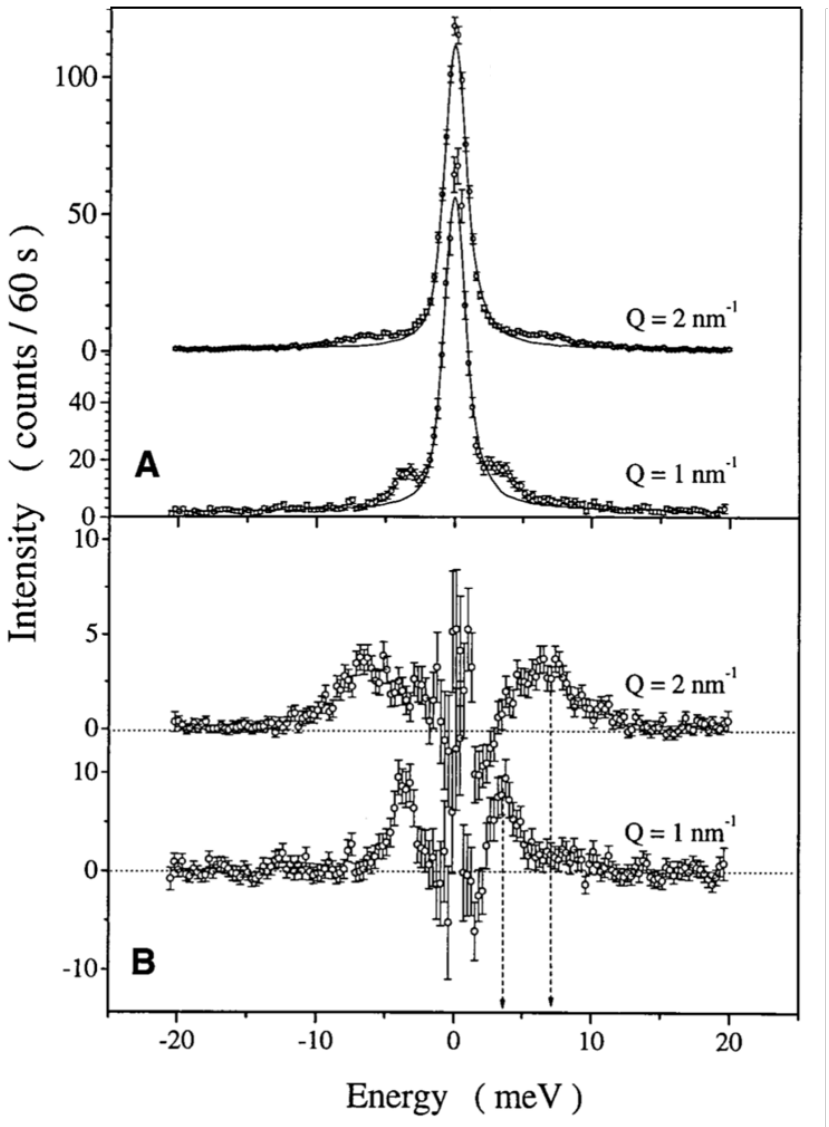

Figure 4.4: (**A**) IXS spectra of amorphous silica at 1075 K at Q = 1 nm^{-1} and Q = 2 nm^{-1} [109]. The solid line is the scaled resolution function. (**B**) IXS spectra with the scaled resolution function subtracted out to signify the inelastic peaks. Arrows denote the peaks of the inelastic signal.

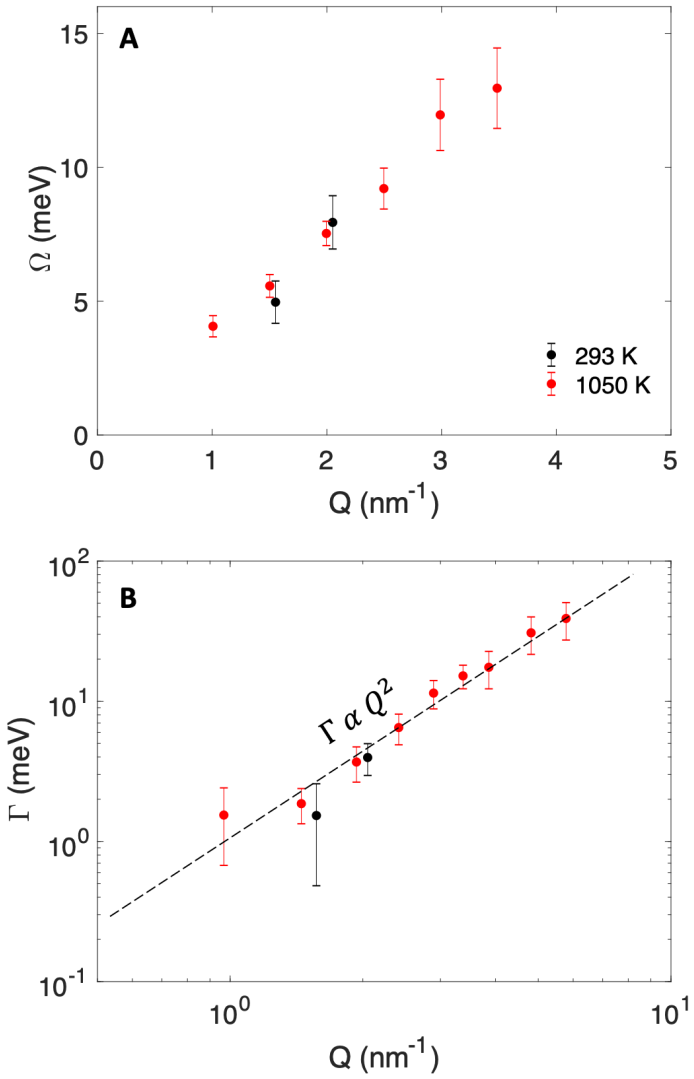

Figure 4.5: (**A**) Momentum transfer dependence of the excitation energies from IXS spectra of a-SiO_2 at 293 K [124] and 1050 K [106]. (**B**) Broadening of the excitation versus momentum transfer at 293 K and 1050 K. Q^2 is plotted as a guide to the eye.

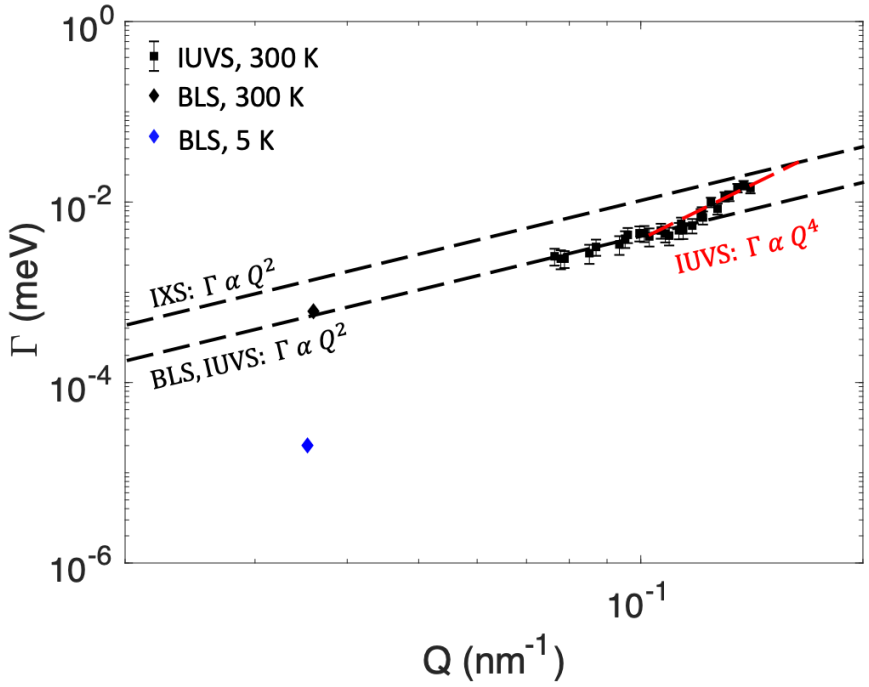

Figure 4.6: Momentum transfer dependence of the excitation energies from Brillouin light scattering (black diamond at 300 K and blue diamond at 5 K) [129] and inelastic ultraviolet scattering spectra of a-SiO_2 at 300 K [105]. Q^2 scalings extended from the IXS data Fig. 4.5 (**B**) and for the BLS and IUVS data below 0.1 nm^{-1} are shown as black dashed lines. Also plotted is the Q^4 scaling for IUVS data above 0.1 nm^{-1} as red dashed line.

In another work, the frequency at which Q^4 to Q^2 transitions has been reported at a much higher frequency around 1 THz which is where the boson peak frequency lies [130]. The underlying physics of the strong scattering regime is a matter of a debate. It has been attributed to Rayleigh-like scattering [131, 132] due to density fluctuations and elastic constant fluctuations and to a resonant interaction between soft modes and sound waves predicted by the soft potential model [133, 134]. Unlike the high momentum transfer IXS measurements that follow the Q^2 scaling, the BLS measurements show a strong temperature dependence in the broadening of the inelastic peak as shown in Fig. 4.6 (**B**), which signifies the role of anharmonicity in scattering these acoustic excitations.

Vibrations in densified amorphous silica (d-SiO_2) have also been studied [135, 136] and compared to those of powderized crystalline α-quartz [136]. In Ref. [136], d-SiO_2 was synthesized under high pressure up to 8 GPa resulting in the density of 2.67 gcm^{-3}, very close to that of α-quartz at 2.65 gcm^{-3}. The grain size of the polycrystal

was reported to be a few microns which is significantly larger than the wavelengths of vibrational excitations probed by the IXS. The spectra of the glass were measured at 570 K while those of the polycrystal were done at room temperature and the extracted inelastic peak and broadening by fitting the DHO model are shown in Fig. 4.7. Interestingly, at low momentum transfers below 2 nm^{-1} (Q_c), the polycrystal has wider inelastic peaks compared to glass which has been attributed to the additional contributions from the quasi-transverse modes in the polycrystal and the broadening exhibits Q dependence. On the other hand, in the same momentum transfer range we see a Q^4 dependence in the broadening for densified silica glass, consistent with prior IUVS and IXS spectra of regular amorphous silica at low momentum transfers as mentioned before. Above the Q_c, we see that the broadening of both polycrystal and glass have similar magnitude and show the signature Q^2 dependence. However, it is questionable if a single DHO is sufficient to fit the inelastic peaks in this Q range as the spectra are highly asymmetric as shown in Fig. 4.8 (**D**) and (**E**) and multiple peaks are clearly observed for the polycrystal.

The inelastic peak spectra of the glass and polycrystal at various momentum transfers are shown in Fig. 4.8. The instrument resolution function is plotted as a magenta dashed line in Fig. 4.8 (**A**) and the DHO fits are shown in 4.8 (**A**) and (**B**) as a solid green line. The inelastic peak predicted by the *ab-initio* lattice dynamics of the polycrystal is also shown as the solid red curve and the vertical red lines represent the predicted phonon branches of a single-crystal. As mentioned before below Q_c, the polycrystal has wider inelastic peaks compared to glass. Above the Q_c, the overall inelastic peaks of glass and polycrystal are similar; hence, it was concluded that the momentum transfer resolved vibrations for the glass arise from the linear combination of the crystal eigenstates with wavevectors within the Q resolution of the given Q [136]. However, this conclusion may be premature and oversimplified as there are some quantitative differences in the inelastic spectra of the polycrystal and glass: a large number of peaks arising from different branches of the polycrystal are clearly observed whereas they are absent in the glass spectra.

Glassy glycerol

Along with amorphous silica, glassy glycerol has also been studied extensively [108, 109, 137–139]. Glycerol shares similar characteristics of acoustic excitations with amorphous silica: temperature independence of the inelastic peak broadening Γ at high momentum transfer of a few nm^{-1}, $Q^4 \rightarrow Q^2$ transition regime, and excitations at low $Q < 0.1$ nm^{-1} having temperature dependent broadening. For this reason,

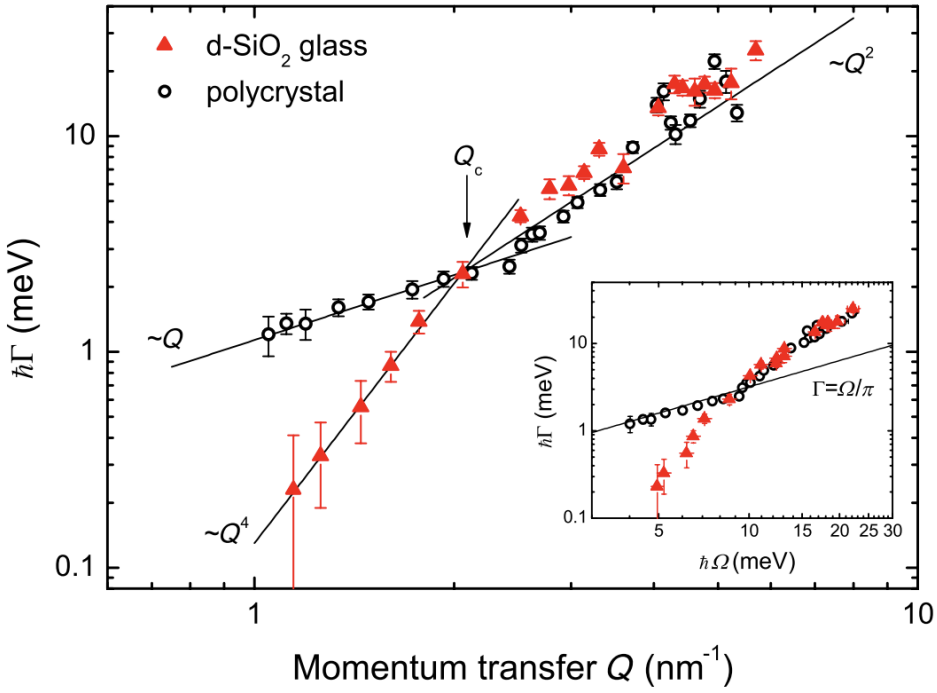

Figure 4.7: Momentum transfer dependent inelastic peak broadening of densified silica glass (solid red triangle) and polycrystal (open black circle) [136]. Various Q scalings are plotted as a guide to the eye. The crossover momentum transfer Q_c marks the transition from the strong scattering (Q^4) to the Q^2 regimes. In the inset, excitation frequency dependent broadening is shown and the black solid line represents the Ioffe-Regel crossover criteria. The Ioffe-Regel crossover for glass is at 10 meV or ~ 2 THz.

only a concise review on the inelastic scattering studies of glycerol is described here.

Inelastic peak frequency and broadening of IXS spectra of glycerol at 150 K are shown in the inset of Fig. 4.9 (**A**) [108]. The dashed red line represents the macroscopic sound limit. All the IXS data points lie slightly below this limit. Longitudinal phase velocity is plotted in Fig. 4.9 (**A**) and it is again apparent that the phase velocity does not reach the macroscopic sound velocity v_L even at the lowest momentum transfer ~ 1 nm^{-1}. There is a rapid decrease of v_L with momentum transfer (softening) until ~ 2.2 nm^{-1} and then a plateau up to ~ 4.5 nm^{-1}. Above the plateau, we start to see the expected decrease of the phase velocity due to the bending of the dispersion curve on approaching the first sharp diffraction peak. It is interesting to observe that the softening of the vibrational excitations in the low momentum transfer correspond to the strong scattering region as shown in Fig. 4.9 (**B**). Transition momentum transfer from the initial softening to the plateau region also coincides with the $Q^4 \rightarrow Q^2$ transition at 2.2 nm^{-1}. It is evident that the

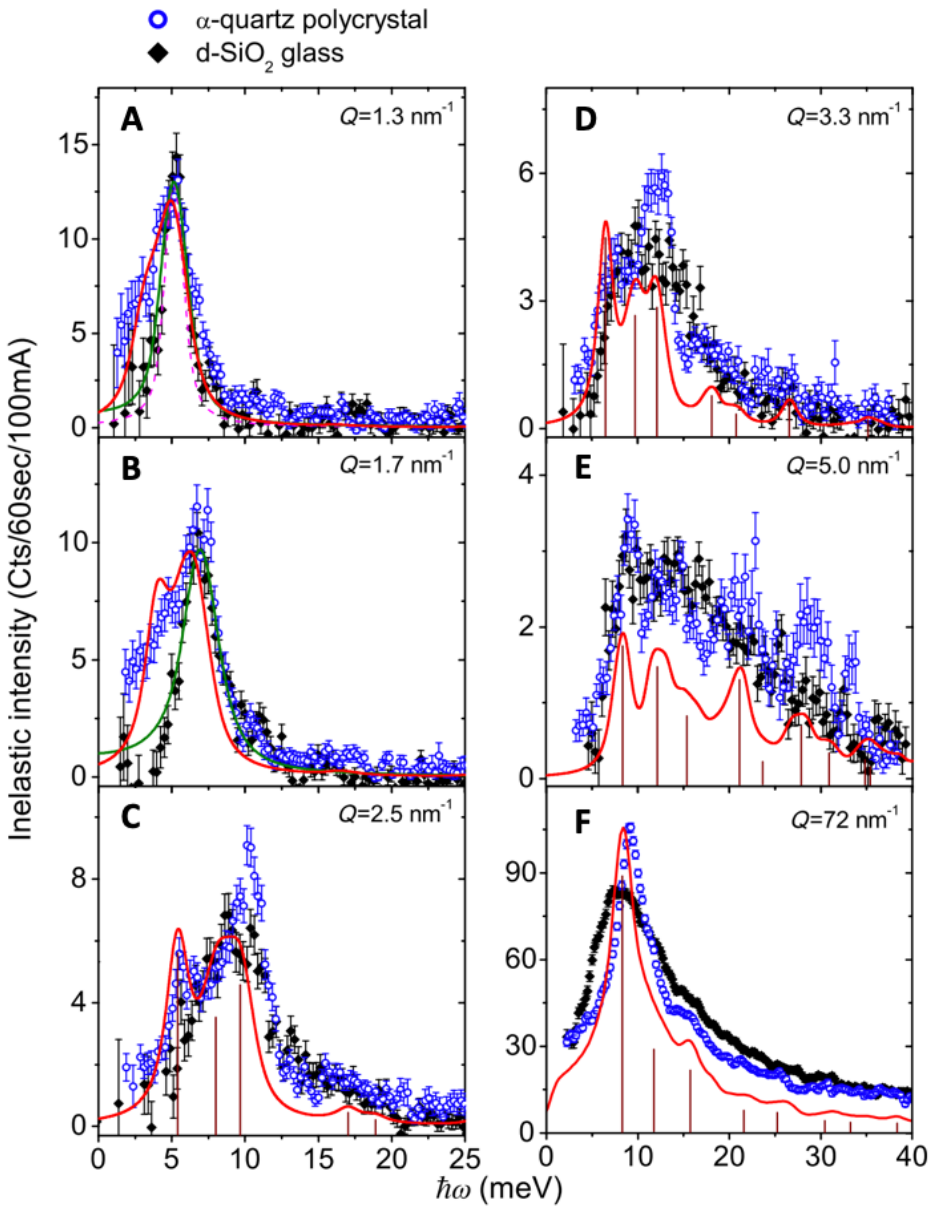

Figure 4.8: Momentum transfer dependent IXS spectra of densified amorphous silica (Solid black diamond) and α-quartz polycrystal (open blue circle) [136]. Measurements were done at 570 K (glass) and room temperature (polycrystal). Instrument resolution function is shown as magenta dashed lines in (**A**). Solid green lines in (**A**) and (**B**) are the DHO fit to the spectra. Red solid curves are obtained from *ab-initio* lattice dynamics calculations for the polycrystal and the vertical red lines represent the location of single-crystal branches.

softening of sound in the strong scattering regime directly implies the existence of acoustic-like excitations in excess of the Debye level and therefore, contributes to the boson peak which is at 4 meV or 1.7 nm^{-1}. The softening of the transverse acoustic excitations has also been shown in the strong scattering regime up to 3.5 nm^{-1} in MD simulation of glycerol glass at 150 K [138]. On the other hand, a dicrepancy with IXS experiments was reported in Ref. [138] that in the strong regime, the power law scaling is $\Gamma \alpha Q^3$ rather than the Q^4 for both the longitudinal and transverse excitations and the origin of this discrepancy is currently unknown.

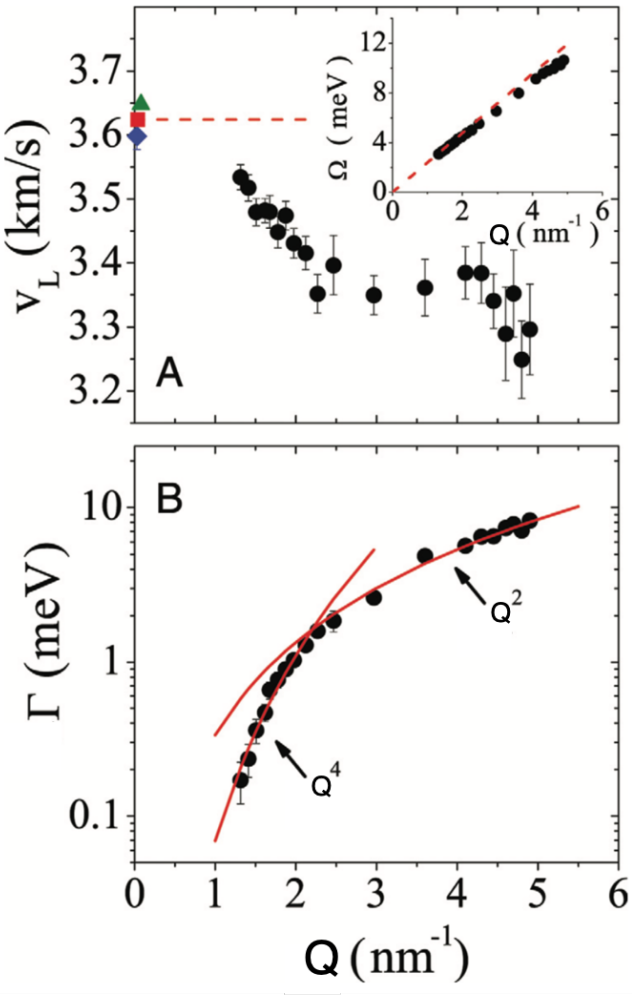

Figure 4.9: (**A**) Phase velocity of the acoustic excitations of glassy glycerol at 150 K from IXS [108]. The inset shows the dispersion of these excitations. The dashed red line represents macroscopic sound limit. (**B**) Momentum transfer dependent broadening. Similar to amorphous silica, we see a strong scattering regime up to 2.2 nm^{-1} followed by the signature Q^2 power law. A correlation between the sound softening in (**A**) and the strong scattering in (**B**) is observed.

4.4 Conclusion

In this chapter, theory of non-resonant inelastic scattering was derived and the dynamic structure factor arising from light-matter interaction was discussed. In the derivations, no assumption of the normal mode was made and unlike normal mode methods, inelastic scattering can be directly used to study collective excitations in any phases of matter. The peak frequency of the inelastic peaks represents the collective excitation energy at a particular momentum transfer with the finite linewidths representing the inverse of the collective excitation lifetimes. Results from inelastic scattering studies in amorphous silica and glycerol were discussed and some common features of the acoustic excitations such as the power laws and the temperature (in)depedence in the inelastic peak broadening were reviewed.

In the next chapter, we use molecular dynamics to calculate the dynamic structure factor to study collective excitations in amorphous silicon instead of the conventional normal mode methods metioned in Chapter 3.

Chapter 5

COLLECTIVE ACOUSTIC EXCITATIONS DOMINATE THERMAL CONDUCTION IN AMORPHOUS SILICON

This chapter has been adapted from [140]:

Moon, J., Latour, B., Minnich, A. J., Propagating elastic vibrations dominate thermal conduction in amorphous silicon, *Physical Review B*, 2018

While in-depth overview of thermal transport in a-Si from normal mode methods was discussed in Chapter 3, the results from normal mode based methods on a-Si are reiterated [42–44, 54, 56, 62, 72, 74–76] and some experimental results [85, 86, 88, 89] are discussed for completeness. Decades of work using normal mode methods have led to a general consensus that the propagating waves (in the normal mode picture, these are propagons) contribute from 20 to 50 % of thermal conductivity despite their small population existing only up to 2 to 3 THz, and that they are scattered by anharmonicity. Here, anharmonicity refers to typical phonon-phonon interactions such as normal and Umklapp scattering [44, 62]. However, we saw that there were numerous discrepancies with each one of the consensus. Size dependent thermal conductivity measurements have shown that propagating waves instead contribute a majority of the thermal conduction in amorphous silicon [85, 86, 89] and temperature dependent measurements [85, 86, 89] show a typical glass-like thermal conductivity in contrast to some predictions of crystal-like thermal conductivity due to anharmonic scattering [44, 62, 74, 75]. In addition, spectral thermal conductivity calculations of bulk a-Si [54] and thin film (14 nm thick) a-Si [77] have revealed significant suppression of spectral thermal conductivity for diffusons in the thin film which violates the definitions that diffusons are normal modes with mean free paths less than a few Å. It is difficult to locate the exact origin of the discrepancies, but these normal mode methods rely on two assumptions that atoms vibrate around their equilibrium positions and that normal modes are fundamental heat carriers in glasses.

In this chapter, we instead investigate the collective acoustic excitations in amorphous silicon by dynamic structure factor using molecular dynamics simulations

that can be directly probed by IXS. Our results support a qualitatively different picture from the predictions from the normal mode methods mentioned above. We explicitly demonstrate the propagating nature of waves up to around 10 THz that are scattered by structural disorder rather than anharmonicitity, and further show that these collective acoustic excitations dominate the thermal conduction in amorphous silicon, consistent with experiments.

5.1 Computational approach

We used lattice and molecular dynamics to examine the atomic vibrations of various amorphous domains. The molecular dynamics calculations were performed using the Large-scale Atomic/Molecular Massively Parallel Simulator (LAMMPS) with a timestep of 0.5 fs [61]. Periodic boundary conditions were imposed and the Stillinger-Weber interatomic potential was used [57]. The initial structure we considered contained 4096 atoms and was created by first melting crystalline silicon at 3500 K for 500 ps in an NVT ensemble. Next, the liquid silicon was quenched to 1000 K with the quench rate of 100 K/ps. The structures were annealed at 1000 K for 25 ns to reduce metastabilities [33]. Finally, the domain was quenched at a rate of 100 K/ps to 300 K and equilibrated at 300 K for 10 ns in an NVT ensemble using a Nose-Hoover thermostat. The structure was then equilibrated at 300 K for 500 ps in an NVT ensemble. After an additional equilibration in an NVE ensemble for 500 ps, the heat fluxes were computed for 1.6 ns in the same NVE ensemble. To check the amorphous nature of our structure, we calculated the radial distribution function, bond angle distribution, and the coordination number and compared them with those of c-Si. As mentioned in Chapter 2, radial distribution function (RDF) is given by

$$g(r) = \frac{1}{4\pi r^2 N\rho} \sum_{i\neq k}^{N} \langle \delta(r - |r_k - r_i|) \rangle \tag{5.1}$$

where r represents a distance from a reference atom, N is the number of atoms, ρ is the number density, and $\langle ... \rangle$ denotes ensemble average. Intuitively, radial distribution function represents a normalized number of atoms that are distance r away from each other. If a structure is periodic, such as in c-Si, we would expect to see sharp peaks as the distances between atoms have low spread. On the other hand, we would expect broadened peaks for amorphous solids as demonstrated in Fig. 5.1. We can see that the bond length is around 2.35 Å for both crystalline and amorphous silicon, which is consistent with scattering experiments.

From the radial distribution function, we can calculate the coordination number CN,

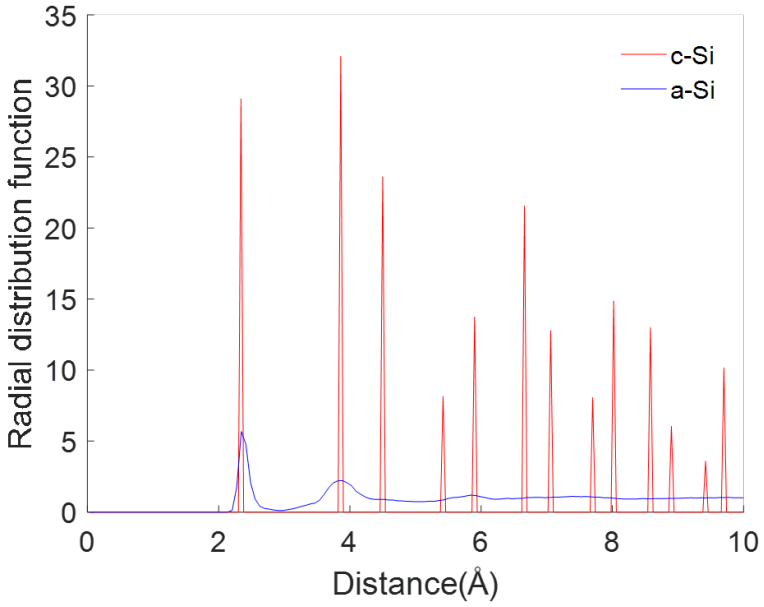

Figure 5.1: Radial distribution function comparisons between crystalline (red) and amorphous (blue) silicon. It is clear that a-Si has broadened peaks due to a spread in bond lengths.

the average number of the nearest atoms by

$$CN = \int_0^{r_c} 4\pi r^2 \rho g(r) dr \tag{5.2}$$

where r_c is the first minimum of $g(r)$ after the first peak. By comparing the coordination number of crystals with that of their amorphous counterparts, we can gain insight into how the local structure changed due to amorphization. For c-Si, we have the coordination number of 4 as expected for tetrahedrally bonded crystalline solids. On the other hand, we observe the coordination number of 4.2 for a-Si, which indicates that on average, local structures have more than 4 nearest neighbors.

Another important parameter to characterize the local structure is the bond angle distribution of atoms within r_c. For crystalline materials, we expect to observe delta function-like sharp peaks with small broadening resulting from thermal fluctuations. For disordered materials such as amorphous materials or liquids, a wide range of bond angles are observed due to the lack of symmetry as clearly seen in Fig. 5.2. We see a significantly broadened peak for amorphous silicon with about four times the full width at half maximum.

With the confirmation from several structural parameters that our structure is amorphous, dynamic structure factor was calculated in two ways: i) using the general

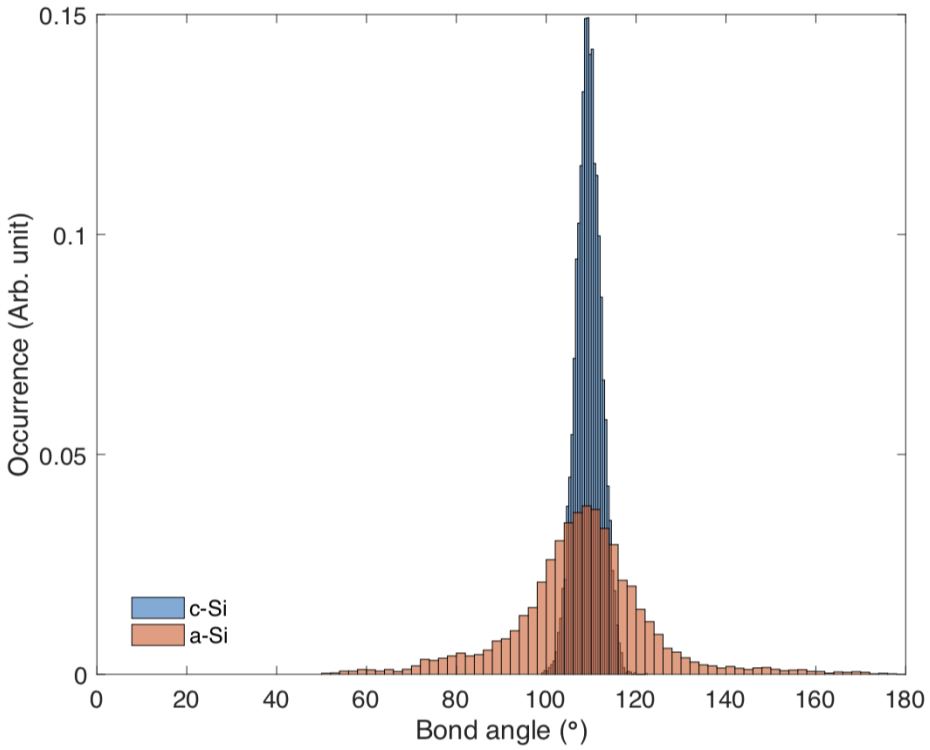

Figure 5.2: Bond angle distribution comparisons between crystalline (blue) and amorphous (orange) silicon. Both have peak the bond angle at $\sim 109.5°$, but we see a large difference in the spread of the bond angles between c-Si and a-Si. a-Si has about four times larger full width at half maximum.

definition of dynamic structure factor with velocity currents from molecular dynamics at 300 K as derived from Eq. (4.21), and ii) using the projections of the density correlation function onto the normal modes in the harmonic approximation at 0 K given by

$$S_{L,T}(\boldsymbol{q},\omega) = \sum_{\nu} E_{L,T}(\boldsymbol{q},\nu)\delta(\omega - \omega(\boldsymbol{q}=\boldsymbol{0},\nu)) \tag{5.3}$$

where the $\boldsymbol{q}$ is phonon wavevector, ω is frequency, and the summation is over all the modes ν at gamma point. E_L and E_T refer to the longitudinal polarization and transverse polarization, respectively and are defined as

$$E_{L,T}(\boldsymbol{q},\nu) = \left| \sum_i u_i^{L,T} e^{i\boldsymbol{q}\cdot\boldsymbol{r}_i} \right|^2 \tag{5.4}$$

where the summation is over all atoms indexed by i in the domain, and $\boldsymbol{r}_i$ is the equilibrium position. Here $u_i^L = \hat{\boldsymbol{q}} \cdot \boldsymbol{e}(\nu,i)$ and $u_i^T = \hat{\boldsymbol{q}} \times \boldsymbol{e}(\nu,i)$, where $\hat{\boldsymbol{q}}$ is a unit vector and $\boldsymbol{e}(\nu,i)$ is the eigenvector. Comparisons of the results from these two methods

will give us useful information about the relationship between normal modes and the collective excitations. In crystals, normal modes are the collective excitations; therefore, we would expect delta peaks in the harmonic case and broadened peaks in the velocity current formalism with the linewidths inversely proportional to the lifetime. Similarly, as prior normal mode works in a-Si have concluded, if low frequency normal modes are collective excitations that are scattered by the anharmonic interactions with one another, we should observe qualitatively similar observations to normal modes in crystals where we observe temperature induced broadening.

We calculated the eigenvectors of the 4096 atom structure using the General Utility Lattice Program (GULP) with equilibrated structures from MD [65]. As amorphous Si is isotropic, we average the dynamic structure factor over all wavevectors of the same magnitude. If collective acoustic excitations exist despite the atomic disorder, the dynamic structure factor will exhibit a clear band with a dispersion; if collective acoustic excitations are not supported, the vibrational modes will appear diffuse without an apparent dispersion.

5.2 Results

Dynamic structure factor

We first calculated directionally dependent harmonic dynamic structure factors for crystalline silicon and compared with lattice dynamics predictions [141] using the same SW potential for consistency. We see a very good agreement between dynamic structure factors and lattice dynamics as shown in Fig. 5.3 (**A**). We further performed the dynamic structure factor calculations from the velocity currents at 300 K and comparisons of these to those from harmonic approximation at [0.875 0 0] in reduced wavevector units for a transverse branch are shown in Fig. 5.3 (**B**). We see delta peaks for the harmonic case and broadened peaks at 300 K arising from anharmonic interactions of normal modes as expected. With this confirmation, we next calculate dynamic structure factors for a-Si.

The harmonic dynamic structure factor for longitudinal waves is presented in Fig. 5.4 (**A**). The figure demonstrates that despite the atomic disorder, a clear dispersion exists up to frequencies as high as 10 THz for longitudinal waves, corresponding to a wavelength of 6.5 Å. In the transverse direction, a clear dispersion with broadening is also observed up to $\sim$ 5 THz, with a similar transition wavelength at 6.6 Å . For sufficiently high frequency vibrations with wavelengths comparable to interatomic distances, the structure factor is very broad, and identifying acoustic excitations

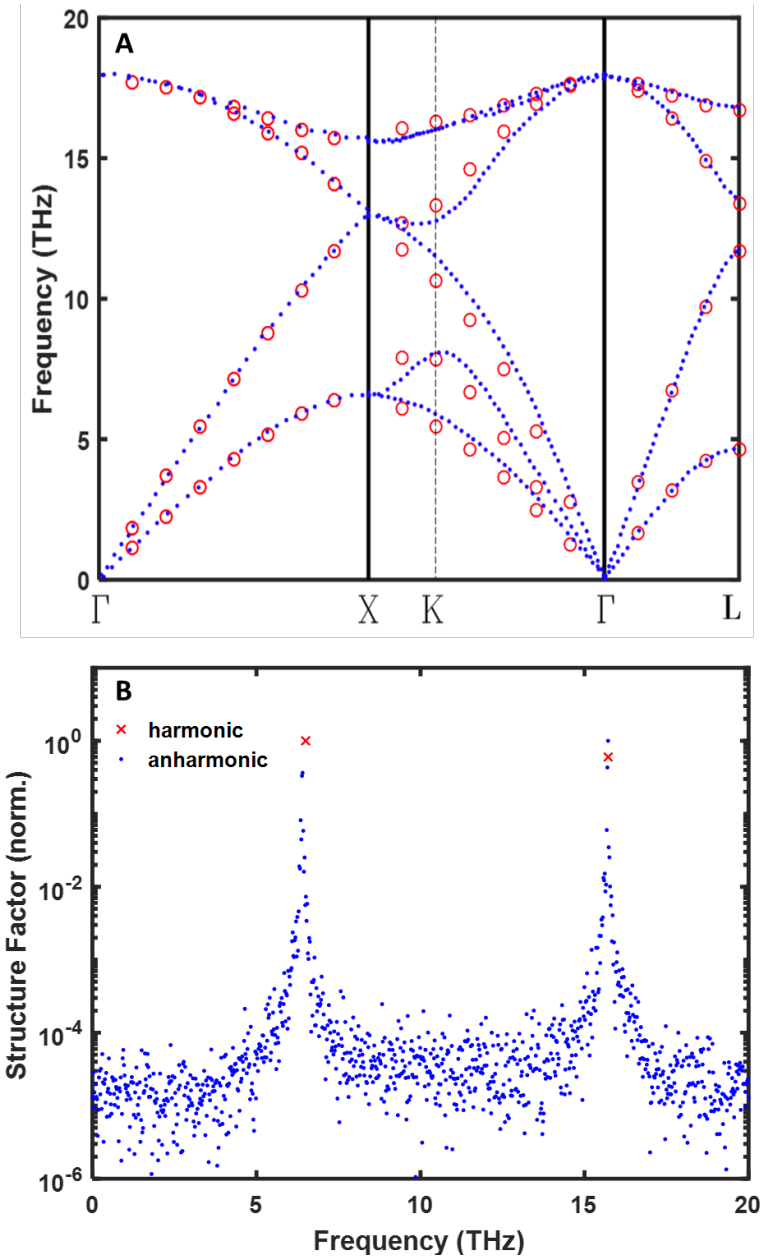

Figure 5.3: (**A**) Dispersion comparisons for crystalline silicon from our dynamic structure calculations in the harmonic approximation (red circle) and lattice dynamics predictions (blue dashed lines) by Broughton and Li [141] using the same SW potential. We see a very good agreement. (**B**) Dynamic structure factor for transverse waves for crystalline silicon with (red cross) and without (blue dot) anharmonicity at [0.875 0 0] in reduced wave vector units. For the harmonic case, we have two delta peaks for transverse acoustic and optical modes. With anharmonicity, we see a clear broadening in the peaks.

with well-defined frequency and wavevector is not possible. However, the figure

clearly shows that collective acoustic excitations comprise a substantial portion of the vibrational spectrum. Specifically, by calculating the density of states of the collective acoustic excitations with a Debye model, we estimate that about 24% of all vibrations are collective acoustic excitations. Our observation is consistent with prior calculations of dynamical structure factor [44, 142] but is inconsistent with prior conclusions that propagons have frequencies less than $2 \sim 3$ THz in amorphous silicon [43, 44, 54, 62, 76, 91].

We also observe that the lines are not narrow but have a clear broadening indicating the presence of a scattering mechanism. In crystals, this broadening is typically due to anharmonic interactions. In the harmonic lattice dynamics calculations of amorphous silicon, anharmonic interactions cannot play any role. Instead, the broadening must be due to structural disorder such as point defects and elastic modulus fluctuations. To assess how broadening due to elastic fluctuations compares to that from anharmonic interactions, we also calculate dynamic structure factors using velocity outputs from MD at 300 K [14]. The longitudinal dynamic structure factor at $q = 6.0\,\mathrm{nm}^{-1}$ with only harmonic, and harmonic and anharmonic forces are depicted in Fig. 5.4 (**B**). The two curves are nearly identical. Anharmonic broadening has essentially no effect on the lifetimes, and therefore the broadening must be solely due to structural disorder such as point defects and elastic modulus fluctuations. This is strikingly different from phonons in crystals as clearly observed in Fig. 5.3 (**B**) where anharmonicity broadening is apparent. Therefore, the picture that emerges from our calculation of dynamical structural factor of a-Si is a vibrational spectrum that is dominated by collective acoustic excitations that are scattered by structural disorder.

We next aim to extract quantitative information from the observed broadened lines for amorphous silicon. Prior works used normal mode analysis to extract lifetimes from molecular dynamics simulations [44, 62] or perturbation theory [74, 75]. Here, we use the standard scattering theory approach to obtain lifetimes by fitting a constant wavevector slice of the dynamic structure factor with a damped harmonic oscillator (DHO) model [14, 58, 142–145]. The lifetime τ at a certain frequency is related to the full-width at half-maximum Γ by $\tau = 1/\pi\Gamma$ [146]. By multiplying the lifetimes by the group velocity given by the slope of the dispersion, we also obtain mean free paths.

The results are shown in Fig. 5.5 (**A**). We see that the mean free paths span from 0.5 nm to 10 nm. At still lower frequencies that cannot be included in the present

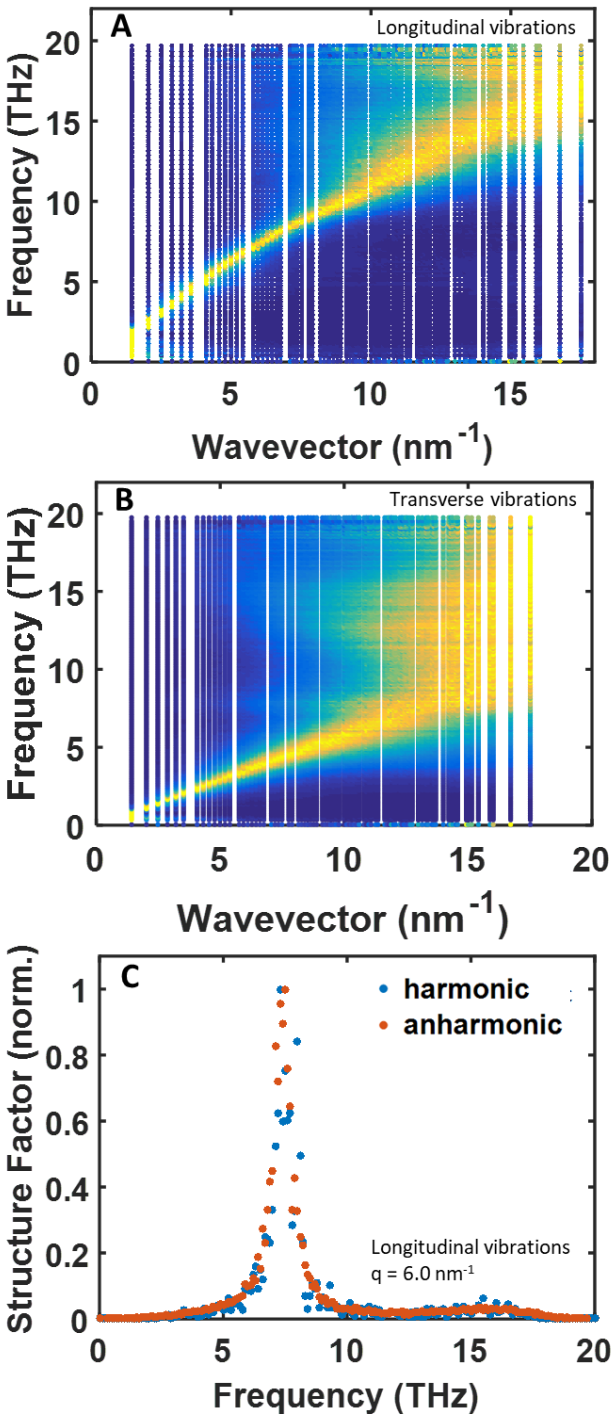

Figure 5.4: Dynamic structure factor for (**A**) longitudinal waves and (**B**) transverse waves for 4096-atom pure a-Si domain. Bright yellow indicates a high intensity of vibrations with the given frequency and wavevector. A clear phonon band is observed up to around 10 THz despite the atomic disorder. (**C**) Constant wavevector slice of the dynamical structure factor at q = 6.0 nm^{-1} in the longitudinal direction. Anharmonic broadening is negligible at 300 K.

simulations, mean free paths are likely even longer, as suggested by experiment [89]. In addition, Fig. 5.5 (**B**) plots the product of lifetime and vibrational frequency. In this plot, the Ioffe-Regel (IR) crossover from propagons to diffusons, defined as when the lifetime is equal to the period of a wave, can be indicated as a horizontal line [144]. For longitudinal waves, the IR crossover is observed at $\sim$ 10 THz and $\sim$ 5 THz for transverse waves (not shown); both of these values are in good agreement with the qualitative estimate of the transition frequency from the structure factor.

Having established that propagating acoustic excitations comprise a substantial fraction of the vibrational spectrum, we next estimate the propagating acoustic excitations contribution to thermal conductivity given knowledge of the linear, isotropic dispersion, the group velocity, and the mean free paths from Figs. 5.4 and 5.5 using a Debye model. In this model, we separate thermal conductivity contributions into longitudinal and transverse branches with group velocities obtained from the dispersion as 8000 and 3610 m s^{-1}, respectively. Recalling the bulk thermal conductivity of 1.5 $Wm^{-1}K^{-1}$ from the Green-Kubo calculation, we estimate that the acoustic excitations contribute about 1.35 $Wm^{-1}K^{-1}$ (classical), or 90 % of the GK thermal conductivity and 1.25 $Wm^{-1}K^{-1}$ (quantum) by taking into account temperature dependent phonon occupation. The primary uncertainty in this estimate is the role of vibrations of frequency less than 2 THz that are challenging to include in both the Green-Kubo and structure factor calculations; however, our conclusion still holds, even in the absence of these additional propagating vibrations in our analysis. This contribution is much larger than the values reported previously and suggests that, counterintuitively, heat transport in a-Si is dominated by a gas of collective acoustic excitations despite the atomic disorder.

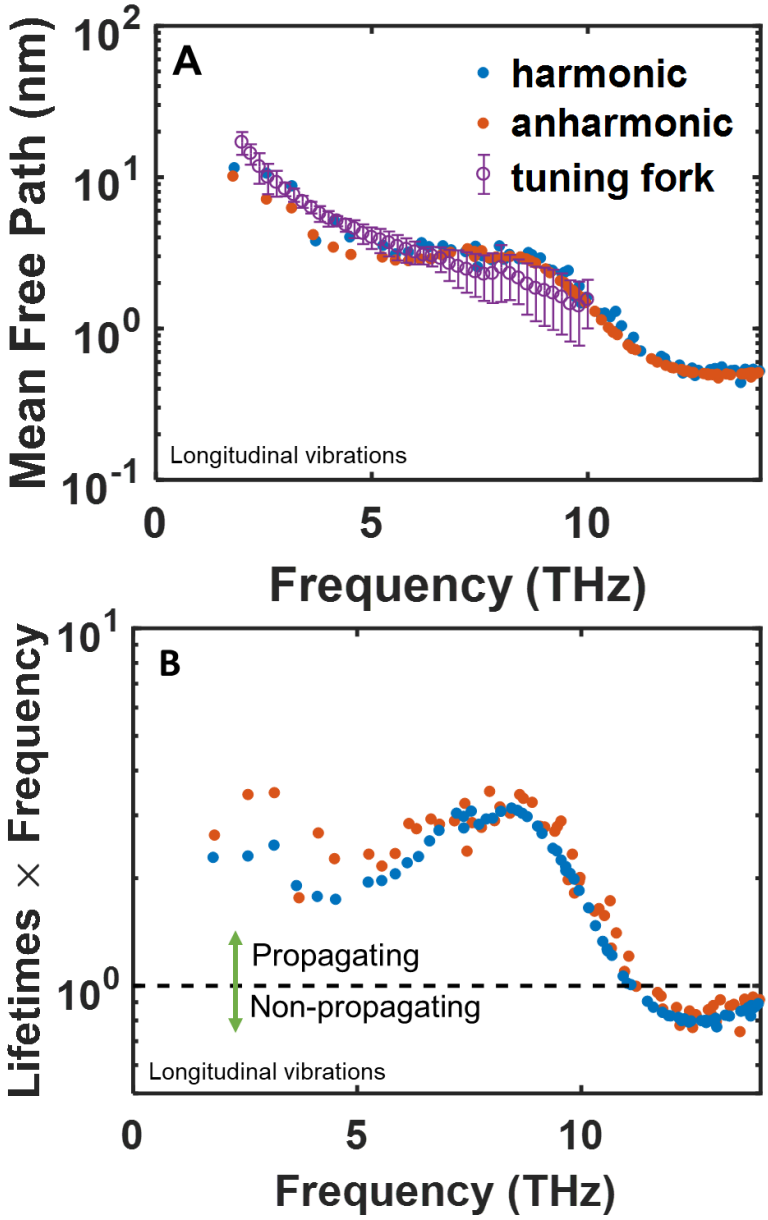

Figure 5.5: (**A**) Spectral mean free path and (**B**) lifetime multiplied by frequency versus frequency for longitudinal waves with harmonic and anharmonic forces for the 4096-atom pure a-Si domain. We observe an excellent agreement between mean free paths obtained from dynamic structure factors, and tuning fork calculations that explicitly simulate the damping of acoustic collective excitations. The Ioffe-Regel criterion occurs when lifetime multiplied by frequency equals 1. Propagons are observed up to around 10 THz for longitudinal waves as predicted from the dispersion.

Calculations using Tersoff potential

In addition to the SW potential to describe the interatomic interactions in a-Si, we have calculated thermal conductivity values from the GK formalism and dynamic structure factors using the Tersoff potential. Figure 5.6 shows the dispersion of longitudinal and transverse directions using the Tersoff potential [94] for 4096 atoms from dynamic structure factor calculations. As observed in the dispersions for the Stillinger-Weber potential, we see clear and well-defined phonon bands up to around 10 THz and 5 THz for longitudinal and transverse directions, respectively. The Ioffe-Regel crossover frequencies using Tersoff potential and the lifetimes from the structure factor agree well with those from Stillinger-Weber potential calculations.

The thermal conductivity of amorphous silicon was then calculated using the Debye model with longitudinal sound velocity of 8179 m/s and transverse sound velocity of 4198 m/s for the propagons from the structure factors (SF) and Allen and Feldman (AF) diffusivities for diffusons, and is tabulated among the works by He et al. and Lv and Henry as shown in Table 5.1 [54, 62]. For the frequency range between longitudinal and transverse Ioffe-Regel frequencies, we multiplied a factor of $2/3$ to the Allen and Feldman diffusivities to account for transverse vibrations only. We can see that our thermal conductivity prediction from structure factor and Allen and Feldman diffusivities agree well with the available data. About 90 % of thermal conductivity is calculated to be from propagating acoustic excitations and the rest from non-propagating vibrations. Calculations using the Tersoff potential also confirm that propagating acoustic excitations dominate the thermal conduction in amorphous materials as predicted by our calculations using the Stillinger-Weber potential.

Table 5.1: Thermal conductivity comparison for a-Si at 300 K using Tersoff potential without the quantum correction in the specific heat.

Source	Thermal conductivity ($Wm^{-1}K^{-1}$)
This work (GK)	2.32 ± 0.30
This work (SF + AF)	2.61
He et al. (GK) [62]	2.4 ± 0.35
Lv and Henry (GK) [54]	2 ± 0.32
Lv and Henry (GKMA) [54]	1.75

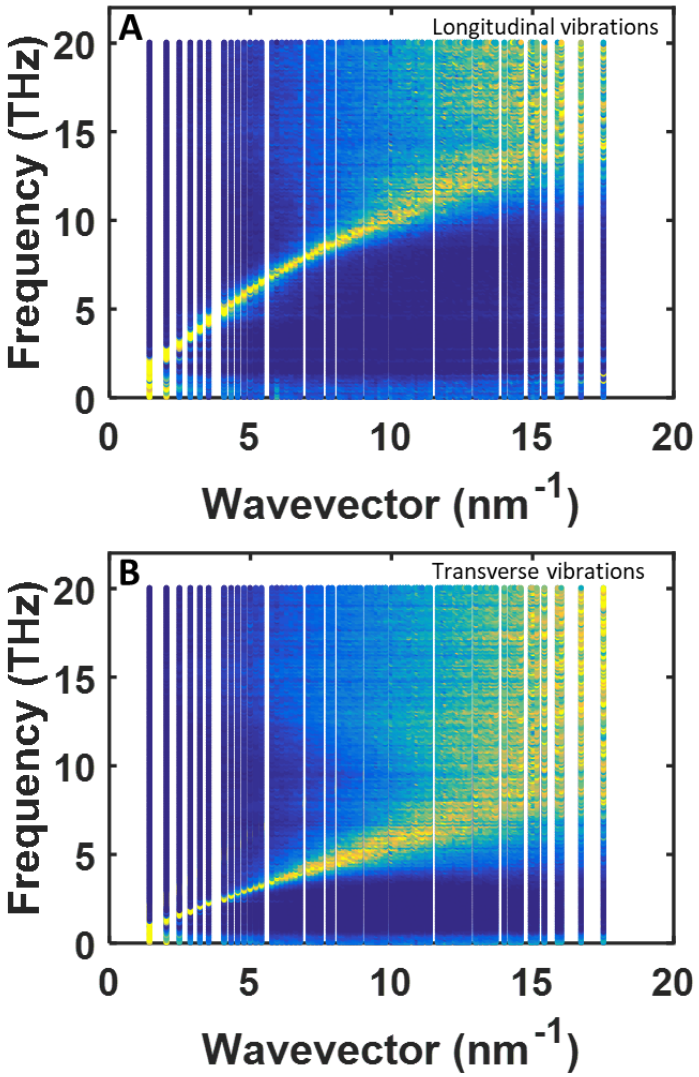

Figure 5.6: (**A**) Dispersion for longitudinal waves and (**B**) for transverse waves for 4096-atom pure a-Si domain using Tersoff potential from dynamic structure factor calculations. Bright yellow indicates a high intensity of vibrations with the given frequency and wavevector. A clear phonon band is observed up to around 10 THz for longitudinal and 5 THz for transverse directions.

Triggered wave analysis

We provide further support for our conclusions with two additional calculations. First, we explicitly demonstrate the propagating nature of vibrational modes by conducting a "tuning fork experiment" in which imposed oscillatory atomic motions at one edge of the atomic domain triggers a longitudinal wave through the a-Si. To perform this calculation, we first create a domain by repeating 4096-atom cell 10

times along one direction, resulting in a supercell of size $4.3 \times 4.3 \times 43$ nm. In the long dimension, the domain is divided into 80 slabs of width 5.431 Å. Periodic boundary conditions are applied and the temperature is set at 0.1 K to avoid additional thermal displacements. The calculation begins by rigidly displacing the first slab in the longitudinal direction for 2 ps with a sinusoidal wave with amplitude 0.01 Å and a specified frequency ranging from 2 to 10 THz. We computed the longitudinal displacements of every atom for time durations less than 2 ps to prevent edge effects, and subsequently averaged the atomic displacements within each slab.

The wave propagation in a-Si at different frequencies is shown in Fig. 5.7. It is apparent that waves do indeed propagate through a-Si at 3 THz and 8 THz as predicted by the dynamic structure factor calculations. We obtain mean free paths from these simulations by identifying the location at which the wave amplitude has decreased to $1/e$ of its original value. These mean free paths are in quantitative agreement with those from dynamic structure factor calculations as shown in Fig. 5.5 (**A**). On the other hand, the excited wave at 16 THz is damped very quickly, and by the second slab, the amplitude is already less than $1/e$ of the original value. This observation indicates that at 16 THz the vibration is non-propagating. Therefore, the "tuning fork experiment" explicitly confirms that longitudinal collective acoustic excitations exist up to a high frequency of around 10 THz in a-Si and the broadening of the inelastic peaks can be identified with broadening.

Role of elastic fluctuations

Second, we examine how the thermal conductivity is affected by the partial elimination of elastic modulus fluctuations. If our assertion regarding scattering by elastic fluctuations is true, we should observe a marked increase in thermal conductivity when these fluctuations are partially eliminated along with a temperature dependence of thermal conductivity that reflects the renewed dominance of phonon-phonon interactions. To test this hypothesis, we generated two additional domains designed to possess reduced elastic fluctuations consisting of 512 and 64-atom amorphous unit cells (AUCs) tiled to create 4096-atom structures as shown in Fig. 5.8. The 512 and 64 AUC domains were created using the same melt-quench procedure described earlier. Elastic fluctuations over a length scale equal to the AUC domain size should be eliminated because the same unit cell is tiled repeatedly in space to form the 4096 atom final structure.

We followed the same procedure as described earlier to obtain dynamic structure

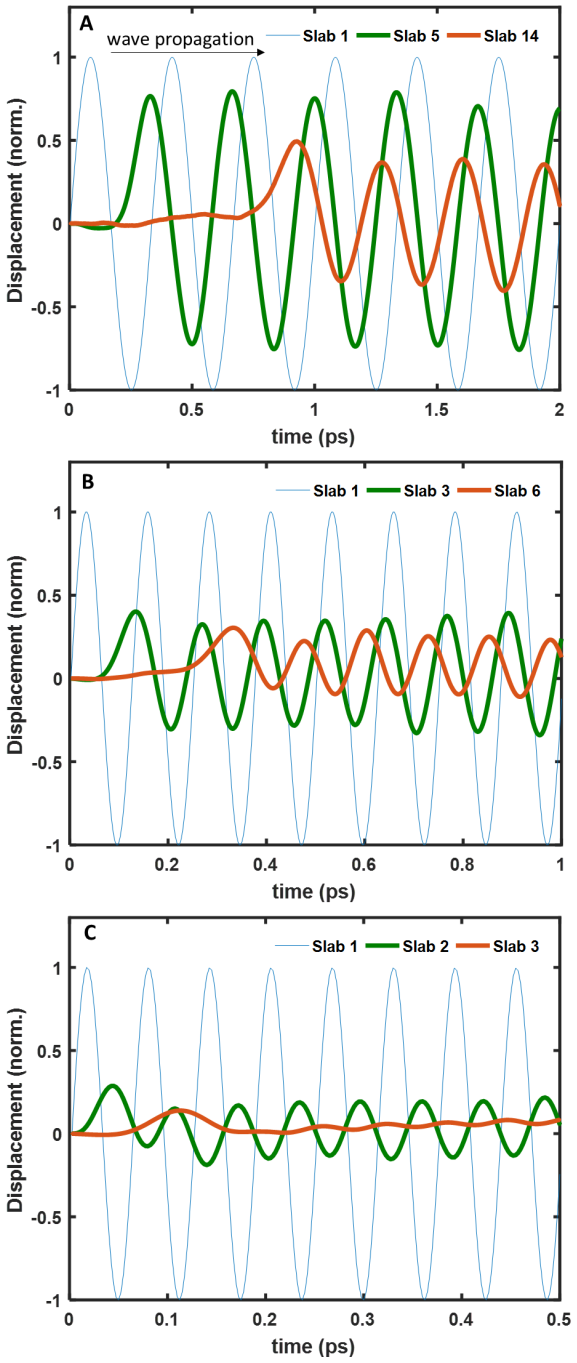

Figure 5.7: Temporal displacement of atoms in each slab with triggering frequencies (**A**) 3 THz, (**B**) 8 THz, and (**C**) 16 THz in the longitudinal direction. Each sinusoidal wave represents the averaged displacements of the atoms in a slab. By observing where the amplitudes of the displacement decrease by $1/e$, we estimate that the mean free paths are around 9 and 2 nm for 3 THz and 8 THz waves, respectively. The mean free path of the 16 THz wave is comparable to the interatomic spacing and hence the vibration is non-propagating.

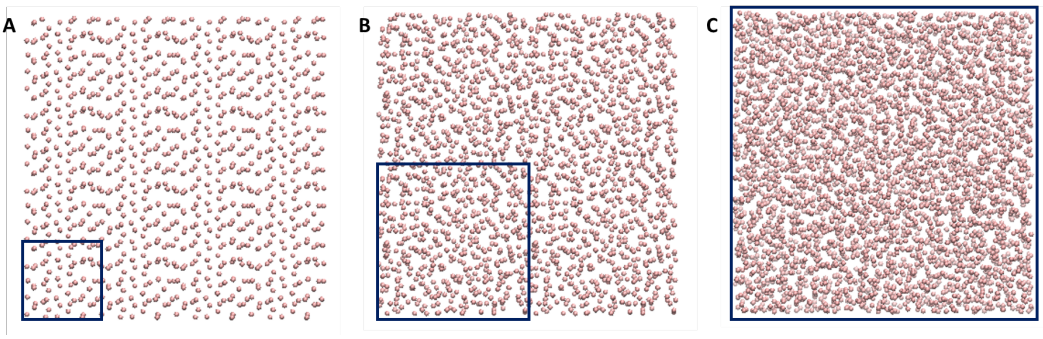

Figure 5.8: 4096-atom structures created from (**A**) 64-atom, (**B**) 512-atom, and (**C**) 4096-atom amorphous unit cells. The black box signifies the unit cell. 64-atom and 512-atom unit cell generated structures visually look more sparse than the orignal 4096-atom structure due to periodicity.

factors for the tiled structures. The structure factor for the 512-atom AUC tiled structure appears almost identical to that of the original calculation (not shown). That for the 64-atom AUC tiled structure are shown in Fig. 5.9 (**A**). We observe discrete points rather than a continuous broadening, indicative of the dynamic structure factor having delta-function-like peaks as occurs in c-Si. From a constant wavevector slice of the dynamic structure factor for the 64-atom AUC tiled structure in Fig. 5.9 (**B**), we observe that anharmonicity broadens those individual peaks of the modes from the harmonic calculations, indicating that anharmonicity plays a role in scattering these modes. Overall, these calculations indicate that the 64-atom AUC structure possesses vibrations that are characteristic of a semi-crystalline solid while the 512-atom AUC remains effectively amorphous.

We now compute the thermal conductivity of the three structures using Green-Kubo theory. The resulting thermal conductivity calculations of these structures are shown in Fig. 5.9 (c). The figure shows that the pure a-Si and the 512-atom AUC tiled structure have identical thermal conductivity with little temperature dependence. This result confirms that the 512-atom AUC structure is effectively amorphous. However, we observe a significant increase in thermal conductivity of the 64-atom AUC tiled structure, by more than a factor of 2 at room temperature, along with a marked temperature dependence. At 100 K, the thermal conductivity of the 64-atom AUC tiled structure is $\sim$ 10 $Wm^{-1}K^{-1}$, more than 6 times that of pure a-Si. Therefore, the 64-atom AUC tiled structure exhibits characteristics of crystals, and the key disorder length scale that sets the transition of thermal vibrations from crystalline to amorphous character lies between 10-20 Å.

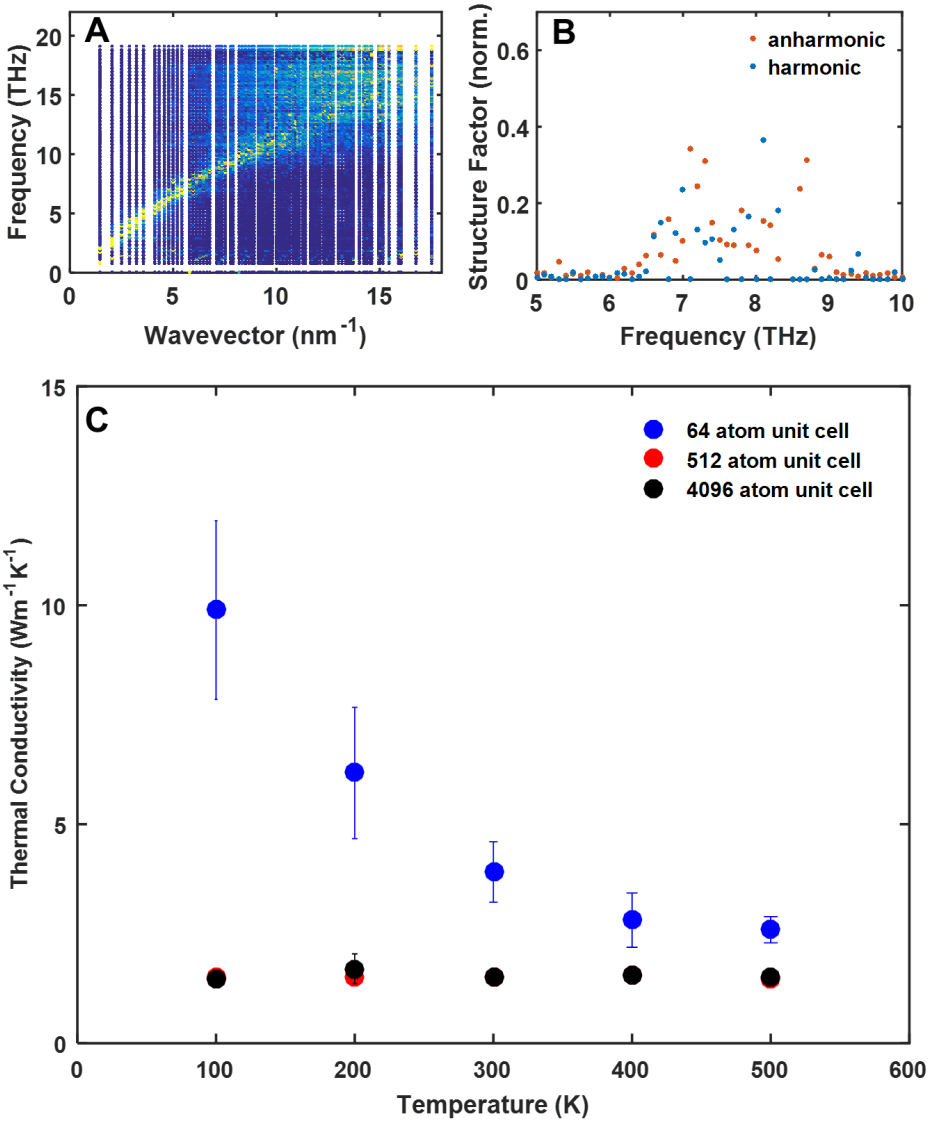

Figure 5.9: (**A**) Dynamic structure factor for longitudinal vibrations for the 64 AUC tiled structure. (**B**) Constant wavevector slice of the dynamical structure factor at q = 6.0 nm^{-1} with harmonic and anharmonic forces for the 64 AUC structure. While the harmonic calculation indicates the presence of closely spaced, discrete modes as occurs in crystals, the anharmonic case exhibits a single broadened mode due to phonon-phonon interactions. (**C**) Thermal conductivity versus temperature for three amorphous structures. No temperature dependence is observed for 512 and 4096-atom AUC structures while a noticeable dependence in temperature for the 64-atom AUC tiled structure is evident.

5.3 Discussion

Our analysis differs from prior normal mode works in two key respects. First, we identify heat carriers as the collective excitations instead of normal modes; therefore, we use a standard definition of lifetime from inelastic scattering theory as the broadening of the inelastic peak of the dynamic structure factor that arise from acoustic collective excitations that interact rather than the typical normal-mode lifetimes that assume normal modes as fundamental heat carriers.

Our tuning fork analysis explicitly shows that the physical lifetime corresponding to the damping of collective excitations is given by the lifetime from the dynamic structure factor. Those given by normal-mode analysis give lifetimes that are 3 to 10 times higher than those observed in the tuning fork calculation. It is also important to note that the tuning fork analysis was done at 0.1 K. If the triggered low frequency collective excitations were indeed governed by anharmonic scattering as predicted by some normal mode works [44, 62, 74, 75], no damping of these collective excitations should have been observed in the length scale of the computational domain. However, the fact that these excitations are damped explicitly demonstrates that they are scattered by structural disorder such as point defects and elastic fluctuations, consistent with our dynamic structure factor calculations and temperature dependent thermal conductivity measurements [85, 89].

Second, we determine the propagating to non-propagating transition frequency using the standard Ioffe-Regel criterion with the lifetimes from the structure factor, leading to transition frequencies of around $\sim$ 5 THz and $\sim$ 10 THz for transverse and longitudinal excitations, respectively. Prior works used different criteria to identify the transition frequency, such as the frequency at which diffusivities calculated by different methods are equal [44] or by looking at the degree of periodicities in the eigenvectors [76], leading to the commonly cited transition frequency of 2-3 THz (See Appendix D for more details). Our tuning fork analysis in Figs. 5.5 and 5.7 explicitly shows that modes that were previously considered to be non-propagating by the latter criterion are in fact propagating. Our conclusion that propagating acoustic excitations dominate thermal conduction in amorphous Si is a direct and unavoidable consequence of these observations.

The picture of a gas of delocalized acoustic excitations transporting heat in amorphous solids suggests follow-on experiments as well as new strategies to realize exceptional thermal materials. First, our prediction of propagating acoustic excitations existing up to around 10 THz can be verified with additional thermal

measurements on amorphous nanostructures with characteristic dimensions of less than 10 nm as well as with scattering methods such as inelastic X-ray scattering. Second, our analysis suggests that fully dense solids with exceptionally low thermal conductivity can be achieved by disrupting the propagating vibrations via enhancement of variations of local elastic modulus, expanding the physical range of thermal conductivity of solids.

5.4 Conclusion

In this chapter, instead of assuming that normal modes being the fundamental heat carriers, we draw on fundamental concepts from many-body physics and inelastic scattering theory that dictate that the collective excitation energies of a many-body interacting system are given by the poles of the single-particle Green's function. The imaginary part of this function is proportional to the dynamic structure factor that is directly measured in inelastic scattering experiments. Our results show that collective acoustic excitations can exist up to 10 THz which is significantly larger than previously predicted 2 to 3 THz by normal mode methods and that they are scattered by structural disorder such as point defects and elastic fluctuations rather than anharmonicity consistent with tuning fork calculations and temperature dependent thermal conductivity measurements. By extracting the collective acoustic excitation lifetimes from the inelastic peaks of the dynamic structure factor, the collective acoustic excitations are shown to dominate thermal conduction in amorphous silicon in agreement with size dependent thermal conductivity measurements.

In the next chapter, we show recent inelastic X-ray scattering measurements of amorphous silicon at the Advanced Photon Source and we find that the measurements are consistent with our dynamic structure factor calculations. The physical picture that emerges is, therefore, heat being carried in large part by a gas of weakly interacting collective excitations with a cutoff frequency that depends on the atomic structure and composition of the glass.

Chapter 6

THERMAL ACOUSTIC EXCITATIONS WITH ATOMIC-SCALE WAVELENGTHS IN AMORPHOUS SILICON

This chapter has been adapted from [98]:

Moon, J., Hermann, R. P., Manley, M. E., Alatas, A., Said, A. H., Minnich, A. J., Thermal acoustic excitations with atomic-scale wavelengths in amorphous silicon, *Physical Review Materials*, 2019

In the previous chapter, we reached a qualitatively different picture of atomic dynamics in amorphous silicon by calculating the dynamic structure factor, compared to the general consensus from normal mode methods that rely on normal modes as the fundamental heat carriers. It is interesting to see that despite the extensive theoretical, numerical, and experimental works in a-Si discussed in Chapter 2 and Chapter 4, inelastic X-ray scattering studies to directly probe THz collective acoustic excitations are lacking. Perhaps, the absence of the IXS measurements is due to the long attenuation lengths of hard X-rays (a few mm) for silicon and the difficulty to make bulk a-Si samples. We circumvented this problem by powderizing a-Si films to meet the attenuation lengths in the transmission geometry of IXS and dynamic structure factor of amorphous silicon was then measured at the Advanced Photon Source (APS) at Argonne National Laboratory.

In this chapter, we report the direct observation of acoustic excitations with frequencies up to 10 THz in amorphous silicon, confirming our predictions from MD simulations. The excitations have atomic-scale wavelengths as short as 6 Å and exist well into the thermal vibrational frequencies. Further simulations indicate that these high frequency collective excitations are supported due to the high group velocity and monatomic composition of a-Si, suggesting that other glasses with these characteristics may also exhibit such excitations. Our findings demonstrate that a substantial portion of thermal vibrational excitations in amorphous materials can still be described as a phonon gas despite the lack of atomic order.

6.1 Sample preparation

We prepared two samples (A1 and A2) by depositing amorphous Si onto sapphire substrates by plasma enhanced chemical vapor deposition (PECVD) at separate times with silane gas diluted (5%) in argon gas at a deposition table temperature of 473 K. To make a sample suitable for the 21.657 and 23.71 keV X-ray beams for the IXS measurements (corresponding to absorption lengths of ~ 2 mm [147]), a-Si thin films (3 μm thick) were powderized in the glovebox under either nitrogen or argon and placed in 2 mm outer diameter quartz capillary tubes with 10 μm wall thickness as shown in Fig. 6.1. Due to the small packing factor of powders, we placed additional capillary tube with powders from the same sample filled to a different height to obtain optimal scattering measurements.

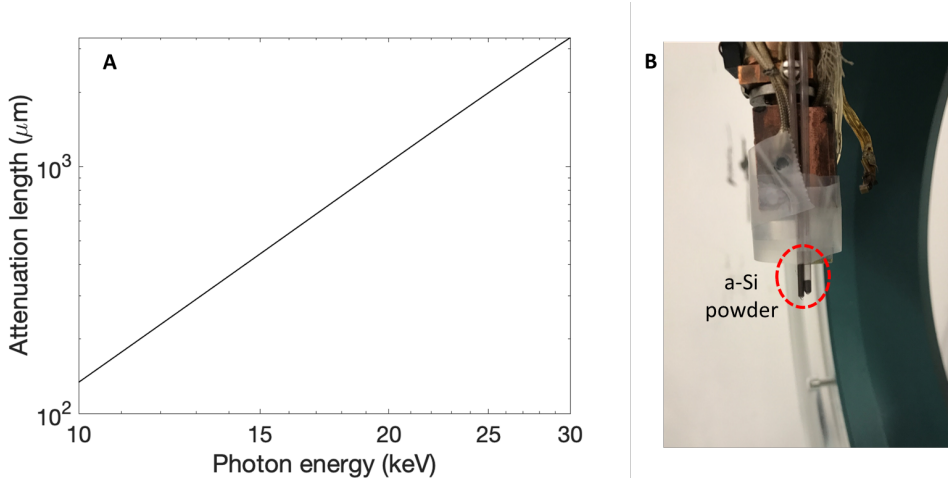

Figure 6.1: (**A**) Photon energy dependent attenuation lengths of silicon [147]. The attentuation lengths of a-Si at 21.657 and 23.71 keV are about 2 mm. (**B**) a-Si powder sample (A2) filled in two 2mm thick quartz capillary tubes, each with wall thickness of 10 μm.

The structural characterization of sample A1 is shown in Fig. 6.2. The radial distribution function (RDF) of this sample was measured by neutron scattering at Nanoscale-Ordered Materials Diffractometer (NOMAD), Spallation Neutron Source (SNS) at Oak Ridge National Laboratory. The neutron total scattering structure function was produced by normalizing the sample scattering intensity to the scattering intensity from a solid vanadium rod and subtracting the background of an empty 2 mm quartz capillary. The radial distribution function was obtained through the Fourier transform of the total scattering function with momentum transfer between 0.1 and 31.4 Å^{-1}. The RDF and X-ray diffraction pattern show broadened features, indicating that the samples are disordered. The RDF indicates that residual hydro-

gen (~ 20 at.%) is present in the sample as indicated by the negative peak at the Si-H 1.4 Å distance, but we expect little influence on our measurements considering that prior work observed no systematic change in thermal conductivity of PECVD amorphous silicon films with hydrogen content varying from 1 at. % to 20 at. % [85].

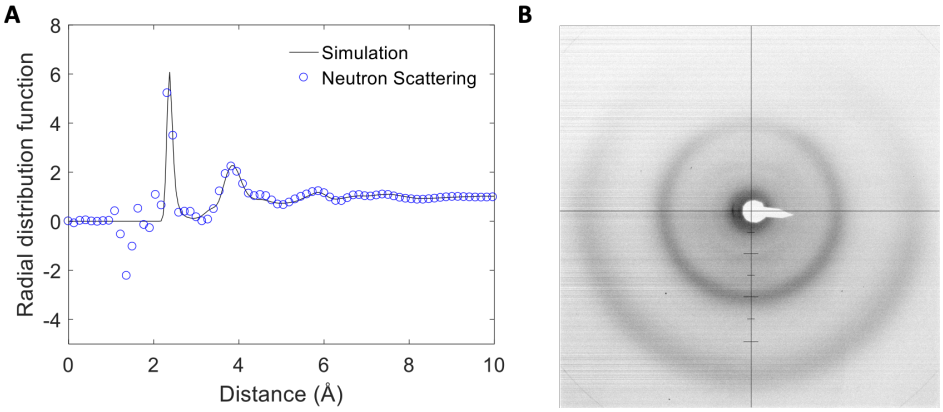

Figure 6.2: Structural characterization of a-Si powders. (**A**) Radial distribution function (blue circles) of the sample A1 compared to a calculation using an amorphous structure from molecular dynamics (line) [140]. (**B**) X-ray diffraction pattern measured at 300 K. Each tick mark represents $2\theta = 2.5°$ at X-ray energy of 21.657 keV. Broadened features in both the RDF and XRD measurements indicate an amorphous atomic structure.

6.2 Results

Inelastic X-ray scattering measurements

Dynamic structure factors from both samples (A1 and A2) were independently measured using spectrometers at sector HERIX-3 and HERIX-30 with energies of 21.657 and 23.71 keV at the Advanced Photon Source (APS) [119, 148–150], respectively. The measurements for the longitudinal branch at different momentum transfers at room temperature are shown in Figs. 6.3 (**A**) and (**B**), respectively. For simplicity, elastic peaks are not shown for each measurement. For both samples, distinct inelastic peaks are clearly visible at thermal frequencies up to around 10 THz, indicating the presence of collective acoustic excitations with well-defined frequencies and wave vectors. The wavelengths of these excitations are as small as 6 Å, comparable to the interatomic spacing in a-Si. A sudden increase in the broadening of the inelastic peaks is observed between 7.79 nm^{-1} and 11.12 nm^{-1} for A1 and between 10.0 nm^{-1} and 12.0 nm^{-1} for A2, respectively. This visual observation indicates that collective excitations with well-defined wave vector and

frequency are not supported beyond these wave vectors and frequencies.

To determine the center frequencies and the broadening of the collective excitations at each momentum transfer, the dynamic structure factor spectra were modeled with a function $S(q, \nu)$ consisting of a Lorentzian for the central elastic peak and a damped harmonic oscillator for the inelastic peaks:

$$S(q,\nu) = I_0(q)\frac{\Gamma_0(q)^2}{\Gamma_0(q)^2 + \nu^2} + [n(\nu)+1]I(q)\frac{\nu\Gamma(q)^2\Omega(q)}{[\Omega(q)^2 - \nu^2]^2 + \Gamma(q)^2\nu^2} \tag{6.1}$$

where q is the wave vector, ν is the frequency, $I_0(q)$ and $\Gamma_0(q)$ are the intensity and width of the central peak, $I(q)$ and $\Gamma(q)$ are the intensity and full width half maximum of the inelastic peak with the peak frequency $\Omega(q)$, and $n(\nu)$ is the Bose factor [110]. The function $S(q, \nu)$ is then convoluted with the pseudo-Voigt function representing the resolution function to fit to the experimental data [119].

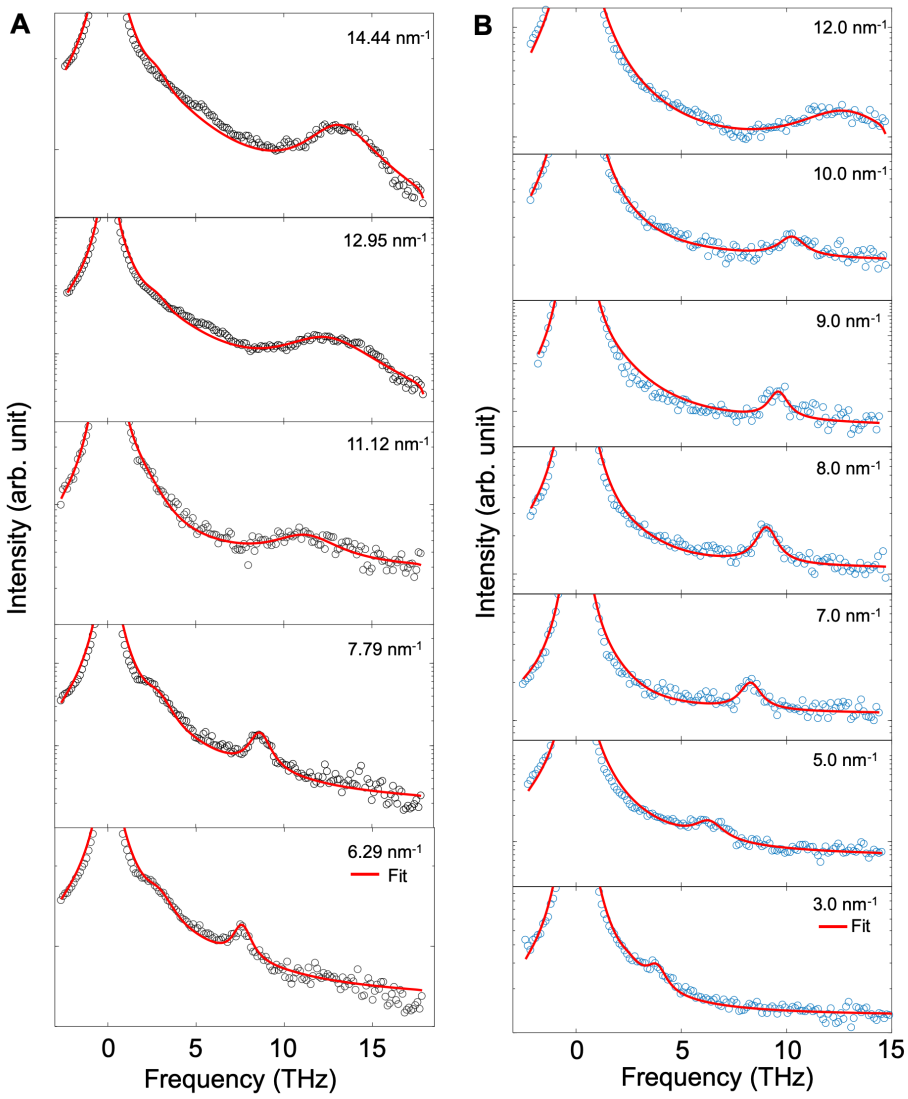

Figure 6.3: Inelastic X-ray scattering spectra of (**A**) sample A1 (black circles) and (**B**) sample A2 (blue circles) along with the fit (red lines). For both samples, sharp inelastic peaks are observed at frequencies approaching 10 THz, above which a significant increase in the broadening is seen.

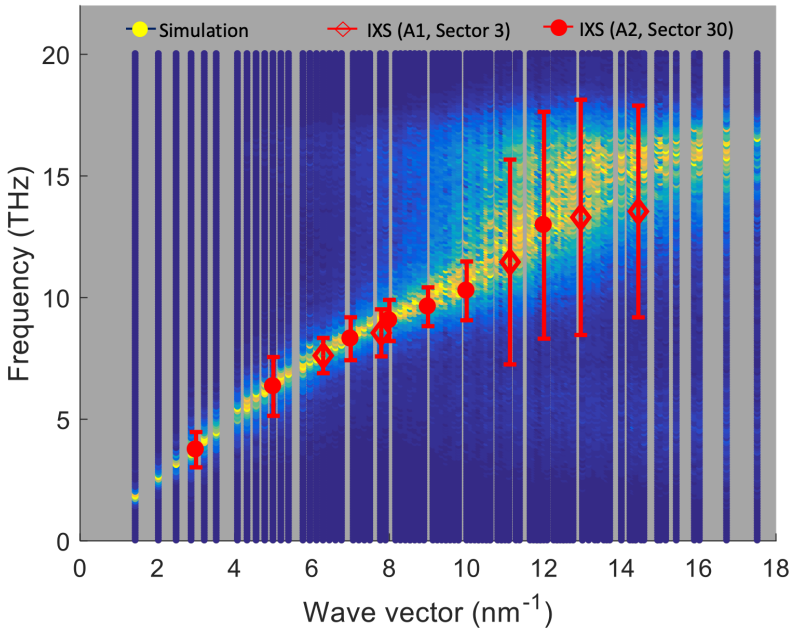

Figure 6.4: Dispersion relation from IXS measurements (diamonds from A1 using HERIX sector 3 and filled circles from A2 using HERIX sector 30) and calculated dynamic structure factor from Moon *et al.* [140]. Vertical bars represent the FWHM of the inelastic peaks. The sound velocity from the measurements is 7850 m s^{-1}, within 4% of the predicted sound velocity of 8179 m s^{-1}.

The dispersion relations of the measured acoustic excitations are plotted in Fig. 6.4 along with the calculated dynamic structure factor from Ref. [140]. The vertical bars represent the full width at half maximum of the inelastic peaks. Excellent agreement between the simulation and the IXS measurements is observed, with the sound velocities agreeing to within 4%. We attempted to include the 20 at.% hydrogen present in the sample in MD simulations using available interatomic potentials [151]; however, the thermal conductivity of the structure was inconsistent with experiments [86]. This discrepancy may arise because the interatomic potential was optimized for structural rather than dynamic properties. The good agreement between simulations with pure a-Si and experiments suggests that the presence of hydrogen does not affect the dispersion of the acoustic excitations. In both simulations and experiments, vibrations with frequencies less than $\sim$ 10 THz have a well-defined frequency and wave vector. It's worth mentioning that the calculated dynamic structure factors of Ref. [44] and [142] are also in good agreement with the measurements. These works also utilized Stillinger-Weber potential [57]. Comparison with other theoretical studies that focus on quantities of relevance to

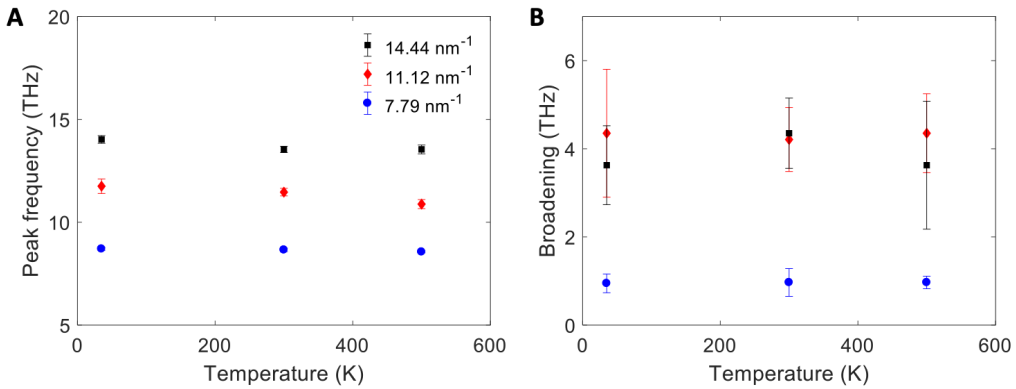

Figure 6.5: Temperature dependent IXS measurements for sample A1 (**A**) Inelastic peak frequency and (**B**) broadening at wave vectors of 7.79 (blue circles), 11.12 (red diamonds), and 14.44 nm^{-1} (black squares) across the temperature range from 35 to 500 K. A slight softening of the peak frequencies with temperature is observed, but no clear temperature dependence is found for the broadenings.

Allen-Feldman theory [43, 56] is difficult because such quantities are not directly measured in an IXS experiment.

Next, we performed additional temperature dependent IXS measurements on Sample A1 at 35 K and 500 K. Beryllium dome was used to insulate the samples and liquid Helium was used to cool the sample. The IXS signal arising from the Beryllium dome was removed from the overall signal by measuring the IXS spectra of an empty Beryllium dome. The extracted inelastic peak frequencies and broadenings are shown in Fig. 6.5. We observe a slight softening with temperature for the peak frequency, $\Omega(q)$, but no temperature dependence of the broadening is seen. This observation indicates that the origin of the broadening of the inelastic peaks is structural rather than anharmonic. The temperature independence of the broadening has also been reported in other amorphous solids such as glycerol and silica as mentioned in Chapter 3 [106, 109, 137].

6.3 Dynamic structure factor of various atomic configurations

We note that a-Si does not have a uniquely determined structure. Prior calculations [152, 153] have shown that paracrystalline amorphous silicon structures yield an RDF that is indistinguishable with that of experiments. We therefore generated 3 different amorphous silicon configurations (continuous random network, melt-quench, and crystal seed nucleation) that closely match with our RDF from neutron scattering. All three structures contain 4096 atoms and use the same SW potential with a time constant of 0.5 fs. The continuous random network model was provided by N. Mousseau and was generated from the modified Wooten-Winer-Weaire (WWW) algorithm [58]. The description of the melt-quench method is provided in detail in Moon et al. [140]. For the crystal seed nucleation method, the crystalline silicon was first melted at 3500 K at constant volume for 50 ps while the spherical crystal seed atoms (1 at.%) are kept fixed at their positions. We then quenched the structure to 1000 K at 100 K ps^{-1}. The entire structure was then annealed at 1000 K and 0 bar for 2.75 ns in NPT followed by quenching to room temperature at the same rate as before. The resulting structure from the crystal seed nucleation, therefore, has a crystalline region as shown in Fig. 6.6 (**A**). Only the crystallite atoms are displayed in the otherwise amorphous domain.

A zoomed-in view of the crystallite is depicted in Fig. 6.6 (**B**). The red atoms denote the initial crystal seed (1 at.%) and the black atoms represent the crystal growth from the seed during the annealing process. The crystalline region with well-defined tetrahedral local structures is easily observed and is estimated to be 8 at.% by dividing the number of atoms in the crystallite by the total number of atoms. The radial distribution functions of the above-mentioned structures are plotted against the experimental data from neutron scattering in Fig. 6.6 (**C**) and show good agreement. A larger crystal seed with 3 at.% was also used to create a paracrystalline silicon structure with the same procedure above, but additional distinctive peaks were clearly seen in the RDF, suggesting that the structural heterogeneity is large enough to affect the sample average of atomic density fluctuations.

The dispersion relations for longitudinal waves from dynamic structure factor calculations of these 3 amorphous silicon structures are depicted in Fig. 6.7. We observe that all structures exhibit crisp phonon disperion line up to around 10 THz above which significant broadening is clearly observed, consistent with our IXS measurements. Comparisons of the RDFs and dynamic structure factor calculations between the PECVD a-Si and three amorphous silicon models suggest that acoustic

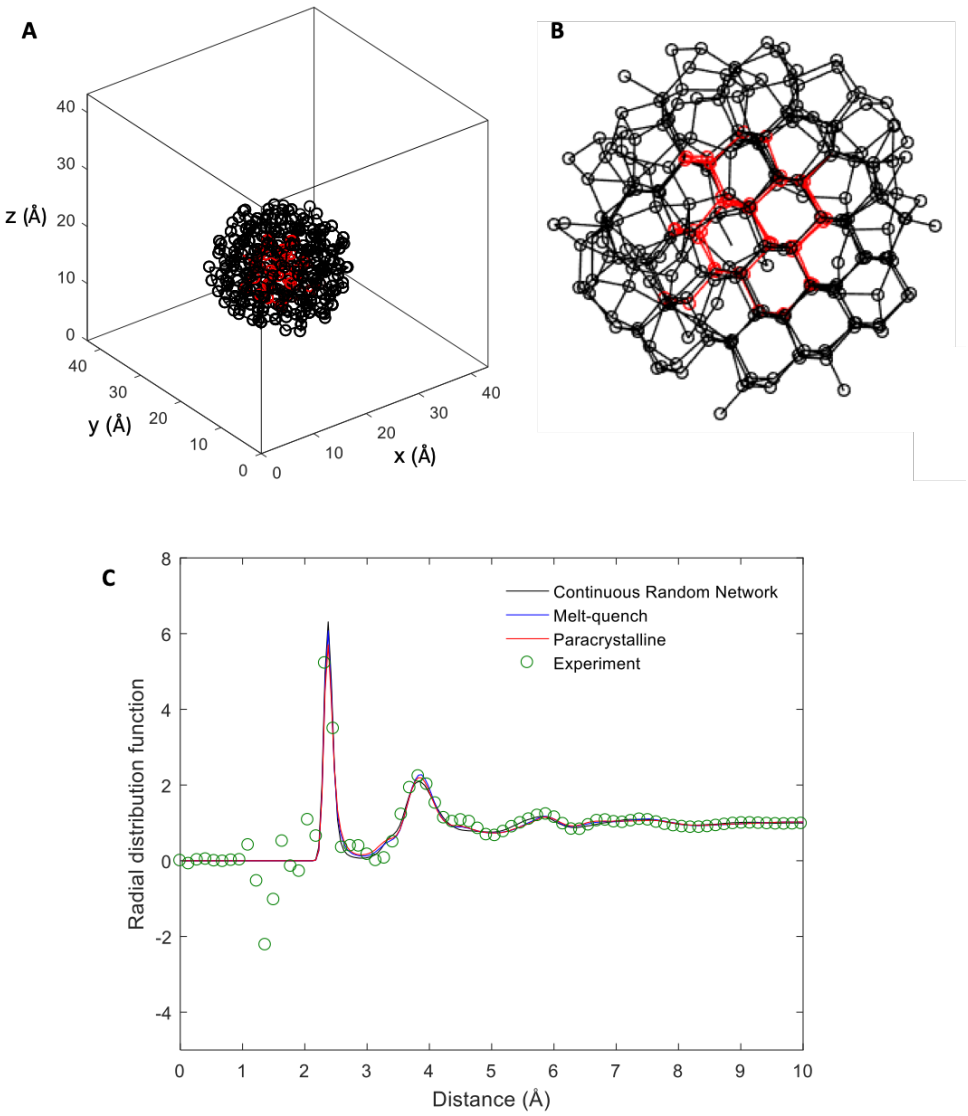

Figure 6.6: (**A**) Paracrystalline amorphous silicon structure with only the crystalline region displayed. (**B**) Zoomed-in view of the crystallite. The red atoms denote the initial crystal seed and the black atoms represent the crystal growth from annealing. The crystallite is estimated to compose 8 at.% of the structure. The crytal order is clearly observed. (**C**) Radial distribution function of continuous random network (black line), melt-quench (blue line), and paracrystalline (red line) amorphous silicon structures compared to that of experimental data (green circles).

excitations with frequencies up to 10 THz with atomic scale wavelengths exist in several possible atomic configurations of a-Si.

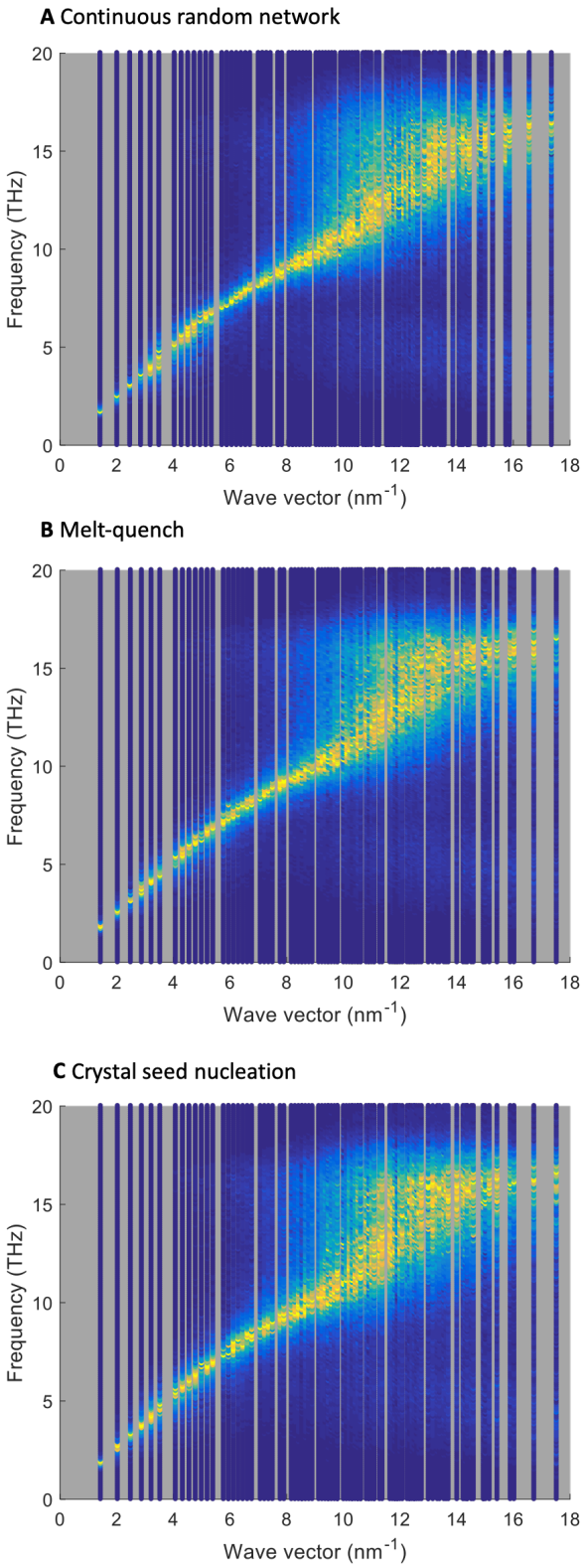

Figure 6.7: Dispersion relations for longitudinal waves for (**A**) continuous random network, (**B**) melt-quench, and (**C**) crystal seed nucleation amorphous silicon structures. All of them show a crisp phonon dispersion line up to around 10 THz above which a significant broadening is observed.

6.4 IXS measurement comparison among several amorphous materials

The broadening of the inelastic peaks, $\Gamma(q)$, of a-Si at 300 K versus wave vector are shown in Fig. 6.8 (a) along with those of various types of amorphous materials from metallic glasses to polymers studied by IXS [106, 125, 127, 128] and the computational work of Ref. [140]. A $\Gamma(q)\ \alpha\ q^2$ scaling is also shown as a guide to the eye. Previous works in other materials show a clear power law dependence. In contrast, the broadening of a-Si for both the IXS and dynamic structure factor calculations [140, 142] demonstrate a sudden increase rather than a power law dependence. This sudden increase in the broadening can also be visually observed in the raw data shown in Fig. 6.3. The origin of this increase is at present not clear and will be the subject of future work.

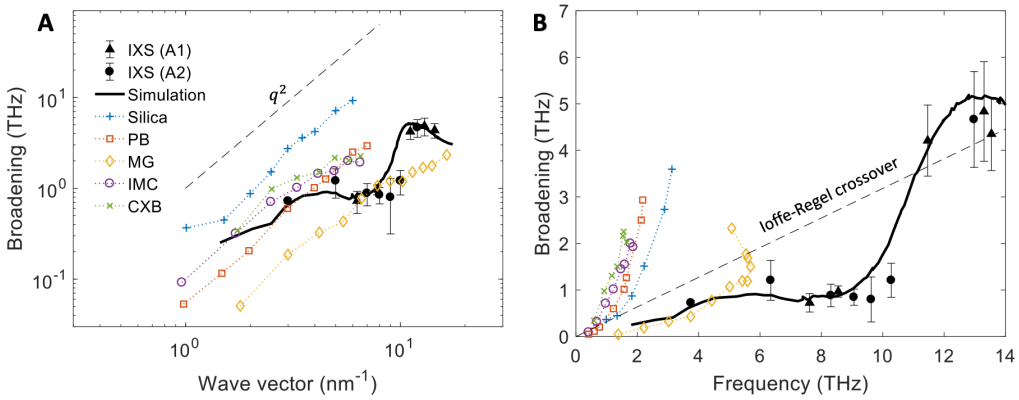

Figure 6.8: Inelastic peak broadening for a-Si (A1 and A2) and other amorphous materials. (a) Broadening Γ versus wave vector q of various amorphous materials from IXS: present measurements at 300 K (black filled triangles for A1 and black filled circles for A2), simulations from Ref. [140] (solid black line), silica at 1050 K (blue crosses) [106], polybutadiene at 140 K (PB, orange squares) [125], $Ni_{33}Zr_{67}$ metallic glass at room temperature (MG, yellow diamonds) [127], and amorphous drugs of Indomethacin (IMC, purple circles) and Celecoxib (CXB, green crosses) at room temperature [128]. A temperature dependence of the broadenings were not observed in these materials; therefore, direct comparison of our measurements at 300 K is possible. The q^2 dependence of broadening on wave vector for these materials is not observed in amorphous silicon. (b) Broadening versus frequency for the same materials as in (a). The dotted line is the Ioffe-Regel crossover defined by $\Omega = \pi\Gamma$. The Ioffe-Regel crossover occurs at around $\sim$ 10 THz for a-Si, well into the thermal frequencies. The vertical bars in the measured data are the uncertainties of fitting the damped harmonic oscillator model to the measurements. The simulated broadening lies within the vertical bars.

The definition of the frequency at which an acoustic excitation is no longer well-

defined is conventionally taken to be when the broadening $\Gamma(q) = \Omega(q)/\pi$, known as the Ioffe-Regel crossover [14, 144]. Using this criterion, we find a strikingly high crossover frequency of around 10 THz, as shown in Fig. 6.8 (b). This crossover frequency (corresponding to $\hbar\omega/k_B$ = 480 K) is well within the portion of the vibrational spectrum thermally occupied at 295 K and implies that acoustic excitations are supported for wavelengths as small as ~ 6 Å, only a few times larger than the interatomic distance of amorphous silicon (~ 2.4 Å).

Our simulations show that this unusually high crossover frequency can be explained by two features of a-Si. First, acoustic excitations cease to possess a well-defined wave vector and frequency if the disorder is sufficiently strong. a-Si is monatomic with only minor isotopic mass disorder and hence lacks the degree of disorder present in polyatomic glasses such as mass or force constant disorder. Using Tersoff potentials [154, 155], dynamic structure factors of a-SiO_2 and a-SiC were calculated. The longitudinal sound velocities of a-SiO_2 and a-SiC from dynamic structure factors are calculated to be 5567 and 9844 m s^{-1} which are within 5% of the experimental results of 5800 and 9462 m s^{-1}, respectively [106, 156]. Clear additional broadening in the dispersions is observed compared to a-Si as shown in Fig. 6.9.

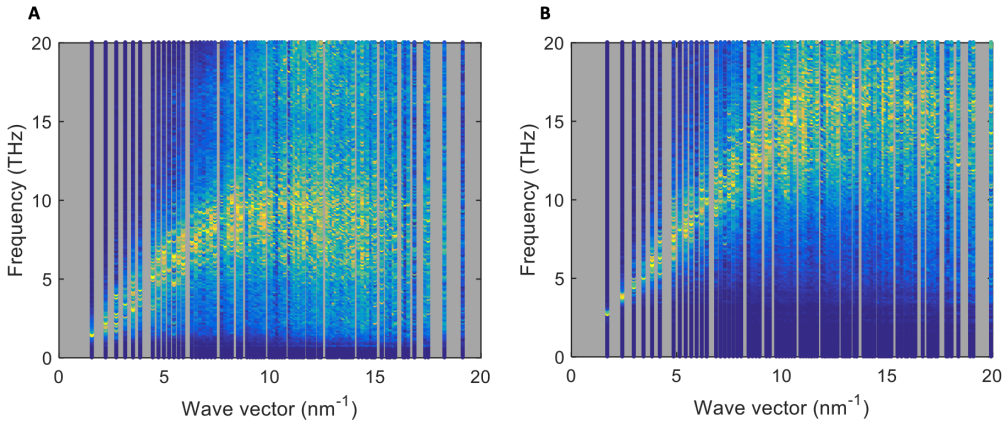

Figure 6.9: Calculated dynamic structure factor for longitudinal vibrations in (**A**) a-SiO_2 and (**B**) a-SiC. Noticeable broadening is observed for frequencies below 10 THz. The Ioffe-Regel crossover frequency is ~ 1.5 THz and ~ 8 THz for (a) and (b), respectively.

Second, a-Si has a high group velocity due to the low atomic mass of Si and stiff covalent bonds. Thus for a given wave vector, a-Si supports higher frequency excitations than for a heavier and weaker bonded amorphous material like glassy selenium. Inelastic neutron and x-ray scattering studies on glassy selenium reported

a longitudinal sound velocity of around 2000 m s^{-1} leading to a Ioffe-Regel crossover frequency of around 1-2 THz [157, 158]. For a given wave vector, a-Si supports a vibrational frequency around four times larger than that of a-Se owing to its higher group velocity.

These factors explain the presence of acoustic excitations at frequencies up to 10 THz in a-Si. Other glasses with similar characteristics, such as tetrahedral amorphous carbon, may exhibit such excitations as well, a prediction that can be verified with further inelastic scattering experiments.

Amorphous diamond is a good candidate that meets these criteria to test this assertion. Amorphous diamond (3.3 gcm^{-3}) with a very high coordination number of 3.9 has been synthesized by melting under high pressure using lasers in diamond anvil cell and quenching [159]. Our preliminary dynamic structure factor calculations of longitudinal vibrations in amorphous diamond (3.3 gcm^{-3}) that has larger sound velocity than a-Si (13.1 kms^{-1} in a-diamond vs 8 kms^{-1} in a-Si) is shown in Fig. 6.10. Remarkably, we see a crisp phonon dispersion all the way up to 50 THz. In the transverse direction, a linear, narrow dispersion is observed up to $\sim$ 25 THz. Considering that in our density of states calculations vibration spectra exist up to $\sim$ 50 THz, a majority of vibrations can, therefore, be described by collective excitations despite the intrinsic atomic disorder in amorphous diamond, a prediction that has never been made in any amorphous solids. If these predictions are confirmed, there will be a paradigm shift for how we understand the transport of heat in amorphous solids. Efforts have been made to measure the dynamic structure factor of amorphous diamonds during our more recent beamtime at APS. However, due to a very high X-ray attenuation lengths of around 1 cm and difficulty to make bulk samples and to powderize, we were unfortunately unable to obtain meaningful data.

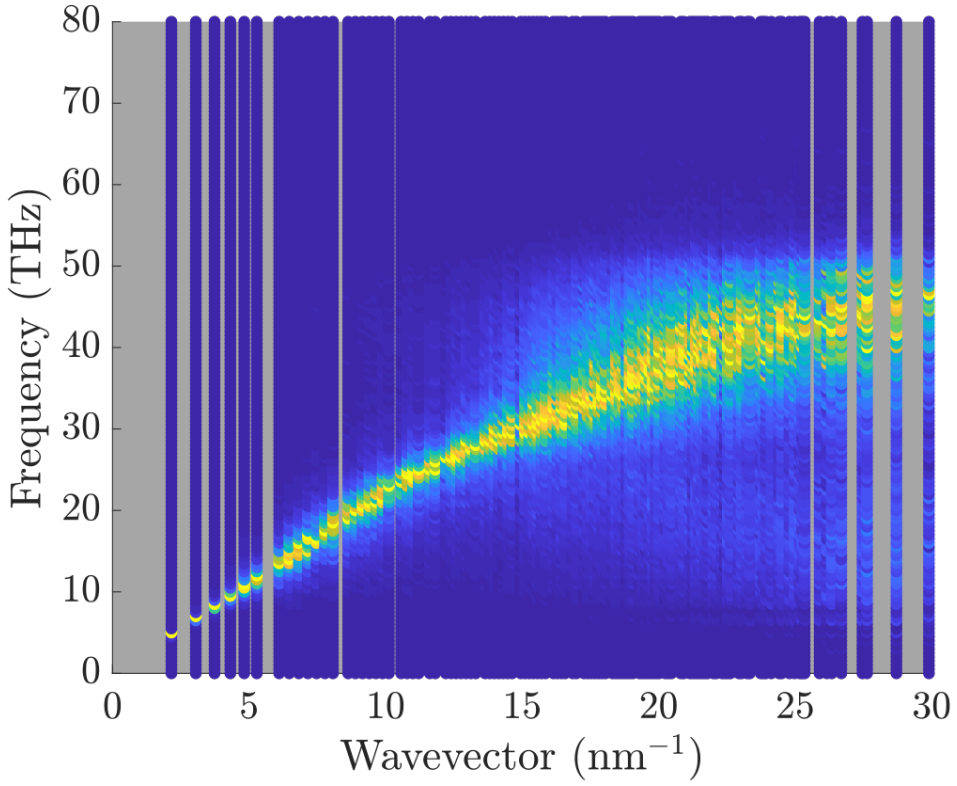

Figure 6.10: Calculated dynamic structure factor for longitudinal excitations in amorphous diamond with density of 3.3 gcm^{-3}. We see a crisp phonon dispersion up to 50 THz.

6.5 Conclusion

Despite decades of intense theoretical, numerical, and experimental works to characterize thermal transport in amorphous silicon, there has not been an inelastic scattering work to probe THz range collective excitations in a frequency and wavevector resolved manner. In this work, the first IXS measurements to directly probe these collective acoustic excitations in amorphous silicon are reported. Our measurements confirm our predictions that collective acoustic excitations are supported up to 10 THz corresponding to wavelengths as small as 6 Å, in contrast to prior predictions from normal mode methods that they only exist up to 2 to 3 THz. Comparing with other polyatomic amorphous solids, we find that these high frequency collective excitations are supported in amorphous silicon due to the monatomic composition and high group velocity. Our findings, therefore, demonstrate that the description of thermal vibrations in a-Si as a gas of acoustic excitations is unexpectedly accurate despite the lack of crystalline order, suggesting that other monatomic glasses with

high sound velocity may also support acoustic waves in the thermal spectrum.

Chapter 7

SUMMARY AND OUTLOOK

Historically, normal mode methods have been used extensively to study thermal transport in amorphous solids. Amorphous silicon has been the proving ground to develop these methods and study thermal transport of glasses due to its simpler monatomic composition and its wide usage in many applications such as solar cells and gravitational wave detectors. Decades of normal mode analysis in amorphous silicon have led to a general consensus that collective excitations exist up to 2 to 3 THz and are scattered by anharmonic interactions with one another as in crystals, and that non-propagating vibrations dominate thermal conduction. However, after a careful analysis of these works in this thesis, we find that there exist a number of discrepancies with experiments such as a strong size effects in thermal conductivity indicating that collective excitations dominate thermal transport and a weak temperature dependent thermal conductivity that are not consistent with collective excitations scattering through anharmonic interactions. Pinpointing the precise origin of these discrepancies is challenging; however, the common assumptions made in these normal mode methods are that atoms vibrate around their equilibrium positions and that normal modes are the fundamental heat carriers. We show from classical and *ab-initio* molecular dynamics simulations of amorphous silicon that atoms diffuse even at room temperature and more severely so at higher temperatures consistent with high temperature atomic diffusion measurements.

In this thesis, we have instead used inelastic scattering theory to study collective excitations in amorphous silicon that does not require the use of normal modes. We find that collective acoustic excitations dominate the thermal conduction in amorphous silicon and they are scattered by structural disorder rather than anharmonic interactions, consistent with above mentioned experimental findings. We further show that collective acoustic excitations can exist up to 10 THz, well into the thermal spectrum. These predictions were directly confirmed by our recent non-resonant inelastic X-ray scattering (IXS) measurements of amorphous silicon and our subsequent calculations demonstrate that these high frequency propagating excitations are supported in amorphous silicon due to a large sound velocity and monatomic composition, suggesting that other monatomic amorphous solids with large sound velocities may also support these thermal excitations.

Appendix A

HAMILTONIAN FOR INELASTIC SCATTERING

To derive an explicit expression for the double differential cross section, we start from the Hamiltonian describing the interaction between electrons in the sample and the time dependent electromagnetic field. We treat the matter quantum mechanically, and treat the electromagnetic field classically. For the electromagnetic field, we assume that only light influences the matter through a time-dependent interaction potential and that the matter does not affect the light. Non-relativistic electrons are assumed. Here are some comments and summaries from classical electrodynamics:

1. Maxwell's equations describe the electric and magnetic fields $(\boldsymbol{E}, \boldsymbol{B})$.

2. The time-dependent interaction between light and matter must be described in terms of a potential rather than a field.

3. To describe $\boldsymbol{E}$ and $\boldsymbol{B}$, a vector potential $\boldsymbol{A}(\boldsymbol{r}, t)$ and a scalar potential $\phi(\boldsymbol{r}, t)$ are used.

4. Since the potentials are not uniquely determined, Coulomb gauge is used for this derivation:

$$-\nabla^2 \boldsymbol{A}(\boldsymbol{r}, t) + \frac{1}{c^2}\frac{\partial^2 \boldsymbol{A}(\boldsymbol{r}, t)}{\partial t^2} = 0 \tag{A.1}$$

$$\nabla \cdot \boldsymbol{A}(\boldsymbol{r}, t) = 0 \tag{A.2}$$

. With the Coulomb gauge, the electric field and the magnetic field can be expressed as

$$\boldsymbol{E} = -\frac{\partial \boldsymbol{A}(\boldsymbol{r}, t)}{\partial t} \tag{A.3}$$

$$\boldsymbol{B} = \nabla \times \boldsymbol{A}(\boldsymbol{r}, t). \tag{A.4}$$

Now, we find a classical Hamiltonian that describes charged particles in the EM field in terms of the vector potential. The Lorentz force acting on a particle with charge q is given by

$$\boldsymbol{F} = q(\boldsymbol{E} + \boldsymbol{v} \times \boldsymbol{B}) \tag{A.5}$$

where $\boldsymbol{v}$ is the velocity of the particle. The Lorentz force can also be written in terms of the total potential energy, U, in Lagrangian mechanics as

$$\boldsymbol{F} = -\nabla \boldsymbol{U} + \frac{d}{dt}\nabla_{\boldsymbol{v}} U. \tag{A.6}$$

Equating the above two expressions, we obtain

$$U = q\phi - q\boldsymbol{v} \cdot \boldsymbol{A}. \tag{A.7}$$

Now, the Lagrangian can be written in terms of the kinetic and potential energy of the particle

$$\begin{aligned} L &= T - U \\ &= \frac{1}{2} m\boldsymbol{v}^2 + q\boldsymbol{v} \cdot \boldsymbol{A} - q\phi. \end{aligned} \tag{A.8}$$

In addition, the Hamiltonian is

$$\begin{aligned} H &= \boldsymbol{p} \cdot \boldsymbol{v} - L \\ &= \boldsymbol{p} \cdot \boldsymbol{v} - \frac{1}{2} m\boldsymbol{v}^2 - q\boldsymbol{v} \cdot \boldsymbol{A} + q\phi \end{aligned} \tag{A.9}$$

where

$$\boldsymbol{p} = \frac{\partial L}{\partial \boldsymbol{v}} = m\boldsymbol{v} + q\boldsymbol{A}. \tag{A.10}$$

Velocity, $\boldsymbol{v}$, can then be written in terms of $\boldsymbol{p}$ as

$$\boldsymbol{v} = \frac{1}{m}(\boldsymbol{p} - q\boldsymbol{A}). \tag{A.11}$$

Plugging in the velocity into the Hamiltonian,

$$\begin{aligned} H &= \frac{1}{m}\boldsymbol{p} \cdot (\boldsymbol{p} - q\boldsymbol{A}) - \frac{1}{2m}(\boldsymbol{p} - q\boldsymbol{A})^2 - \frac{q}{m}(\boldsymbol{p} - q\boldsymbol{A}) \cdot \boldsymbol{A} + q\phi \\ &= \frac{1}{2m}\big[\boldsymbol{p} - q\boldsymbol{A}\big]^2. \end{aligned} \tag{A.12}$$

In the second step, we assume that the scalar potential, ϕ is negligible. Above derivations have used the SI units. However, many condensed matter theorists typically use the CGI units, and the Hamiltonian including the electromagnetic wave and electron interaction derived above in CGI units, can be written as

$$H = \frac{1}{2m}\sum_i \big(\boldsymbol{p}_i - \frac{q}{c}\boldsymbol{A}\delta(\boldsymbol{r} - \boldsymbol{r}_i)\big) \cdot \big(\boldsymbol{p}_i - \frac{q}{c}\boldsymbol{A}\delta(\boldsymbol{r} - \boldsymbol{r}_i)\big) + \sum_i V(\boldsymbol{r}_i) + V_{int}^{e-e} \tag{A.13}$$

where c is the speed of light, sum is over all electrons, $V(\boldsymbol{r}_i)$ is the potential field, and V_{int}^{e-e} describes the electron-electron interaction. Spin contribution is neglected.

Appendix B

AUTOCORRELATION FUNCTIONS

We have seen that many vibrational properties of materials can be found from autocorrelation functions. In this chapter, basics and properties of autocorrelation functions are briefly reviewed.

Let us first define a time-limited stationary stochastic signal $x(t)$ for $0 \leq t \leq T$. For $t > T$, $x(t)$ is zero. Its autocorrelation can be defined as

$$\begin{aligned} AC_{xx}(t, t+\tau) &= E[x(t)x(t+\tau)] \\ &\approx \frac{1}{T}\int_0^T x(t)x(t+\tau)dt \end{aligned} \tag{B.1}$$

where E refers to the expectation value. The first line is valid for stochastic signals and the second line is more general and can be used for deterministic processes as well. Some important properties of autocorrelation functions of stationary stochastic processes are listed below.

- For wide-sense stationary stochastic processes, the autocorrelation is shift-invariant and their expectation values are constant.

$$AC_{xx}(t, t+\tau) = AC_{xx}(\tau) \tag{B.2}$$

- The autocorrelation function is symmetric

$$AC_{xx}(\tau) = AC_{xx}(-\tau). \tag{B.3}$$

- The autocorrelation function is at its maximum at $\tau = 0$ and its value is equal to the variance of the signal.

- The derivative of the autocorrelation function can be written as

$$\begin{aligned} \frac{d(AC_{xx}(\tau))}{d\tau} &= E[x(t)\dot{x}(t+\tau)] = AC_{x\dot{x}}(\tau) \\ &= -E[x(t-\tau)\dot{x}(t)] = -AC_{\dot{x}x}(\tau) \\ \frac{d(AC_{xx}(\tau))}{d\tau} &= -\frac{d(AC_{xx}(-\tau))}{d\tau}. \end{aligned} \tag{B.4}$$

- The second derivative of the autocorrelation function can be written as

$$\frac{d^2(AC_{xx}(\tau))}{d\tau^2} = \frac{d(AC_{x\dot{x}}(\tau))}{d\tau} = AC_{x\ddot{x}}(\tau) = -AC_{\dot{x}\dot{x}}(\tau). \tag{B.5}$$

B.1 Weiner Khinchin's Theorem

The autocorrelation, $R(t)$, of a function, $f(x)$ is defined as

$$R(t) \equiv \int_{-\infty}^{\infty} \bar{f}(\tau) f(t+\tau) d\tau. \tag{B.6}$$

Recall that the inverse Fourier transform of $F(\nu)$ is defined by

$$f(\tau) = \int_{-\infty}^{\infty} F(\nu) e^{i2\pi\nu\tau} d\nu \tag{B.7}$$

with a complex conjugate of

$$\bar{f}(\tau) = \int_{-\infty}^{\infty} \bar{F}(\nu) e^{-i2\pi\nu\tau} d\nu. \tag{B.8}$$

Plugging in $\bar{E}(\tau)$ and $E(t+\tau)$ into the autocorrelation gives

$$\begin{aligned}
R(t) &= \int_{-\infty}^{\infty} \left[\int_{-\infty}^{\infty} \bar{F}(\nu) e^{-i2\pi\nu\tau} d\nu \right] \left[\int_{-\infty}^{\infty} F(\nu') e^{i2\pi\nu'(t+\tau)} d\nu' \right] d\tau \\
&= \int_{-\infty}^{\infty} \int_{-\infty}^{\infty} \int_{-\infty}^{\infty} \bar{F}(\nu) F(\nu') e^{-i2\pi\tau(\nu-\nu')} e^{i2\pi\nu' t} d\tau d\nu d\nu' \\
&= \int_{-\infty}^{\infty} \int_{-\infty}^{\infty} F(\nu) F(\nu') \delta(\nu'-\nu) e^{i2\pi\nu' t} d\nu d\nu' \\
&= \int_{-\infty}^{\infty} |F(\nu)|^2 e^{i2\pi\nu t} d\nu \\
&= \mathrm{IFT}\left[F(\nu)^2 \right].
\end{aligned} \tag{B.9}$$

Weiner Khinchin's theorem can be used to calculate Green-Kubo thermal conductivity, vibrational density of states, and dynamic structure factors as they are based on autocorrelation functions.

Appendix C

GREEN-KUBO THERMAL CONDUCTIVITY

The Green-Kubo formalism is based on classical statistical thermodynamics. There are several derivations that result in the same formula but in this chapter, I will mainly adapt the derivations by Helfand and Kaviany.

The energy equation can be written as

$$nc_v \frac{\partial E_o(\boldsymbol{r},t)}{\partial t} = k\nabla^2 E_o(\boldsymbol{r},t) \tag{C.1}$$

where $E_o(\boldsymbol{r},t) = E(\boldsymbol{r},t) - \langle E(\boldsymbol{r},t)\rangle$, the time and position dependent energy deviation. $E(\boldsymbol{r},t)$ is the actual energy and $\langle E(\boldsymbol{r},t)\rangle$ denotes the expectation energy. n and c_v correspond to density and specific heat. For discrete particle systems, $E_o(\boldsymbol{r},t) = \sum_j E_{o,j}(\boldsymbol{r},t)\delta[\boldsymbol{r} - \boldsymbol{r}_j(t)]$ where index j denotes the atom identity.

Let us define the Fourier transform of $E_o(\boldsymbol{r},t)$ as $\tilde{E}(\boldsymbol{r},t)$

$$\tilde{E}(\boldsymbol{r},t) = \int E_o(\boldsymbol{r},t)e^{i\boldsymbol{\kappa}\cdot\boldsymbol{r}}\,d\boldsymbol{r} = \sum_j E_{o,j}(t)e^{i\boldsymbol{\kappa}\cdot\boldsymbol{r}_j(t)} \tag{C.2}$$

The energy equation can then be written in terms of $\tilde{E}(\boldsymbol{r},t)$ as

$$\frac{\partial \tilde{E}(\boldsymbol{r},t)}{\partial t} = -\frac{\kappa^2 k}{nc_v}\tilde{E}(\boldsymbol{r},t) \tag{C.3}$$

by using the Fourier transform identity that $FT(\frac{df}{dx}) = -i\kappa F(\kappa)$ where FT is the Fourier transform operation and $F(\kappa)$ is the Fourier transform of $f(x)$. The solution with the initial condition, $\tilde{E}(\boldsymbol{r},0)$, is then

$$\tilde{E}(\boldsymbol{r},t) = \tilde{E}(\boldsymbol{r},0)e^{-\frac{\kappa^2 kt}{nc_v}} \tag{C.4}$$

Multiplying the complex conjugate of the initial condition to both sides, we have

$$\tilde{E}(\boldsymbol{r},t)\tilde{E}^*(\boldsymbol{r},0) = \sum_j E_{o,j}(t)e^{i\boldsymbol{\kappa}\cdot\boldsymbol{r}_j(t)} \sum_l E_{o,l}(0)e^{i\boldsymbol{\kappa}\cdot\boldsymbol{r}_l(0)} \tag{C.5}$$

and we can further write

$$\sum_j E_{o,j}(t)e^{i\boldsymbol{\kappa}\cdot\boldsymbol{r}_j(t)} \sum_l E_{o,l}(0)e^{i\boldsymbol{\kappa}\cdot\boldsymbol{r}_l(0)} = \Big[\sum_j E_{o,j}(0)e^{i\boldsymbol{\kappa}\cdot\boldsymbol{r}_j(0)} \sum_l E_{o,l}(0)e^{i\boldsymbol{\kappa}\cdot\boldsymbol{r}_l(0)}\Big]e^{-\frac{\kappa^2 k}{nc_v}} \tag{C.6}$$

Applying ensemble average on both sides and rearranging,

$$\begin{aligned}&\Big\langle \sum_j \sum_l E_{o,j}(t)E_{o,l}(0)e^{i\boldsymbol{\kappa}\cdot(\boldsymbol{r}_j(t)-\boldsymbol{r}_l(0))}\Big\rangle \\ &= \Big\langle \sum_j \sum_l E_{o,j}(0)E_{o,l}(0)e^{i\boldsymbol{\kappa}\cdot(\boldsymbol{r}_j(0)-\boldsymbol{r}_l(0))}\Big\rangle e^{-\frac{\kappa^2 k}{nc_v}}\end{aligned} \tag{C.7}$$

Next, we expand both sides as a Taylor series about $\kappa = 0$ and assuming small perturbations, we keep up to the second order. For simplicity, we will only consider the x direction without losing generality. The left hand side is then

$$\begin{aligned}&\Big\langle \sum_j \sum_l E_{o,j}(t)E_{o,l}(0)\Big\rangle + i\kappa\Big\langle \sum_j \sum_l E_{o,j}(t)E_{o,l}(0)\big[x_j(t) - x_l(0)\big]\Big\rangle \\ &-\frac{\kappa}{2}\Big\langle \sum_j \sum_l E_{o,j}(t)E_{o,l}(0)\big[x_j(t) - x_l(0)\big]^2\Big\rangle\end{aligned} \tag{C.8}$$

We now examine each term. In equilibrium, the expectation value at time t of a dynamic property that depends on the particle positions and velocities is same as that at $t = 0$.

$$\begin{aligned}\Big\langle \sum_j \sum_l E_{o,j}(t)E_{o,l}(0)\Big\rangle &= \Big\langle \sum_j \sum_l (E_j - \langle E_j\rangle)(E_l - \langle E_l\rangle)\Big\rangle \\ &= \Big\langle \sum_j \sum_l (E_jE_l - E_j\langle E_l\rangle - E_l\langle E_j\rangle + \langle E_j\rangle\langle E_l\rangle)\Big\rangle \\ &= \Big\langle E_t^2 - 2E_t\langle E_t\rangle + \langle E_t\rangle^2\Big\rangle \\ &= \Big\langle (E_t - \langle E_t\rangle)^2\Big\rangle \\ &= Nc_vk_BT^2\end{aligned} \tag{C.9}$$

where $E_t = \sum_n E_n$ is the total energy of the system and N is the total number of atoms. In the last step, I have used the fact that for canonical ensemble systems,

$$\Big\langle (E_t - \langle E_t\rangle)^2\Big\rangle = \frac{\partial^2 lnZ}{\partial\beta^2} \tag{C.10}$$

where Z is the partition function and $\beta = k_BT$.

The first order expansion term can be written as

$$i\kappa\Big\langle \sum_j \sum_l E_{o,j}(t)E_{o,l}(0)\big[x_j(t) - x_l(0)\big]\Big\rangle$$

$$
\begin{aligned}
&= i\kappa\left[\left\langle \sum_j \sum_l E_{o,j}(t)E_{o,l}(0)x_j(t)\right\rangle - \left\langle \sum_j \sum_l E_{o,j}(t)E_{o,l}(0)x_j(0)\right\rangle\right] \\
&= i\kappa\left[\left\langle \sum_j \sum_l E_{o,j}(0)E_{o,l}(0)x_j(0)\right\rangle - \left\langle \sum_j \sum_l E_{o,j}(0)E_{o,l}(0)x_j(0)\right\rangle\right] \qquad \text{(C.11)} \\
&= 0
\end{aligned}
$$

The second order term can be written as

$$
\frac{-kappa^2}{2}\left\langle \sum_j \sum_l E_{o,j}(t)E_{o,l}(0)\left[x_j(t) - x_l(0)\right]^2\right\rangle
$$

$$
\begin{aligned}
= \frac{-\kappa^2}{2}\Bigg[&\left\langle \sum_j \sum_l E_{o,j}(t)E_{o,l}(0)x_j(t)^2\right\rangle - 2\left\langle \sum_j \sum_l E_{o,j}(t)E_{o,l}(0)x_j(t)x_l(0)\right\rangle \\
&+\left\langle \sum_j \sum_l E_{o,j}(t)E_{o,l}(0)x_l(0)^2\right\rangle\Bigg]
\end{aligned}
$$

$$
\begin{aligned}
= \frac{-\kappa^2}{2}\Bigg[&\left\langle \sum_j \sum_l E_{o,j}(t)E_{o,l}(t)x_j(t)^2\right\rangle - 2\left\langle \sum_j \sum_l E_{o,j}(t)E_{o,l}(0)x_j(t)x_l(0)\right\rangle \\
&+\left\langle \sum_j \sum_l E_{o,j}(t)E_{o,l}(0)x_l(0)^2\right\rangle\Bigg] \qquad \text{(C.12)}
\end{aligned}
$$

If we assume that the particles are densely populated, we can write

$$
\left\langle \sum_j \sum_l E_{o,j}(t)E_{o,l}(t)x_j(t)^2\right\rangle = \left\langle \sum_j E_{o,j}(t)x_j(t)\sum_l E_{o,l}(t)x_l(t)\right\rangle \qquad \text{(C.13)}
$$

Therefore, the second order correction term becomes

$$
\frac{-\kappa^2}{2}\left\langle \left(\sum_j x_j(t)E_{o,j}(t) - x_j(0)E_{o,j}(0)\right)^2\right\rangle \qquad \text{(C.14)}
$$

The left hand side of the Eq. C.7 is then

$$
Nk_BT^2c_v - \frac{\kappa^2}{2}\left\langle \left(\sum_j x_j(t)E_{o,j}(t) - x_j(0)E_{o,j}(0)\right)^2\right\rangle \qquad \text{(C.15)}
$$

Now, we consider the right hand side of Eq. C.7 and expand up to the second order about $\kappa = 0$. With the same argument as the zeroth term on the left hand side, the zeroth term on the right hand side,

$$
\left\langle \sum_j \sum_l E_{o,j}(0)E_{o,l}\right\rangle = Nk_BT^2c_v \qquad \text{(C.16)}
$$

For $\kappa = 0$, the first order term can be written as

$$i\kappa\Big\langle \sum_j \sum_l E_{o,j}(0)E_{o,l}[x_j(0) - x_l(0)]\Big\rangle \tag{C.17}$$

With the same argument as the first term on the left hand side, the first order term on the right hand side is equal to 0.

If we define

$$\begin{aligned} a &= \Big\langle \sum_j \sum_l E_{o,j}(0)E_{o,l}(0)e^{i\boldsymbol{\kappa}\cdot(\boldsymbol{r}_j(0)-\boldsymbol{r}_l(0))}\Big\rangle \\ b &= e^{\frac{-\kappa^2 k}{nc_v}} \end{aligned} \tag{C.18}$$

For the secord order term, we need to evaluate the derivative

$$\frac{\partial^2(ab)}{\partial\kappa^2} = a\frac{\partial^2 b}{\partial\kappa^2} + 2\frac{\partial a}{\partial\kappa}\frac{\partial b}{\partial\kappa} + \frac{\partial^2 b}{\partial\kappa^2} \tag{C.19}$$

The derivative of the exponential is zero at $\kappa = 0$. Carrying out the algebra (not shown here), the second order term is equal to $-Vk_BT^2k_x\kappa^2$. Therefore, the right hand side of Eq. C.7 is

$$Nk_BT^2c_v - Vk_BT^2k_x\kappa^2 \tag{C.20}$$

Equating the left hand side and the right hand side of Eq. C.7 and solving for kx,

$$k_x = \frac{1}{k_BT^2V}\Big\langle \Big(\sum_j [E_{j,o}(t)x_j(t) - E_{j,o}(0)x_j(0)]\Big)^2\Big\rangle \tag{C.21}$$

In order to obtain the Green-Kubo formula, we transform the summation to the integral form. We use the fact that

$$\Big\langle \Big(\sum_j [E_{j,o}(t)x_j(t) - E_{j,o}(0)x_j(0)]\Big)^2\Big\rangle = \int_0^t \frac{d}{dt}\sum_j E_{j,o}(t')x_j(t')dt' \tag{C.22}$$

and we define $\boldsymbol{S(t)}$ in x-direction as

$$S_x(t) = \frac{d}{dt}\sum_j E_{j,o}(t)x_j(t) \tag{C.23}$$

Here $\boldsymbol{S(t)}$ is often referred to as the heat current or energy current. However, this is misleading as $\boldsymbol{S(t)}$ has the units of Wm. The Green-Kubo formula I have used in previous chapters use actual heat currents with the units of Wm^{-2}. Hence, the volume, V, is located in the numerator instead.

Using the heat current as defined above, the ensemble average can be written as

$$\begin{aligned}\left\langle \Big(\sum_j [E_{j,o}(t)x_j(t) - E_{j,o}(0)x_j(0)] \Big)^2 \right\rangle &= \left\langle \int_0^t S_x(t')dt' \int_0^t S_x(t'')dt'' \right\rangle \\ &= \int_0^t \int_0^t \Big\langle S_x(t')S_x(t'') \Big\rangle dt'dt'' \\ &= \int_0^t \int_0^t \Big\langle S_x(t''-t')S_x(0) \Big\rangle dt'dt'' \\ &= 2t \int_0^t (1-\frac{\tau}{t}) \Big\langle S_x(\tau)S_x(0) \Big\rangle d\tau\end{aligned} \tag{C.24}$$

In the last step, I have the used the identity that

$$\int_0^t \int_0^t f(t''-t')dt'dt'' = 2t \int_0^t (1-\frac{\tau}{t}) f(\tau)d\tau \tag{C.25}$$

Therefore, the thermal conductivity in x-direction can be written as $t \to \infty$,

$$k_x = \frac{1}{Vk_BT^2} \int_0^\infty \Big\langle S_x(t)S_x(0) \Big\rangle dt \tag{C.26}$$

For three dimensional systems, the thermal conductivity tensor can be written as

$$k_{ij} = \frac{1}{Vk_BT^2} \int_0^\infty \Big\langle S_i(t)S_j(0) \Big\rangle dt \tag{C.27}$$

where the indices i, j refer to the cartesian directions and heat current vector is

$$\boldsymbol{S}(t) = \frac{d}{dt} \sum_j E_{j,o}(t)\boldsymbol{r}_j(t) \tag{C.28}$$

Once the heat current vectors are calculated (e.g. using LAMMPS [61]), thermal conductivity can be calculated using the Green-Kubo formalism outlined above.

Appendix D

NORMAL MODE METHODS TO DETERMINE PROPAGON TO DIFFUSON AND DIFFUSON TO LOCON CROSSOVER FREQUENCIES

Crossover frequencies from propagon to diffuson (Ioffe-Regel) and diffuson to locon (mobility edge) crossover frequencies from several works in amorphous silicon are summarized in Table D.1. One way to determine the Ioffe-Regel (IR) frequency was to find the frequency at which propagon diffusivity using the Debye sound velocity and normal mode lifetimes is equal to the Allen-Feldman diffusivity [44]. Using this method, the propagon to diffuson crossover frequency was reported at 1.8 THz. However, utilizing this method may lead to an over-simplification in characterizing the IR frequency as there is no theory to support that longitudinal propagons and transverse propagons must have the same IR frequency. Another way to determine the IR frequency is to use the equilibrium atomic positions and eigenvectors of individual normal modes then look for planewave-like periodicity in the eigenvectors [76]. The eigenvector periodicity (EP) of a mode is further normalized by a fictitious normal mode that has pure sinusoidal modulation, which provides information about the degree of propagation of that particular mode. However, the EP method also has some flaws. It only provides the information of periodicity of a normal mode frozen at 0 K without interacting with any other normal modes; therefore, the degree of the periodicity of a normal mode at finite temperatures is not known. Inverse participation ratio (IPR) which has been used to find the diffuson to locon crossover frequency (mobility edge) is also based on eigenvectors from the lattice dynamics. In brief, it measures the number of atoms participating in an individual mode. In the most ideal case where only one atom is participating in a normal mode, the normal mode is then a locon. On the other hand, if the normal mode is delocalized, there will be many other atoms participating in that mode. Then again, this calculation is done at 0 K and it is unknown how finite temperature will affect the predictions from the IPR.

Work	IR frequency (THz)	Method	Mobility edge (THz)	Method
Ref. [62]	3	-	-	-
Ref. [44]	1.8	$D_{pr} = D_{AF}$	-	$D_{AF} \rightarrow 0$
Ref. [54]	2	-	16.5	IPR
Ref. [76]	2	EP	17	IPR

Table D.1: Propagon to diffuson (IR frequency) and diffuson to locon crossover (mobility edge) frequencies and the corresponding methods to determine them in amorphous silicon by various works [44, 54, 62, 76]. D_{pr} and D_{AF} represent propagon and Allen and Feldman diffusivities, respectively. IPR is the inverse participation ratio and EP is the eigenvector periodicity. "-" denotes items not explicitly mentioned. All works mentioned employed Tersoff potentials [94, 155] except Ref. [44] which used Stillinger-Weber potential [57]. All works employed a 4096-atom structure.

BIBLIOGRAPHY

1. Anderson, P. W. Through the Glass Lightly. en. *Science* **267,** 1615–1616. ISSN: 0036-8075, 1095-9203 (1995).
2. McGaughey, A. & Kaviany, M. en. in *Advances in Heat Transfer* 169–255 (Elsevier, 2006). ISBN: 978-0-12-020039-9.
3. Kittel, C. Interpretation of the Thermal Conductivity of Glasses. *Physical Review* **75,** 972–974 (1949).
4. Cahill, D. G. & Pohl, R. O. Heat flow and lattice vibrations in glasses. *Solid State Communications* **70,** 927–930. ISSN: 0038-1098 (1989).
5. Cahill, D. G., Watson, S. K. & Pohl, R. O. Lower limit to the thermal conductivity of disordered crystals. en. *Physical Review B* **46,** 6131–6140. ISSN: 0163-1829, 1095-3795 (1992).
6. Agne, M. T., Hanus, R. & Snyder, G. J. Minimum thermal conductivity in the context of *diffuson* -mediated thermal transport. en. *Energy & Environmental Science* **11,** 609–616. ISSN: 1754-5692, 1754-5706 (2018).
7. Kittel, C. *Introduction to solid state physics. Fifth edition* (1976).
8. Ibach, H. & Lüth, H. en. in *Solid-State Physics: An Introduction to Principles of Materials Science* (eds Ibach, H. & Lüth, H.) 83–103 (Springer, Berlin, Heidelberg, 1996). ISBN: 978-3-642-88199-2.
9. Zeller, R. C. & Pohl, R. O. Thermal conductivity and specific heat of non-crystalline solids. *Physical Review B* **4,** 2029 (1971).
10. Eucken, A. Über die Temperaturabhängigkeit der Wärmeleitfähigkeit fester Nichtmetalle. en. *Annalen der Physik* **339,** 185–221. ISSN: 1521-3889 (1911).
11. Phillips, W. A. Tunneling states in amorphous solids. en. *Journal of Low Temperature Physics* **7,** 351–360. ISSN: 1573-7357 (1972).
12. Anderson, P. w., Halperin, B. I. & Varma, c. M. Anomalous low-temperature thermal properties of glasses and spin glasses. *The Philosophical Magazine: A Journal of Theoretical Experimental and Applied Physics* **25,** 1–9. ISSN: 0031-8086 (1972).
13. Parshin, D. A., Schober, H. R. & Gurevich, V. L. Vibrational instability, two-level systems, and the boson peak in glasses. en. *Physical Review B* **76.** ISSN: 1098-0121, 1550-235X (2007).
14. Shintani, H. & Tanaka, H. Universal link between the boson peak and transverse phonons in glass. *Nature Materials* **7,** 870–877. ISSN: 1476-1122, 1476-4660 (2008).

15. Schirmacher, W. Thermal conductivity of glassy materials and the “boson peak". *Europhysics Letters (EPL)* **73,** 892–898. ISSN: 0295-5075, 1286-4854 (2006).

16. Flores-Ruiz, H. M. & Naumis, G. G. The transverse nature of the Boson peak: A rigidity theory approach. en. *Physica B: Condensed Matter* **418,** 26–31. ISSN: 09214526 (2013).

17. Lubchenko, V. & Wolynes, P. G. The origin of the boson peak and thermal conductivity plateau in low-temperature glasses. *Proceedings of the National Academy of Sciences* **100,** 1515–1518 (2003).

18. Chumakov, A. I. *et al.* Role of Disorder in the Thermodynamics and Atomic Dynamics of Glasses. en. *Physical Review Letters* **112.** ISSN: 0031-9007, 1079-7114 (2014).

19. Einstein, A. Elementare Betrachtungen über die thermische Molekularbewegung in festen Körpern. en. *Annalen der Physik* **340,** 679–694. ISSN: 1521-3889 (1911).

20. Born, M. & von Kármán, T. Vibrations in space gratings (molecular frequencies). *Z. Phys* **13,** 297–309 (1912).

21. Debye, P. Zur theorie der spezifischen Wärmen. *Annalen der Physik* **344,** 789–839 (1912).

22. Pohl, R. Lattice vibrations of glasses. en. *Journal of Non-Crystalline Solids* **352,** 3363–3367. ISSN: 00223093 (2006).

23. Mukhopadhyay, S. *et al.* Two-channel model for ultralow thermal conductivity of crystalline Tl3VSe4. en. *Science* **360,** 1455–1458. ISSN: 0036-8075, 1095-9203 (2018).

24. Cahill, D. G. & Pohl, R. O. Lattice Vibrations and Heat Transport in Crystals and Glasses. *Annual Review of Physical Chemistry* **39,** 93–121 (1988).

25. Cahill, D. G. & Pohl, R. O. Thermal conductivity of amorphous solids above the plateau. *Physical review B* **35,** 4067 (1987).

26. Phillips, W. A. Two-level states in glasses. en. *Reports on Progress in Physics* **50,** 1657–1708. ISSN: 0034-4885, 1361-6633 (1987).

27. Jäckle, J. On the ultrasonic attenuation in glasses at low temperatures. en. *Zeitschrift für Physik A Hadrons and nuclei* **257,** 212–223. ISSN: 0939-7922 (1972).

28. Jones, D. P. & Phillips, W. A. Thermal conductivity of vitreous silica. en. *Physical Review B* **27,** 3891–3894. ISSN: 0163-1829 (1983).

29. Golding, B., Graebner, J. E., Halperin, B. I. & Schutz, R. J. Nonlinear Phonon Propagation in Fused Silica below 1 K. en. *Physical Review Letters* **30,** 223–226. ISSN: 0031-9007 (1973).

30. Leggett, A. J. & Vural, D. C. "Tunneling Two-Level Systems" Model of the Low-Temperature Properties of Glasses: Are "Smoking-Gun" Tests Possible? *The Journal of Physical Chemistry B* **117,** 12966–12971. ISSN: 1520-6106 (2013).

31. Liu, X., Queen, D. R., Metcalf, T. H., Karel, J. E. & Hellman, F. Hydrogen-Free Amorphous Silicon with No Tunneling States. *Physical Review Letters* **113,** 025503 (2014).

32. Perez-Castaneda, T., Rodriguez-Tinoco, C., Rodriguez-Viejo, J. & Ramos, M. A. Suppression of tunneling two-level systems in ultrastable glasses of indomethacin. en. *Proceedings of the National Academy of Sciences* **111,** 11275–11280. ISSN: 0027-8424, 1091-6490 (2014).

33. Moon, J. & Minnich, A. J. Sub-amorphous thermal conductivity in amorphous heterogeneous nanocomposites. en. *RSC Advances* **6,** 105154–105160 (2016).

34. Poudel, B. *et al.* High-Thermoelectric Performance of Nanostructured Bismuth Antimony Telluride Bulk Alloys. en. *Science* **320,** 634–638. ISSN: 0036-8075, 1095-9203 (2008).

35. Biswas, K. *et al.* High-performance bulk thermoelectrics with all-scale hierarchical architectures. *Nature* **489,** 414–418. ISSN: 0028-0836, 1476-4687 (2012).

36. Zebarjadi, M., Esfarjani, K., Dresselhaus, M. S., Ren, Z. F. & Chen, G. Perspectives on thermoelectrics: from fundamentals to device applications. en. *Energy Environ. Sci.* **5,** 5147–5162. ISSN: 1754-5692, 1754-5706 (2012).

37. Cahill, D. G. *et al.* Nanoscale thermal transport. II. 2003–2012. en. *Applied Physics Reviews* **1,** 011305. ISSN: 1931-9401 (2014).

38. Zhao, L.-D., Dravid, V. P. & Kanatzidis, M. G. The panoscopic approach to high performance thermoelectrics. en. *Energy Environ. Sci.* **7,** 251–268. ISSN: 1754-5692, 1754-5706 (2014).

39. Minnich, A. J. Advances in the measurement and computation of thermal phonon transport properties. *Journal of Physics: Condensed Matter* **27,** 053202. ISSN: 0953-8984, 1361-648X (2015).

40. Foote, M. C. & Jones, E. W. *High-performance micromachined thermopile linear arrays* in *Aerospace/Defense Sensing and Controls* (International Society for Optics and Photonics, 1998), 192–197.

41. Mizuno, H., Mossa, S. & Barrat, J.-L. Beating the amorphous limit in thermal conductivity by superlattices design. *Scientific Reports* **5,** 14116. ISSN: 2045-2322 (2015).

42. Allen, P. B. & Feldman, J. L. Thermal conductivity of glasses: Theory and application to amorphous Si. *Physical review letters* **62,** 645 (1989).

43. Allen, P. B., Feldman, J. L., Fabian, J. & Wooten, F. Diffusons, locons and propagons: Character of atomie yibrations in amorphous Si. *Philosophical Magazine B* **79,** 1715–1731 (1999).

44. Larkin, J. M. & McGaughey, A. J. H. Thermal conductivity accumulation in amorphous silica and amorphous silicon. en. *Physical Review B* **89.** ISSN: 1098-0121, 1550-235X (2014).

45. Minnich, A. & Chen, G. Modified effective medium formulation for the thermal conductivity of nanocomposites. en. *Applied Physics Letters* **91,** 073105. ISSN: 00036951 (2007).

46. Chiritescu, C. *et al.* Ultralow Thermal Conductivity in Disordered, Layered WSe2 Crystals. *Science* **315,** 351–353 (2007).

47. Chen, Z. & Dames, C. An anisotropic model for the minimum thermal conductivity. en. *Applied Physics Letters* **107,** 193104. ISSN: 0003-6951, 1077-3118 (2015).

48. Wingert, M. C. *et al.* Sub-amorphous Thermal Conductivity in Ultrathin Crystalline Silicon Nanotubes. en. *Nano Letters* **15,** 2605–2611. ISSN: 1530-6984, 1530-6992 (2015).

49. Dechaumphai, E. *et al.* Ultralow Thermal Conductivity of Multilayers with Highly Dissimilar Debye Temperatures. en. *Nano Letters* **14,** 2448–2455. ISSN: 1530-6984, 1530-6992 (2014).

50. Norouzzadeh, P., Nozariasbmarz, A., Krasinski, J. S. & Vashaee, D. Thermal conductivity of nanostructured SixGe1-x in amorphous limit by molecular dynamics simulation. en. *Journal of Applied Physics* **117,** 214303. ISSN: 0021-8979, 1089-7550 (2015).

51. Giri, A., Hopkins, P. E., Wessel, J. G. & Duda, J. C. Kapitza resistance and the thermal conductivity of amorphous superlattices. en. *Journal of Applied Physics* **118,** 165303. ISSN: 0021-8979, 1089-7550 (2015).

52. Dove, M. T. *Introduction to lattice dynamics* ISBN: 0-521-39293-4 (Cambridge university press, 1993).

53. Ladd, A. J. C., Moran, B. & Hoover, W. G. Lattice thermal conductivity: A comparison of molecular dynamics and anharmonic lattice dynamics. en. *Physical Review B* **34,** 5058–5064. ISSN: 0163-1829 (1986).

54. Lv, W. & Henry, A. Direct calculation of modal contributions to thermal conductivity via Green–Kubo modal analysis. *New Journal of Physics* **18,** 013028. ISSN: 1367-2630 (2016).

55. Hardy, R. J. Energy-Flux Operator for a Lattice. en. *Physical Review* **132,** 168–177. ISSN: 0031-899X (1963).

56. Allen, P. B. & Feldman, J. L. Thermal conductivity of disordered harmonic solids. *Physical Review B* **48,** 12581 (1993).

57. Stillinger, F. H. & Weber, T. A. Computer simulation of local order in condensed phases of silicon. *Physical review B* **31,** 5262 (1985).

58. Barkema, G. T. & Mousseau, N. High-quality continuous random networks. *Physical Review B* **62,** 4985 (2000).

59. Ding, K. & Andersen, H. C. Molecular-dynamics simulation of amorphous germanium. *Physical Review B* **34,** 6987 (1986).

60. Laradji, M., Landau, D. P. & Dünweg, B. Structural properties of Si 1- x Ge x alloys: A Monte Carlo simulation with the Stillinger-Weber potential. *Physical Review B* **51,** 4894 (1995).

61. Plimpton, S. Fast parallel algorithms for short-range molecular dynamics. *Journal of computational physics* **117,** 1–19 (1995).

62. He, Y., Donadio, D. & Galli, G. Heat transport in amorphous silicon: Interplay between morphology and disorder. en. *Applied Physics Letters* **98,** 144101. ISSN: 00036951 (2011).

63. Dickey, J. M. & Paskin, A. Computer simulation of the lattice dynamics of solids. *Physical Review* **188,** 1407 (1969).

64. Bell, R. J. & Dean, P. Atomic vibrations in vitreous silica. *Discussions of the Faraday society* **50,** 55–61 (1970).

65. Gale, J. D. GULP: A computer program for the symmetry-adapted simulation of solids. *Journal of the Chemical Society, Faraday Transactions* **93,** 629–637 (1997).

66. Yang, L., Yang, N. & Li, B. Extreme Low Thermal Conductivity in Nanoscale 3D Si Phononic Crystal with Spherical Pores. en. *Nano Letters* **14,** 1734–1738. ISSN: 1530-6984, 1530-6992 (2014).

67. Chen, J., Zhang, G. & Li, B. Remarkable Reduction of Thermal Conductivity in Silicon Nanotubes. en. *Nano Letters* **10,** 3978–3983. ISSN: 1530-6984, 1530-6992 (2010).

68. Feldman, J. & Bernstein, N. Vibrational spectroscopy of an amorphous/ crystalline sandwich structure for silicon: Numerical results. en. *Physical Review B* **70,** 235214. ISSN: 1098-0121, 1550-235X (2004).

69. Moon, J. & Minnich, A. J. Examining the validity of normal modes as fundamental heat carriers in amorphous materials. *In preparation.*

70. Lv, W., Winters, R. M., DeAngelis, F., Weinberg, G. & Henry, A. Understanding Divergent Thermal Conductivity in Single Polythiophene Chains Using Green–Kubo Modal Analysis and Sonification. *The Journal of Physical Chemistry A* **121,** 5586–5596. ISSN: 1089-5639 (2017).

71. Zhou, Y., Morshedifard, A., Lee, J. & Abdolhosseini Qomi, M. J. The contribution of propagons and diffusons in heat transport through calcium-silicate-hydrates. en. *Applied Physics Letters* **110,** 043104. ISSN: 0003-6951, 1077-3118 (2017).

72. Feldman, J. L., Kluge, M. D., Allen, P. B. & Wooten, F. Thermal conductivity and localization in glasses: Numerical study of a model of amorphous silicon. *Physical Review B* **48,** 12589 (1993).

73. Bickham, S. R. & Feldman, J. L. Calculation of vibrational lifetimes in amorphous silicon using molecular dynamics simulations. *Physical Review B* **57,** 12234 (1998).

74. Fabian, J. & Allen, P. B. Anharmonic decay of vibrational states in amorphous silicon. *Physical review letters* **77,** 3839 (1996).

75. Fabian, J., Feldman, J. L., Hellberg, C. S. & Nakhmanson, S. M. Numerical study of anharmonic vibrational decay in amorphous and paracrystalline silicon. en. *Physical Review B* **67.** ISSN: 0163-1829, 1095-3795 (2003).

76. Seyf, H. R. & Henry, A. A method for distinguishing between propagons, diffusions, and locons. en. *Journal of Applied Physics* **120,** 025101. ISSN: 0021-8979, 1089-7550 (2016).

77. DeAngelis, F. *et al.* Thermal Transport in Disordered Materials. en. *Nanoscale and Microscale Thermophysical Engineering* (2018).

78. Feldman, J. L. & Kluge, M. D. Realistic model calculations based on the Kubo theory for the thermal conductivity of amorphous insulators. en. *Philosophical Magazine B* **71,** 641–647. ISSN: 1364-2812, 1463-6417 (1995).

79. Lv, W. & Henry, A. Non-negligible Contributions to Thermal Conductivity From Localized Modes in Amorphous Silicon Dioxide. en. *Scientific Reports* **6,** 35720. ISSN: 2045-2322 (2016).

80. Lv, W. & Henry, A. Phonon transport in amorphous carbon using Green – Kubo modal analysis. en. *Applied Physics Letters* **108,** 181905. ISSN: 0003-6951, 1077-3118 (2016).

81. Zhu, T. & Ertekin, E. Phonons, Localization, and Thermal Conductivity of Diamond Nanothreads and Amorphous Graphene. en. *Nano Letters* **16,** 4763–4772. ISSN: 1530-6984, 1530-6992 (2016).

82. Carlson, D. E. & Wronski, C. R. Amorphous silicon solar cell. *Applied Physics Letters* **28,** 671–673. ISSN: 0003-6951 (1976).

83. Bullock, J. *et al.* Efficient silicon solar cells with dopant-free asymmetric heterocontacts. en. *Nature Energy* **1,** 15031. ISSN: 2058-7546 (2016).

84. Birney, R. *et al.* Amorphous Silicon with Extremely Low Absorption: Beating Thermal Noise in Gravitational Astronomy. *Physical Review Letters* **121,** 191101 (2018).

85. Cahill, D. G., Katiyar, M. & Abelson, J. R. Thermal conductivity of a-Si: H thin films. *Physical review B* **50,** 6077 (1994).

86. Liu, X. *et al.* High Thermal Conductivity of a Hydrogenated Amorphous Silicon Film. en. *Physical Review Letters* **102.** ISSN: 0031-9007, 1079-7114 (2009).

87. Regner, K. T. *et al.* Broadband phonon mean free path contributions to thermal conductivity measured using frequency domain thermoreflectance. *Nature Communications* **4,** 1640. ISSN: 2041-1723 (2013).

88. Braun, J. L. *et al.* Size effects on the thermal conductivity of amorphous silicon thin films. en. *Physical Review B* **93.** ISSN: 2469-9950, 2469-9969 (2016).

89. Kwon, S., Zheng, J., Wingert, M. C., Cui, S. & Chen, R. Unusually High and Anisotropic Thermal Conductivity in Amorphous Silicon Nanostructures. en. *ACS Nano.* ISSN: 1936-0851, 1936-086X (2017).

90. Zink, B. L., Pietri, R. & Hellman, F. Thermal Conductivity and Specific Heat of Thin-Film Amorphous Silicon. en. *Physical Review Letters* **96.** ISSN: 0031-9007, 1079-7114 (2006).

91. Lv, W. & Henry, A. Examining the Validity of the Phonon Gas Model in Amorphous Materials. en. *Scientific Reports* **6.** ISSN: 2045-2322 (2016).

92. Callaway, J. Model for lattice thermal conductivity at low temperatures. *Physical Review* **113,** 1046 (1959).

93. Kim, T. *., Moon, J. *. & Minnich, A. J. Role of acoustic excitations in amorphous silicon characterizaed by ultrafast transient grating spectroscopy and picosecond acoustics. *In preparation.*

94. Tersoff, J. Empirical interatomic potential for silicon with improved elastic properties. *Physical Review B* **38,** 9902 (1988).

95. Blöchl, P. E. *et al.* First-principles calculations of self-diffusion constants in silicon. en. *Physical Review Letters* **70,** 2435–2438. ISSN: 0031-9007 (1993).

96. Perdew, J. P., Burke, K. & Ernzerhof, M. Generalized gradient approximation made simple. *Physical review letters* **77,** 3865 (1996).

97. Kresse, G. & Furthmüller, J. Efficient iterative schemes for ab initio total-energy calculations using a plane-wave basis set. *Physical review B* **54,** 11169 (1996).

98. Moon, J. *et al.* Thermal acoustic excitations with atomic-scale wavelengths in amorphous silicon. *Physical Review Materials* **3,** 065601 (2019).

99. Strauß, F. *et al.* Self-Diffusion in Amorphous Silicon. *Physical Review Letters* **116,** 025901 (2016).

100. Strauß, F., Jerliu, B., Geue, T., Stahn, J. & Schmidt, H. Short range atomic migration in amorphous silicon. en. *Journal of Applied Physics* **119,** 175102. ISSN: 0021-8979, 1089-7550 (2016).

101. Simoncelli, M., Marzari, N. & Mauri, F. Unified theory of thermal transport in crystals and glasses. En. *Nature Physics,* 1. ISSN: 1745-2481 (2019).

102. Tian, Z. *et al.* Inelastic x-ray scattering measurements of phonon dispersion and lifetimes in PbTe $_{1-x}$ Se $_{x}$ alloys. *Journal of Physics: Condensed Matter* **27,** 375403. ISSN: 0953-8984, 1361-648X (2015).

103. Lory, P.-F. *et al.* Direct measurement of individual phonon lifetimes in the clathrate compound Ba7.81Ge40.67Au5.33. en. *Nature Communications* **8.** ISSN: 2041-1723 (2017).

104. Schober, H. *et al.* Crystal-like High Frequency Phonons in the Amorphous Phases of Solid Water. en. *Physical Review Letters* **85,** 4100–4103. ISSN: 0031-9007, 1079-7114 (2000).

105. Masciovecchio, C. *et al.* Evidence for a Crossover in the Frequency Dependence of the Acoustic Attenuation in Vitreous Silica. en. *Physical Review Letters* **97.** ISSN: 0031-9007, 1079-7114 (2006).

106. Benassi, P. *et al.* Evidence of high frequency propagating modes in vitreous silica. *Physical review letters* **77,** 3835 (1996).

107. Monaco, G. & Mossa, S. Anomalous properties of the acoustic excitations in glasses on the mesoscopic length scale. *Proceedings of the National Academy of Sciences* **106,** 16907–16912 (2009).

108. Monaco, G. & Giordano, V. M. Breakdown of the Debye approximation for the acoustic modes with nanometric wavelengths in glasses. *Proceedings of the national Academy of Sciences* **106,** 3659–3663 (2009).

109. Sette, F., Krisch, M. H., Masciovecchio, C., Ruocco, G. & Monaco, G. Dynamics of glasses and glass-forming liquids studied by inelastic X-ray scattering. *Science* **280,** 1550–1555 (1998).

110. Sette, F. *et al.* Collective Dynamics in Water by High Energy Resolution Inelastic X-Ray Scattering. en. *Physical Review Letters* **75,** 850–853. ISSN: 0031-9007, 1079-7114 (1995).

111. Alatas, A. *et al.* Elastic modulus of supercooled liquid and hot solid silicon measured by inelastic X-ray scattering. *Journal of Physics and Chemistry of Solids. 5th International Conference on Inelastic X-ray Scattering (IXS 2004)* **66,** 2230–2234. ISSN: 0022-3697 (2005).

112. Baron, A. Q. R. en. in *Synchrotron Light Sources and Free-Electron Lasers* 1–68 (Springer, Cham, 2015). ISBN: 978-3-319-04507-8.

113. Burkel, E. *Inelastic Scattering of X-Rays with Very High Energy Resolution* en. Google-Books-ID: 7pl0DgAAQBAJ. ISBN: 978-3-540-38351-2 (Springer, 2006).

114. Burkel, E. Phonon spectroscopy by inelastic x-ray scattering. en. *Reports on Progress in Physics* **63,** 171. ISSN: 0034-4885 (2000).

115. Cunsolo, A. The terahertz dynamics of simplest fluids probed by inelastic X-ray scattering. en. *International Reviews in Physical Chemistry* **36,** 433–539. ISSN: 0144-235X, 1366-591X (2017).

116. Sinha, S. K. Theory of inelastic x-ray scattering from condensed matter. en. *Journal of Physics: Condensed Matter* **13,** 7511–7523. ISSN: 0953-8984, 1361-648X (2001).

117. Krisch, M. & Sette, F. in *Light Scattering in Solid IX* 317–370 (Springer, 2006).

118. Sinn, H. Spectroscopy with meV energy resolution. en. *Journal of Physics: Condensed Matter* **13,** 7525. ISSN: 0953-8984 (2001).

119. Sinn, H. *et al.* An inelastic X-ray spectrometer with 2.2meV energy resolution. *Nuclear Instruments and Methods in Physics Research Section A: Accelerators, Spectrometers, Detectors and Associated Equipment. Proceedings of the 7th Int. Conf. on Synchrotron Radiation Instru mentation* **467-468,** 1545–1548. ISSN: 0168-9002 (2001).

120. Boon, J. P. & Yip, S. *Molecular Hydrodynamics* en. Google-Books-ID: LfCDDwAAQBAJ. ISBN: 978-0-486-66949-6 (Courier Corporation, 1991).

121. Maradudin, A. A. & Fein, A. E. Scattering of neutrons by an anharmonic crystal. *Physical Review* **128,** 2589 (1962).

122. Mattuck, R. D. *A guide to Feynman diagrams in the many-body problem* ISBN: 0-486-67047-3 (Courier Corporation, 1992).

123. Jishi, R. A. *Feynman diagram techniques in condensed matter physics* ISBN: 1-107-35512-5 (Cambridge University Press, 2013).

124. Masciovecchio, C. *et al.* High-frequency propagating modes in vitreous silica at 295 K. en. *Physical Review B* **55,** 8049–8051. ISSN: 0163-1829, 1095-3795 (1997).

125. Fioretto, D. *et al.* High-frequency dynamics of glass-forming polybutadiene. *Physical Review E* **59,** 4470 (1999).

126. Scopigno, T. *et al.* High frequency acoustic modes in vitreous beryllium fluoride probed by inelastic x-ray scattering. en. *The Journal of Chemical Physics* **118,** 311–316. ISSN: 0021-9606, 1089-7690 (2003).

127. Scopigno, T., Suck, J.-B., Angelini, R., Albergamo, F. & Ruocco, G. High-Frequency Dynamics in Metallic Glasses. en. *Physical Review Letters* **96.** ISSN: 0031-9007, 1079-7114 (2006).

128. Pogna, E. A. A., Rodríguez-Tinoco, C., Krisch, M., Rodríguez-Viejo, J. & Scopigno, T. Acoustic-like dynamics of amorphous drugs in the THz regime. *Scientific reports* **3** (2013).

129. Ruocco, G. & Sette, F. High-frequency vibrational dynamics in glasses. *Journal of Physics: Condensed Matter* **13,** 9141 (2001).

130. Baldi, G., Giordano, V. M., Monaco, G. & Ruta, B. Sound Attenuation at Terahertz Frequencies and the Boson Peak of Vitreous Silica. en. *Physical Review Letters* **104.** ISSN: 0031-9007, 1079-7114 (2010).

131. Rayleigh, J. W. S. B. *The Theory of Sound* en (Macmillan, 1896).

132. Elliott, R. A Unified Model for the Low-Energy Vibrational Behaviour of Amorphous Solids. en. *EUROPHYSICS LETTERS,* 7.

133. Buchenau, U. *et al.* Interaction of soft modes and sound waves in glasses. en. *Physical Review B* **46,** 2798–2808. ISSN: 0163-1829, 1095-3795 (1992).

134. Rufflé, B., Parshin, D. A., Courtens, E. & Vacher, R. Boson Peak and its Relation to Acoustic Attenuation in Glasses. *Physical Review Letters* **100,** 015501 (2008).

135. Rufflé, B., Foret, M., Courtens, E., Vacher, R. & Monaco, G. Observation of the Onset of Strong Scattering on High Frequency Acoustic Phonons in Densified Silica Glass. en. *Physical Review Letters* **90.** ISSN: 0031-9007, 1079-7114 (2003).

136. Baldi, G. *et al.* Emergence of Crystal-like Atomic Dynamics in Glasses at the Nanometer Scale. *Physical Review Letters* **110,** 185503 (2013).

137. Ruocco, G. *et al.* Nondynamic origin of the high-frequency acoustic attenuation in glasses. *Physical Review Letters* **83,** 5583 (1999).

138. Busselez, R., Pezeril, T. & Gusev, V. E. Structural heterogeneities at the origin of acoustic and transport anomalies in glycerol glass-former. en. *The Journal of Chemical Physics* **140,** 234505. ISSN: 0021-9606, 1089-7690 (2014).

139. Grubbs, W. T. & MacPhail, R. A. Dynamics in supercooled glycerol by high resolution stimulated Brillouin gain spectroscopy. en. *The Journal of Chemical Physics* **100,** 2561–2570. ISSN: 0021-9606, 1089-7690 (1994).

140. Moon, J., Latour, B. & Minnich, A. J. Propagating elastic vibrations dominate thermal conduction in amorphous silicon. en. *Physical Review B* **97** (2018).

141. Broughton, J. Q. & Li, X. P. Phase diagram of silicon by molecular dynamics. *Physical Review B* **35,** 9120 (1987).

142. Beltukov, Y. M., Fusco, C., Parshin, D. A. & Tanguy, A. Boson peak and Ioffe-Regel criterion in amorphous siliconlike materials: The effect of bond directionality. en. *Physical Review E* **93.** ISSN: 2470-0045, 2470-0053 (2016).

143. Shapiro, S. M., Axe, J. D., Shirane, G. & Riste, T. Critical Neutron Scattering in SrTi O 3 and KMn F 3. *Physical Review B* **6,** 4332 (1972).

144. Taraskin, S. N. & Elliott, S. R. Low-frequency vibrational excitations in vitreous silica: the Ioffe-Regel limit. *Journal of Physics: Condensed Matter* **11,** A219 (1999).

145. Damart, T., Giordano, V. M. & Tanguy, A. Nanocrystalline inclusions as a low-pass filter for thermal transport in a -Si. en. *Physical Review B* **92.** ISSN: 1098-0121, 1550-235X (2015).

146. Nilsson, G. & Nelin, G. Phonon dispersion relations in Ge at 80 K. *Physical Review B* **3,** 364 (1971).

147. Henke, B. L., Gullikson, E. M. & Davis, J. C. X-Ray Interactions: Photoabsorption, Scattering, Transmission, and Reflection at E = 50-30,000 eV, Z = 1-92. en. *Atomic Data and Nuclear Data Tables* **54,** 181–342. ISSN: 0092-640X (1993).

148. Alatas, A. *et al.* Improved focusing capability for inelastic X-ray spectrometer at 3-ID of the APS: A combination of toroidal and Kirkpatrick-Baez (KB) mirrors. en. *Nuclear Instruments and Methods in Physics Research Section A: Accelerators, Spectrometers, Detectors and Associated Equipment* **649,** 166–168. ISSN: 01689002 (2011).

149. Said, A. H., Sinn, H. & Divan, R. New developments in fabrication of high-energy-resolution analyzers for inelastic X-ray spectroscopy. en. *Journal of Synchrotron Radiation* **18,** 492–496. ISSN: 0909-0495 (2011).

150. Toellner, T. S., Alatas, A. & Said, A. H. Six-reflection meV-monochromator for synchrotron radiation. *Journal of Synchrotron Radiation* **18,** 605–611. ISSN: 0909-0495 (2011).

151. De Brito Mota, F., Justo, J. F. & Fazzio, A. Structural properties of amorphous silicon nitride. *Physical Review B* **58,** 8323 (1998).

152. Voyles, P. M. *et al.* Structure and physical properties of paracrystalline atomistic models of amorphous silicon. *Journal of Applied Physics* **90,** 4437–4451. ISSN: 0021-8979 (2001).

153. Treacy, M. M. J. & Borisenko, K. B. The Local Structure of Amorphous Silicon. en. *Science* **335,** 950–953. ISSN: 0036-8075, 1095-9203 (2012).

154. Munetoh, S., Motooka, T., Moriguchi, K. & Shintani, A. Interatomic potential for Si–O systems using Tersoff parameterization. *Computational Materials Science* **39,** 334–339. ISSN: 0927-0256 (2007).

155. Tersoff, J. Modeling solid-state chemistry: Interatomic potentials for multicomponent systems. *Physical Review B* **39,** 5566–5568 (1989).

156. Cros, B., Gat, E. & Saurel, J. Characterization of the elastic properties of amorphous silicon carbide thin films by acoustic microscopy. en. *Journal of Non-Crystalline Solids* **209,** 273–282. ISSN: 00223093 (1997).

157. Foret, M. *et al.* Neutron Brillouin and Umklapp scattering from glassy selenium. *Physical review letters* **81,** 2100 (1998).

158. Scopigno, T. *et al.* High Frequency Dynamics in a Monatomic Glass. en. *Physical Review Letters* **92.** ISSN: 0031-9007, 1079-7114 (2004).

159. Zeng, Z. *et al.* Synthesis of quenchable amorphous diamond. en. *Nature Communications* **8.** ISSN: 2041-1723 (2017).